

SUBCRITICAL CRACK GROWTH IN ZIRCONIUM ALLOYS

by

ARNALDO HOMOBONO PAES DE ANDRADE

B.S. Universidade de Sao Paulo, Brasil

(1971)

M.S. Universidade de Sao Paulo, Brasil

(1977)

Submitted to the Department of
Materials Science and Engineering
in Partial Fulfillment of the
Requirements of the
Degree of

DOCTOR OF PHILOSOPHY

at the

MASSACHUSETTS INSTITUTE OF TECHNOLOGY

September 1982

c Massachusetts Institute of Technology 1982

Signature of Author.....
Department of Materials Science and Engineering
August 6, 1982

Certified by.....
Professor Regis Marc Noel Pelloux
Thesis Supervisor

Accepted by.....
Professor Regis Marc Noel Pelloux
Chairman, Department Committee on Graduate Students

Archives

MASSACHUSETTS INSTITUTE
OF TECHNOLOGY

OCT 15 1982

In memory of my father

SUBCRITICAL CRACK GROWTH IN ZIRCONIUM ALLOYS

by

ARNALDO HOMOBONO PAES DE ANDRADE

Submitted to the Department of
Materials Science and Engineering
on August 6, 1982 in Partial Fulfillment of the
requirements for the Degree of Doctor of Philosophy

ABSTRACT

The subcritical growth of iodine-induced cracks in unirradiated Zircaloy plate is investigated as a function of the stress intensity factor (K). Microstructure, crystallographic texture (f-number), and temperature are the testing variables. 40Pa is the iodine partial pressure.

Two regimes of crack growth behavior are observed: a low-K regime strongly dependent on the stress intensity factor and a high-K regime where this dependence is not so intense. At 310°C, the K-value at transition is about 10KsiVin for materials with f-number above 0.5. Also, the crack growth rate increases as the f-number increases.

The crack growth data in both regimes can be fitted to power law relations like $da/dt = A \cdot K^n$ where A is a rate constant and n is the exponent. Heat treatment has a large effect on the n value. At 310°C for the low-K crack growth regime n is in the range 3 to 6 for cold work stress relieved (CWSR) Zircaloy and is about 13 for the recrystallized Zircaloy.

For a given K-value the crack growth rate is lower for recrystallized Zircaloy than for CWSR Zircaloy for tests at 310°C. An apparent activation energy, Q, for CWSR Zircaloy is determined to be 2.9 kcal/mole.

Failure topography and the fracture mode of crack growth are identified for the temperatures studied. The primary mode of crack propagation is by transgranular cleavage near the basal planes. At low temperature (25°C and 100°C) plastic deformation by fluting is observed.

To study under what conditions the linear elastic fracture mechanics (LEFM) approach is valid for analyzing the crack growth through a thin-wall cladding, tube pressurization experiments are done on Zircaloy cladding specimens containing fatigue precracks. The time-to-failure under constant stress is measured. This time is then compared to time-to-failure calculations using power law relations for the crack growth. The crack geometry (aspect ratio) is an important variable in this type of analysis.

Thesis Supervisor: Professor Regis Marc Noel Pelloux

Title: Professor of Materials Engineering

ACKNOWLEDGEMENTS

The author is grateful to a number of people who assisted and encouraged him throughout this work and during the course of his graduate education at MIT.

To Professor R.M.N. Pelloux, his thesis advisor, for his technical and personal guidance, and patience.

To Dr. D.B. Knorr for technical assistance and helpful suggestions.

To W. Moshier, J. Peltier, P. Bensussan, J. Scutti and others in the Fracture Mechanics and High Temperature Alloy Deformation research group who assisted in the experimental work and with critical and interesting discussions.

To professor K.C. Russel and R.G. Ballinger, members of the thesis committee, for their review of the manuscript.

To L. Sudenfield and E. Shaw for their technical assistance on the S.E.M.

To Alice Sanderson who typed the manuscript.

To Exxon Nuclear Company, Inc. for their partial funding of this research.

To Comissao Nacional de Energia Nuclear (RJ-Brasil) and Instituto de Pesquisas Energeticas e Nucleares (SP-Brasil) for sponsoring the author's studies at MIT.

To Lane and Laerte for their love, permanent encouragement and infinite patience. Beijos.

TABLE OF CONTENTS

	<u>Page</u>
Abstract	3
Acknowledgements	4
List of Figures	8
List of Tables	13
1. Introduction	14
2. Literature Review and Background	18
2.1 Zirconium and Zirconium Alloys	18
2.1.1 Deformation Mechanisms	18
2.1.2 Relationship Between Fabrication and Texture	20
2.2 Morphological and Microstructural Features of Iodine Stress Corrosion Cracking in Zircalloys	22
2.3 Mechanism of Iodine-Induced SCC of Zircaloy Cladding	24
2.4 Chemical Aspects of the I-SCC of Zircaloy	26
2.4.1 Gaseous Iodides	27
2.4.2 Kinetics of Formation of Solid Iodides on Zirconium	28
2.5 The Effect of Tensile Stress on I-SCC of Zr Alloys	29
2.6 Metallurgical Factors Controlling Cracking	30
2.6.1 Influence of the Crystallographic Texture	31
2.7 Fracture Mechanics Approach to I-SCC Growth in Zirconium Alloys	32
3. Plan of Work	48
4. Description of Materials	51
4.1 Plate Material	51
4.2 Tube Material	51

TABLE OF CONTENTS (continued)

	<u>Page</u>
4.3 Microstructure	52
5. Equipment and Test Procedures	61
5.1 Crack Propagation Tests	61
5.1.1 Fracture Mechanics Specimen	61
5.1.2 Environmental Control System	62
5.1.3 DCB-Specimen Preparation	64
5.2 Tube Pressurization Tests	65
5.2.1 Fatigue Pre-Cracking of Tubing	65
5.2.2 Closed-End Tube Pressurization Test Procedures	66
5.2.3 Fractography	67
6. Data Reduction and Errors Estimation	73
6.1 Crack Growth Tests	73
6.1.1 Uncertainty in Crack Length (a)	73
6.1.2 Uncertainty in K	73
6.1.2.1 Uncertainty in Load (P)	73
6.1.3 Uncertainty in Temperature	74
7. Results	75
7.1 Crack Propagation Tests	75
7.1.1 Crack Growth as a Function of Stress Intensity Factor	75
7.1.2 Shape of the da/dt vs. K Curves	75
7.1.3 Fractography	79
7.2 Tube Pressurization Tests	79
7.2.1 Time-to-Failure of Precracked Specimens	79

TABLE OF CONTENTS (continued)

	<u>Page</u>
7.2.2 Fractography	80
8. Discussion	107
8.1 Mechanism of Cracking	107
8.2 Influence of the Crystallographic Texture	109
8.3 Effect of Microstructural Directionality	109
8.4 Influence of Heat Treatment	110
8.5 Effect of Temperature	111
8.5.1 Apparent Activation Energy Q	112
8.6 Mechanics of Fluting	113
8.7 I-SCC Growth in Zircaloy Cladding	113
8.7.1 Evaluation of the Stress Intensity Factor of the Semi-Elliptical Crack	114
8.7.2 Finite Thickness Correction	115
8.7.3 Time-to-Failure Calculations	116
9. Summary and Conclusions	125
10. Suggestions for Future Work	127
Appendix A: The Kearns' f-Parameter	128
Appendix B: Basic Concepts in Linear Elastic Fracture Mechanics	131
Appendix C: Fatigue Crack Growth Rate Measurements	134
Appendix D: Stress Analysis of Fatigue Precracking of Tubes	140
Appendix E: "TAIL" Computer Program	143
Appendix F: Polynomial Fitting to the Crack Length vs. Time Data	146
References	148
Biographical Note	155

LIST OF FIGURES

<u>Figure No.</u>		<u>Page</u>
1.1	Schematic of PCI Zircaloy fuel rod mechanism	17
2.1	Slip systems in α -Zirconium	37
2.2	Typical fabrication textures in Zircaloy products	38
2.3	Twinning systems in α -Zirconium	39
2.4	(a) Schematic of "fluting" (b) Tearing between overlapping cleavage regions illustrating flute mechanism	40
2.5	The four stages of iodine-induced cladding failure	41
2.6	Pressures of ZrI_4 in gas in equilibrium with solid zirconium iodide phases. The shaded area indicates the probable location of chemisorption curves for iodine on zirconium	42
2.7	Compositions of Zr/I phase stability	43
2.8	Hoop stress vs. time-to-failure for Zirclay-4 exposed to iodine at 360°C	44
2.9	Effect of irradiation on time to failure vs hoop stress for Zircaloy at ~320°C	45
2.10	Relation between basal pole orientation and crack density	46
2.11	Effect of crystallographic texture on K_{ISCC} in Zircaloy	47
3.1	Orientations of fracture mechanics DCB specimens	50
4.1	Basal pole figure for Zircaloy-4 plate 9912-SR at mid-thickness	58
4.2	Basal pole figure for Zircaloy-2 plate 9908-3A at mid-thickness	58
4.3	Basal pole figure for stress relieved Zircaloy-2 tube from supplier A at midwall	59
4.4	Basal pole figure for stress relieved Zircaloy-2 tube from supplier B at midwall	59

LIST OF FIGURES (continued)

<u>Figure No.</u>		<u>Page</u>
4.5	Microstructure of the Zircaloy-4 plate 9912-SR	60
4.6	Microstructure of the Zircaloy-4 plate 9912-RX	60
5.1	Schematic of fracture mechanics DCB specimens	69
5.2	Schematic of the crack growth rate test. Effect of crack growth on load and stress intensity factor	69
5.3	Diagram of the flowing gas (Ar + I ₂) controlled atmosphere system	70
5.4	I-SCC growth test chamber	70
5.5	Device used for fatigue precracking of tubes	71
5.6	Optical macrograph of a fatigue precracked tube	71
5.7	Schematic drawing of the tube pressurization facility	72
7.1	Profiles of I-SCC fracture of 9912-SR Zircaloy plate, NT orientation (a) 310°C, (b) 25°C, (c) 100°C	82
7.2	Optical micrographs of the crack-tip region in cold- worked stress relieved, and in recrystallized Zircaloy at 310°C	83
7.3	Fracture surface of the 9912-SR Zircaloy specimen tested at 310°C. NT and NL orientation. Stereo pair	84
7.4	Fracture surface of (a) 9912-SR Zircaloy plate, TL orientation. Stereo pair. (b) 9908-3A Zircaloy plate. NT orientation. Both tested at 310°C	85
7.5	da/dt vs K regimes schematic	86
7.6	da/dt vs K behavior for specimens tested at 310°C	87
7.7	da/dt vs K curves for 9912 material in the NL orientation in two heat treated conditions: cold-worked stress relieved, and recrystallized	88

LIST OF FIGURES (continued)

<u>Figure No.</u>		<u>Page</u>
7.8	Effect of temperature on the da/dt vs K behavior for 9912-SR Zircaloy plate, NT orientation	89
7.9	Arrhenius analysis of regime II-SCC growth behavior for 9912-SR Zircaloy, NT orientation	90
7.10	Scanning electron micrograph of the fracture surface of 9912-SR specimen. NT orientation tested under 4 Pa of iodine. (a) Transgranular cleavage in the CC region; (b) Dimples in the mechanical overload region	91
7.11	Scanning electron micrographs of the 9912-SR material, NT orientation tested under 40 Pa of iodine at 310°C. (a) Transition from the fatigue region to the SCC region (b) Detail showing fluting features (c) Detail of SCC region (d) Transition from SCC to ductile overload. The crack growth is from bottom to top	92
7.12	Scanning electron micrographs of the 9912-SR material, NT orientation tested under 40 Pa of iodine at 310°C (a) Detail of the precrack region showing fatigue striations (b) Transition from fatigue to SCC (c) Detail showing fluting (d) SCC region at low K value. Crack growth is from bottom to top	93
7.13	Scanning electron micrographs of the 9908-3A material, NL orientation tested under 40 Pa of iodine at 310°C (a) SCC region near the mechanical overload region at the top left (b) Flutes (c) SCC region showing embryonic ductile features ("stitching") (d) Detail of transgranular cleavage	94
7.14	Scanning electron micrographs of the 9912-SR material, TL orientation tested under 40 Pa of iodine at 310°C (a) Corroded fracture surface, (b) Clean fracture surface showing transgranular cleavage	95
7.15	Fracture surface of the recrystallized Zircaloy plate, NL orientation tested at 310°C under 40 Pa of iodine. (a) Transgranular cleavage at high K (b) Transgranular cleavage at low K (~ 10 MPa m) (c) Enlargement of inset area in (b) showing river patterns	96

LIST OF FIGURES (continued)

<u>Figure No.</u>		<u>Page</u>
7.16	Fracture surface of the recrystallized Zircaloy material, NL orientation tested under 40 Pa of iodine at 310°C. K approximately 10 MPa m (a) Transgranular cleavage, (b) Intercrystalline fracture	97
7.17	Scanning electron micrographs of the fracture surface of the recrystallized Zircaloy plate, NL orientation tested at 310°C under 40 Pa of iodine. (a) Fatigue striations in the precrack region (b) Transgranular cleavage in the SCC zone (c) Dimples in the mechanical overload region	98
7.18	(a) Optical micrograph of the stress corrosion crack near the notch in the 9912-SR plate NT orientation, tested under 40 Pa of iodine at room temperature, (b) Scanning electron micrograph of the SCC region	99
7.19	Fracture surface of the 9912-SR Zircaloy material, NT orientation tested under 40 Pa of iodine at room temperature showing fluting plus transgranular cleavage at three magnifications.	100
7.20	Scanning electron micrographs of the fracture surface of the 9912-SR Zircaloy plate, NT orientation tested under 40 Pa of iodine at 100°C. (a) Stereo pair showing fluting plus transgranular cleavage, (b) SCC region at low K, (c) Fluting plus dimples in the fast fracture region.	101
7.21	Schematic of semi-elliptical crack	102
7.22	General view of the fracture surface of the tubing material. (a) Supplier A, SEM micrograph (b) Supplier B, SEM micrograph (c) Supplier B, optical micrograph	103
7.23	Scanning electron micrographs of the Supplier B tubing material (specimen B2) tested at 320°C with 0.2 mg/cm ² of iodine under a stress of 37.5 ksi. (a) Detail of the fatigue precrack zone, (b) Transition from fatigue region to SCC region, (c) Transgranular cleavage in the SCC region	104

LIST OF FIGURES (continued)

<u>Figure No.</u>		<u>Page</u>
7.24	Scanning electron micrographs of the fracture surface of the Supplier B tubing material (specimen B4) tested at 320°C with 0.2 mg/cm ² of iodine under a stress of 37.6 ksi. (a) General view, (b) Detail of the precrack zone of (a) (c) A higher magnification of the fatigue region (d) SCC zone	105
7.25	Scanning electron micrographs of the fracture surface of the Supplier A tubing material (specimen A2) tested at 320°C with 0.2 mg/cm ² of iodine under a stress of 42.0 ksi showing transition zone between fatigue and SCC (a) Deepest point of fatigue precrack (b) surface intersection point	106
8.1	Adsorption of iodine on zirconium	119
8.2	Mechanics of fluting	120
8.3	Log-log plot of I-SCC growth rate for Zircaloy plate 9912-SR	121
8.4	Time-to-failure vs hoop stress Zircaloy plate 9912-SR, $a_0/t = .3$	122
8.5	Time-to-failure vs hoop stress Zircaloy plate 9912-SR, $a_0/t = .5$	123
8.6	Log-log plot of I-SCC growth rate for Zircaloy plate 9912-RX	124
B.1	Basis of linear elastic fracture mechanics	133
C.1	Basal pole figure	137
C.2	Fatigue crack propagation behavior of CWSR Zircaloy-2 plate cycled in air at 25°C	138
C.3	Scanning electron micrographs of fracture surface of Zircaloy-2 plate fatigue in air at 25°C (a) Region near the crack starter (b) Detail at $K \approx 12 \text{ Ksi}\sqrt{\text{in}}$ (c) Detail at $K \approx 30 \text{ Ksi}\sqrt{\text{in}}$ (d) Fatigue striations. Crack path from bottom to top	139
E.1	Listing of "TAIL" Computer Program	144
F.1	Growth of iodine-induced crack in Zircaloy	147

LIST OF TABLES

<u>Table No.</u>		<u>Page</u>
2.1	Designation and composition of some important zirconium alloys	34
2.2	Deformation systems in Zircalloys	35
2.3	Thermochemical data for gaseous iodides	36
4.1	Chemical composition of Zircaloy plates	55
4.2	Fabrication schedules for Zircaloy plates	56
4.3	Kearns' f-number for Zircaloy plates	57
4.4	Chemical analysis of tubing from suppliers A and B	57
7.1	Results of the tube pressurization experiments	81

1. INTRODUCTION

Environment-induced crack growth usually occurs below gross yielding and thus it is appropriate to use a linear elastic fracture mechanics (LEFM) analysis to correlate the SCC crack growth rates to loads and geometry.

The basic tenet of LEFM is that unstable mechanical crack propagation will occur when the stress intensity factor near the tip of a sharp flaw equals or exceeds a critical value K_{IC} , the fracture toughness index. Since by definition, SCC occurs at stress intensity factors lower than critical, the term SCC (stress corrosion cracking) as used in this thesis denotes "environment-induced subcritical crack growth under sustained stress."

Experience with water-cooled reactor fuel rods, in which uranium dioxide fuel pellets are clad with Zircaloy tubing, has shown that a sufficiently severe power increase (ramp) can cause cladding failure, provided the burn-up is high enough. Any power increase produces an increased radial temperature gradient within the fuel pellets, and results in expansion of the pellets. The Zircaloy cladding is stressed as a result of the fuel thermal expansion, hence the term pellet-clad interaction (PCI) (Figure 1.1)

If the power increases, and the resulting expansion of the fuel pellets is slow enough, then the cladding and possibly the fuel can yield by plastic flow and creep and the stresses in the cladding will remain low. On the other hand, if the power increase is rapid (high ramp rate) then the cladding hoop stresses are high because plastic

flow is less effective as a stress-reducing mechanism. This hoop stress is responsible for the formation and propagation of cracks in the cladding, and fractures have occurred at times that range between a few minutes to many hours after the attainment of maximum power.

The cladding fracture characteristics resulting from power ramp excursions have been discussed (1), and it is generally accepted that most of the failures occur by a stress corrosion (SCC) mechanism with fission product iodine being regarded as the most likely active chemical species.

PCI failure rates are currently maintained at an acceptably low level by conservative reactor operations. In 1977, these operations reduced plant capacity by about 1 percent for pressurized water reactors (PWRs) and about 3 percent for boiling water reactors (BWRs), with extremes up to 6 percent for BWRs. The total cost in replacement power in the United States alone, therefore, currently runs at approximately over \$100 million/year and could rise to \$400 million/year by 1985 if the PCI problem is not resolved (2).

With this clear economic incentive to provide a remedy for PCI, many investigations have been undertaken to understand the mechanism(s) underlying Zircaloy cladding fracture and to define relevant material and operating variables.

Actually, the behavior of a fuel rod in the nuclear power reactor is complex. The behavior of the fuel itself is highly complicated, involving, for example, swelling, irradiation growth, fission products formation, cracking, relocation of fuel pellets, creep, fuel

densification, etc. Cladding behavior is similarly complicated, involving, for example, irradiation hardening, creep, collapse due to the external coolant pressure, environment interaction with the coolant, etc. The fuel and the cladding also interact and this involves frictional effects at the fuel-cladding interface, bonding between fuel and cladding, interactions of the inner cladding surface with fission products produced in the fuel, interfacial stresses generated during power increases, etc.

Despite this complexity, it is nevertheless essential that one should have a clear idea as to how a fuel rod will behave during its service life. An understanding of fuel rod behavior is vital with respect to fuel rod design and the optimum metallurgical condition of the fuel and cladding materials. In regard to the metallurgical conditions of the component materials, it is important to know, for example, how stress-relieved cladding compares to recrystallized cladding, the role of subtle changes in the cladding's microstructure and crystallographic texture.

No detailed, quantitative investigation has yet been reported of the anisotropy of subcritical crack growth for Zircalloys in simulated or actual nuclear environments containing iodine. Such work is needed to estimate the worst-case fuel cladding lifetimes for incorporation into reactor operation and safety codes.

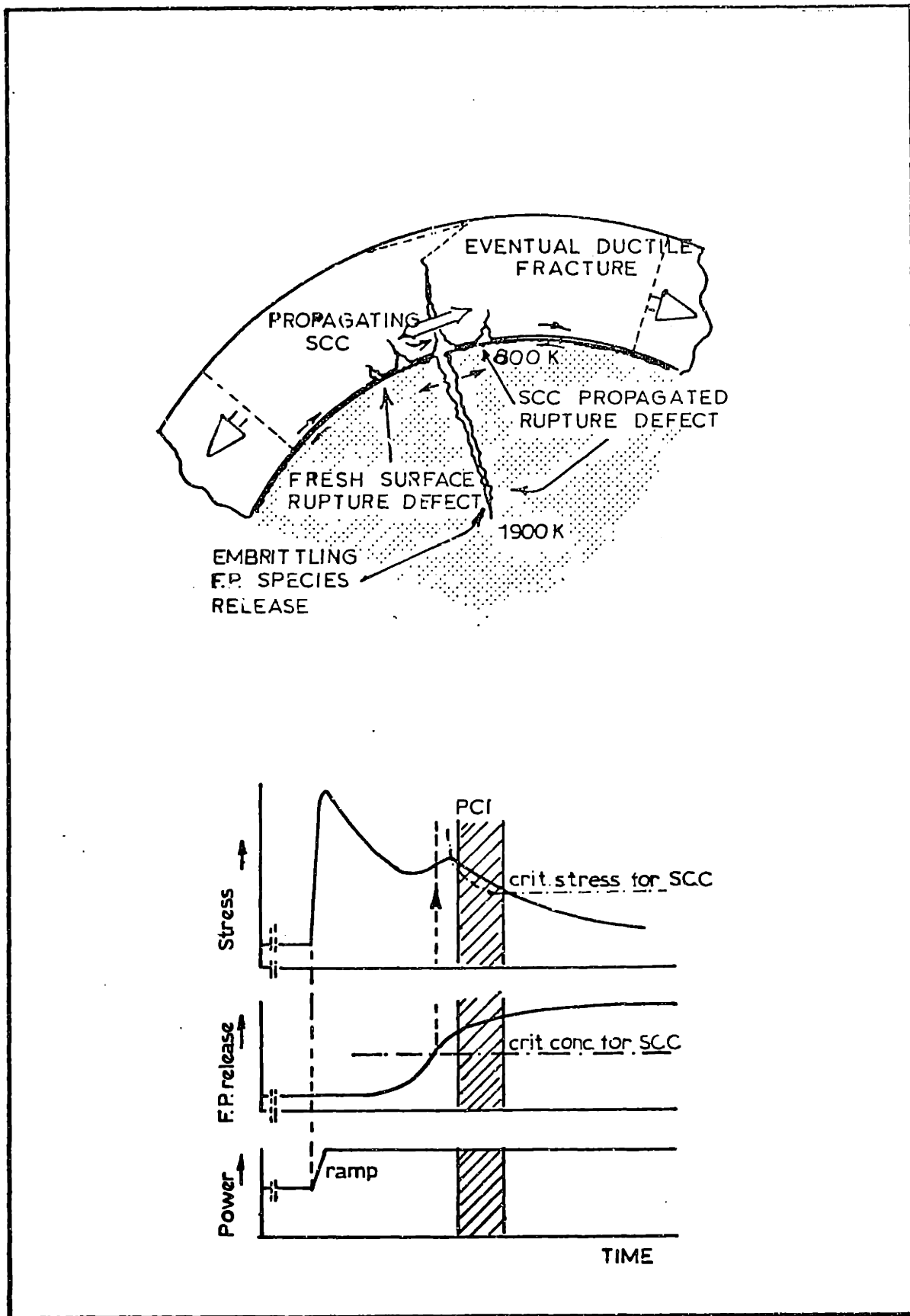


Figure 1.1 Schematic of PCI Zircaloy fuel rod mechanism

2. LITERATURE REVIEW AND BACKGROUND

2.1 Zirconium and Zirconium Alloys

The property of zirconium that makes it desirable for use in nuclear power reactors is its transparency to the passage of thermal neutrons that cause the fission of other uranium atoms with the evolution of heat. Besides that neutronic performance, zirconium alloys were developed to have an excellent resistance to corrosion by the high temperature (up to $\sim 350^{\circ}\text{C}$) water that transfers the heat away from the nuclear core. The alloys also have adequate strength and ductility in service.

Some of the widely used zirconium alloys are listed in Table 2.1. The Zircalloys have been developed for improved corrosion resistance and their typical use is in fuel cladding. The Zr-2.5Nb has been developed for higher strength and its typical use is in pressure tubes.

Generally, fuel-clad tubing for PWRs is used in a cold-worked and stress-relieved condition with the amount of cold-work and stress-relieving varying to produce the blend of strength and ductility desired by the reactor designers. Annealed Zircaloy generally is used for BWR cladding and other parts of the reactor system (3).

2.1.1 Deformation Mechanisms

The crystal structure of pure zirconium changes at 863°C from high-temperature β form, which is body-centered cubic, to the

low-temperature α form, which is hexagonal close-packed (hcp) with a c/a ratio of 1.593.

The first order prism plane slip system $\{10\bar{1}0\}\langle 1\bar{2}10\rangle$, shown in Figure 2.1, has the lowest critical resolved shear stress (i.e., CRSS is the stress necessary to initiate flow) and is the dominant slip system in α -zirconium and Zircaloy polycrystals deformed at temperatures below about 400°C. This makes the basal pole (0001) direction a hard direction of the crystal because slip primarily occurs perpendicular to the basal pole normal direction $\langle 0001\rangle$.

Basal slip of the form $\{0001\}\langle 1\bar{2}10\rangle$ has been observed only at high temperature to a limited extent (4).

The systems above mentioned all slip in the a-direction and therefore do not provide any displacement in the c-direction. Additional deformation systems are then required to achieve the change of shape needed to maintain grain boundary contact during plastic deformation of a polycrystal (five slip systems are required to satisfy a generalized shape change) (5).

Slip on the pyramidal planes $\{10\bar{1}0\}$ and $\{11\bar{2}1\}$ in the (c+a) direction is observed under constraint (a high stress concentration situation) and with increasing temperature (6).

Twinning is the most important factor in the plastic deformation in grains not oriented for $\{10\bar{1}0\}\langle 1\bar{2}10\rangle$ slip. Under tension along the $\langle 0001\rangle$ direction, $\{10\bar{1}2\}\langle 10\bar{1}1\rangle$ twins and less frequently $\{11\bar{2}1\}\langle 1\bar{2}6\rangle$ twins are called upon. Under compression in the same direction, $\{11\bar{2}2\}\langle 11\bar{2}3\rangle$ twins and at elevated temperatures, $\{10\bar{1}1\}$

$\langle 10\bar{1}2 \rangle$ twins are formed. The relative frequency and the thickness of the twins change with temperature, strain and the strain-rate.

The deformation systems that are active in Zircaloy between room temperature and 300°C are listed in Table 2.2 along with some other relevant information (7).

2.1.2 Relationship Between Fabrication and Texture

One consequence of the fabrication process of zirconium-based alloys is the development of a preferred orientation of the grains (crystallites) in the final product. This is called a crystallographic texture.

Crystallographic texture can be measured in several ways (8), the most convenient and common being the normal and inverse pole figure techniques; the former presents information on the intensity of the normals to a specific plane in all directions, while the latter displays the intensities of all planes in a specific direction.

Pole figures representing texture are drawn on a stereographic projection, which provides a two-dimensional plot in which the angular relationship between planes in the crystal are preserved. In a normal or direct pole figure, the center of projection represents an important direction such as the normal to the rolling plane of a plate or the radial direction in a tube, while an inverse pole figure represents the density distribution of poles lying in a specific direction (e.g., the plate rolling direction or the radial direction of the tube) drawn on a stereographic projection of the lattice in a

standard orientation.

Once the distribution of, say, the (0002) poles has been obtained it is desirable to convert it to an analytical form so that quantitative comparisons can be made between preferred orientation and bulk physical properties. A simple analytical method based on the averaging of single crystal strains was used by Kearns (9) in the formulation of an "f-parameter" to correlate thermal expansion and preferred orientation in Zircaloy-4. Appendix A describes the derivation and use of the f-number.

McGeary and Lustman (10) have determined the texture of a thin sheet of Zircaloy as a function of the fabrication history. The cold rolled texture consisted of basal planes parallel to the rolling plane, tilted approximately ± 30 degrees towards the transverse direction; no basal poles were observed in the rolling direction. Hot rolling below the recrystallization temperature did not change the final texture.

The texture formed by cross-rolling consisted of basal planes in the rolling plane with $\langle 10\bar{1}0 \rangle$ directions located in one direction in the sheet (rolling or transverse) and the $\langle 11\bar{2}0 \rangle$ directions located in the other direction.

Recrystallization of the cold-rolled texture resulted in a 30-degree rotation about the c-axis placing the $\langle 11\bar{2}0 \rangle$ direction in the rolling direction. Recrystallization of the cross-rolled texture resulted in a transfer of the $\langle 10\bar{1}0 \rangle$ and $\langle 11\bar{2}0 \rangle$ directions in the sheet.

The fabrication textures of zirconium alloy tube, plate, and rod has been extensively studied (6,7). In each case the texture, which becomes stable after as little as 20 percent reduction, consisted of basal planes parallel to the direction of maximum tensile strain and basal poles predominantly in the direction of maximum compressive strain, Figure 2.2.

The formation and stability of the observed texture can be explained in a simple way if, in the deformation process one takes into account a $(c+a)$ slip mechanism (11) in addition to prism slip and $\{10\bar{1}2\}$ twinning. The formation of the initial texture is the result of the twinning operation which rotates the basal pole by 85 degrees. Figure 2.3 shows the rotations affected by the twins observed in zirconium alloys.

2.2 Morphological and Microstructural Features of Iodine Stress

Corrosion Cracking in Zircalloys

The only features which give a unique indication of the occurrence of SCC in the Zircalloys are the flat cleavage planes. No other conditions (e.g., fracture at low temperatures, low ductility tensile failure after irradiation, etc.) give rise to cleavage in Zircalloys. Fractures always show ductile features when mechanically induced.

During stress corrosion, cleavage of zirconium alloys is prominent only on planes near the basal plane (11a); it is, therefore, unlikely that a fracture surface produced by transgranular SCC of hcp metals

will consist entirely of cleavage planes. In a polycrystalline sample, without a very highly textured structure, there is a high probability of some grains not being oriented so as to permit cleavage.

Since cleavage occurs on planes near the basal plane, there will be little constraint normal to the basal plane and deformation will occur predominantly by slip, on planes in the $\{10\bar{1}0\} \langle 11\bar{2}0 \rangle$ system. There will, therefore, be little thinning of the slabs of material between parallel cleavage cracks because slip occurs in directions parallel to the basal plane, i.e., almost parallel to the crack planes. Moreover, the ridges left by necking will have the direction defined by the intersection of such slip planes, i.e., the striations will be parallel to each other and normal to the basal plane, Figure 2.4.

Aitchison and Cox (13) suggested the term "fluted" for a fracture produced in this way, and "fluting" for the features themselves. They demonstrated by precise matching of identical features on mating fracture surfaces that flutes are the ruptured halves of tubular voids, resulting like ordinary irregular microvoids from internal necking by slip, which in the case of flutes is substantially restricted to the $\frac{1}{2}\{10\bar{1}0\} \langle 11\bar{2}0 \rangle$ system. Spurrier and Scully (14) reached substantially similar conclusions.

In the absence of corrosive environment there is an increasing tendency for intergranular fracture of metals rather than transgranular fracture when one increases the temperature and decreases the strain rate (15). Wood et al. (16) found no such

correlation exists for iodine-induced SCC over a range of strain rates (10^{-3} - 10^{-7} sec $^{-1}$) and temperatures (225-550°C). What they observe is transgranular cleavage at low strain rate, a mixture of failure modes at intermediate strain rates, and ductile fracture (most likely transgranular but of an entirely different process from transgranular cleavage) at high strain rates.

2.3 Mechanism of Iodine-Induced SCC of Zircaloy Cladding

A laboratory approach to fuel rod cracking requires an assumed model of the failure mechanism.

Based on experimental results, Cubicciotti et al. (17) have developed a model for iodine SCC of thin-walled Zircaloy tubes. The model consists of four stages, namely: 1) oxide penetration, 2) crack formation, 3) crack propagation, and 4) cladding rupture. The model is illustrated in Figure 2.5; it is similar to that proposed by Cox and Wood (18). Each stage is summarized below.

(1) Oxide Penetration

Zirconium alloys exposed to oxygen-containing environments at the temperatures of importance for LWR operation are always covered with an oxide film. The thickness of this film is determined by the conditions of temperature and oxygen pressure preceding exposure to iodine vapor. For a specimen in a laboratory SCC test this oxide film will normally be only 50-150 Å thick at room temperature, and if the specimen is then heated in typical "vacuum" of 10^{-3} Torr to a temperature of 300-400°C in the presence of iodine it is unlikely that

a thickness of greater than a few hundred Angstroms will be reached before SCC occurs. At the other extreme, the inside of Zircaloy fuel cladding may exhibit an oxide film a few microns in thickness resulting from oxidation by residual oxygen in the fuel element, and oxygen released by the UO_2 fuel during irradiation.

Iodine is capable of penetrating thin air formed oxide films in the absence of an applied stress but a strain threshold of a few tenths of one percent must be exceeded (17) to mechanically fracture the oxide before iodine can penetrate films with thickness in the micron range.

Because the threshold stress for iodine SCC of annealed Zircaloy in tube pressurization experiments is well above the stress required to fracture the oxide, oxide penetration is not believed to be the critical step in the overall iodine SCC process and also in PCI failures of nuclear fuel cladding.

(2) Crack Formation

Cracking of the protective oxide film exposes a small area of Zircaloy metal surface in the metal-oxide interface to the iodine-containing environment. If the applied stress is sufficiently large, stress corrosion crack nucleation then occurs at certain favored sites in the exposed metal surface.

Cubicciotti et al. (17) think that the threshold stresses observed in tube pressurization tests are associated with crack formation because the minimum stress for continued crack growth of a preexisting stress corrosion crack is expected to decrease with increasing crack

depth. Therefore, they regard crack formation as the critical step in the iodine-induced failure of internally pressurized Zircaloy tubes. The exact mechanism of crack formation is uncertain.

(3) Crack Propagation

Once a stress corrosion crack has been initiated, crack growth will occur if the stress remains above the threshold and the specimen continues to be exposed to a sufficiently aggressive environment; the results of Busby et al. (19) indicate that the minimum iodine concentration required for SCC is less than $.005 \text{ mg/cm}^2$.

Crack propagation occurs by a mixture of cleavage and ductile tearing (fluting) in stress-relieved materials but may involve intergranular processes in unirradiated, recrystallized material.

(4) Cladding Rupture

Stress corrosion crack propagation continues until plastic instability occurs, resulting in rapid, ductile fracture of the uncracked ligament ahead of the crack, usually on a shear surface.

2.4 Chemical Aspects of the I-SCC of Zircaloy

Thermochemistry of the Zirconium-Iodine System

Recent thermodynamic data by Cubicciotti et al. (20) lead to the conclusion that solid iodides on the Zircaloy surface are involved in the mechanism of iodine-induced SCC. It is shown that ZrI_4 must be the gaseous species involved in any mechanism of iodine SCC of Zircaloy in which vapor transport is important.

2.4.1 Gaseous Iodides

Kleinschmidt et al. (21) have used a mass spectrometer method to measure the partial pressures of the gaseous iodides in equilibrium with zirconium metal. From these results, the enthalpies of formation of gaseous ZrI_3 , ZrI_2 , and ZrI were derived. Table 2.3 summarizes the thermodynamic data, and Figure 2.6 gives the pressure of the ZrI_4 gas in equilibrium with zirconium metal.

For temperatures typical of Zircaloy cladding inner surfaces in LWR operation ($\sim 350^\circ\text{C}$), the only important gaseous species containing Zr is ZrI_4 . As $P(\text{total I})$ decreases, the lower iodides become more important relative to ZrI_4 ; however, at 350°C the gases dissociate to iodine before this can happen. Therefore, any mechanism for iodine-induced SCC of Zircaloy that involves transport of Zr must invoke primarily ZrI_4 .

2.4.2 Kinetics of Formation of Solid Iodides on Zirconium

The reaction of zirconium with gaseous ZrI_4 in the temperature range $300\text{-}500^\circ\text{C}$ was studied by Cubicciotti and Scott (22). The initial experiments in their study were made with iodine and zirconium but the presence in the reaction products of more than two phases with different compositions in close contact implied that the system was far from equilibrium. Subsequent experiments were made with ZrI_4 instead of iodine, and with the ZrI_4 maintained at lower temperatures than the zirconium. Under these conditions the effective

iodine partial pressure was much smaller and more uniform layers of reaction products were formed.

The first few experiments were made to determine the conditions for obtaining measurable surface layers of reaction products. Under mild conditions (i.e., low zirconium temperature and small ZrI_4 pressure) clusters of acicular ZrI crystals grew from isolated spots; the surface between the clusters was covered with a thin film that contained iodide. Analysis of these films indicated I/Zr ratios of the order of 0.1 or smaller which probably resulted from a layer of ZrI that was less than $1 \mu m$ thick.

As the conditions became more severe the density of each cluster increased and the number of clusters per unit area also increased until the surface became completely covered by a layer of ZrI . Additional attack led to the formation of a layer of diiodide (about ZrI_2) on top of the ZrI . Further attack produced material of approximately composition of the triiodide (about $ZrI_{2.7}$) on top. The highest iodide that could form was a function of the pressure of the ZrI_4 gas and the temperature of the sample; it corresponded to the equilibrium composition for the solid under those conditions.

The presence of a preformed oxide film on the surface might be expected to act as a barrier to the reaction between the metal and the gaseous ZrI_4 . Accordingly, several experiments were made with preformed oxide film. Oxide layers less than $0.2 \mu m$ thick on the zirconium surface had no effect on the rate of the reaction with gaseous ZrI_4 but an oxide layer about $4 \mu m$ thick slowed the reaction

markedly; however, the reaction was not completely stopped as evidenced by the presence of some ZrI crystals on the surface.

Cubiciotti and Scott (22) also investigated the reaction as a function of time. They indicate that the formation of the surface iodide layers involves several steps:

(1) A thin layer of iodide is formed and clusters of acicular ZrI crystals grow from that surface.

(2) The clusters of crystals increase in density until the surface becomes covered with a layer of ZrI.

(3) Further reaction leads to the formation of a layer of approximately diiodide on top of the monoiodide. The diiodide layer has a columnar structure that appears to be porous. With additional reaction there is evidence for the formation of triiodide.

In summary, zirconium iodides (ZrI_n) with n from 1 to 4 are known. Each of these iodides exists over a range of stoichiometries. The extent of non-stoichiometry is shown in Figure 2.7. These limits should vary somewhat with temperature, but the variation might be small, as found by Daake and Corbett (23) for the triiodide.

2.5 The Effect of Tensile Stress on I-SCC of Zr Alloys

Recently, Syrett et al. (24) have studied the effect of axial stress to hoop stress ratio (σ_a/σ_h) on the SCC susceptibility of Zircaloy. The ratio of applied axial stress to applied hoop stress was varied in the tests between zero and infinite by axially loading the pressurized specimens. They observed the time to failure as a

function of initial stress ratio and initial hoop stress, and showed that a stress ratio of zero, pure hoop tension, is associated with maximum susceptibility to SCC, no matter what is the hoop stress value (Figure 2-8).

2.6 Metallurgical Factors Controlling Cracking

Metallurgical parameters which can have an influence on the SCC of zirconium alloys are crystallographic texture, residual stress, heat treatment, surface condition, and irradiation.

Experiments by Wood (25) demonstrated that residual stress in the cladding can be more important than cold-work in determining the susceptibility to stress corrosion cracking. Since the two properties generally change in unison during fabrication the effect of one may be misinterpreted as resulting from the other. To distinguish between them, Wood has eliminated residual stress by two methods, one of which (annealing) also decreases the cold work, while the other (hydraulic straining) simultaneously increases cold-work. Both techniques resulted in specimens resistant to SCC when the residual stress had been removed.

Surface condition may influence the surface reactivity which may, in turn, affect the susceptibility to iodine SCC, but the precise interaction between surface condition and SCC (if any) is not currently known (26).

Irradiation, in general, increases the susceptibility of Zircaloy to iodine-induced SCC failures (27). This is evidenced by an almost 50 percent reduction in threshold stress and also a substantial

reduction in t_f (time to failure) for hoop stresses above the threshold stress as illustrated in Figure 2.9. There are a number of mechanisms by which irradiation can be conceived to affect SCC susceptibility; most involve local dislocation channeling and consequent plastic flow concentrations (28).

2.6.1 Influence of the Crystallographic Texture

Following the method described by Tenckhoff (29), Peehs et al. (30) machined seamless tubes from a thick, strongly textured Zircaloy plate. Thus they obtained tubing in which the basal pole texture ranged from strongly radial to strongly tangential at a 90° interval along the circumference. After pressurizing these tubes in the presence of iodine, they obtained the density of stress-corrosion-induced microcracks, and found that the density was a function of circumferential position as shown in Figure 2.10. All cracking is contained in regions in which the peak basal pole intensity is within about 45° of the tangential direction. No cracking was observed in regions where the basal pole texture was strongly radial and the maximum susceptibility lies in regions where most of the basal poles are inclined at 10 to 30° to the tangential direction rather than in the most tangential regions.

Syrett et al. (26) compared the susceptibilities to iodine SCC for two lots of Zircaloy tubing manufactured by different suppliers, using closed end tube pressurization tests at 320°C . The tubing from one supplier (supplier B) was found to have a lower SCC threshold stress

and failed more quickly than the tubing from the other supplier (supplier A). In reviewing the results of the tests, the following observations were made: the maximum intensity of basal poles was at about $\pm 30^\circ$ to the radial direction for supplier A's tubing and at about $\pm 42^\circ$ to the radial direction for supplier B's tubing. Even more important than the positions of the basal pole maxima were the intensities of the basal pole intensity about 20° from the tangential direction was less than the random level in supplier A tubing, whereas in supplier B's tubing, the intensity reached as high as about 2.5 times random. They conclude that the greater the tangential texture of the fuel cladding, the greater the susceptibility to SCC. Earlier experimental performed by Garlick (31) also lend support to this view.

Knorr and Pelloux (32) performed SCC tests on fracture mechanics specimens machined from different orientations in plates having two different textures. They found that texture has a strong influence on K_{ISCC} (the threshold K_I value for SCC) as shown in Figure 2.11.

2.7 Fracture Mechanics Approach to I-SCC Growth in Zirconium Alloys

Cox and Wood (18) measured the rate of crack propagation in Zircaloy-2 exposed to iodine vapor at 300°C . Using precracked double cantilever beam (DCB) specimens, they found that the crack velocity is sensitive to the stress intensity factor at the crack tip.

Fractography showed only transgranular fracture.

Iodine stress corrosion experiments done by Videm and Lunde (35) with tubing specimens with fatigue cracks of varying sizes showed that

SCC growth can be satisfactorily expressed as a function of the stress intensity factor. The rate of crack growth increased with the stress intensity factor to the ninth power. No threshold was found for crack growth but the rate became insignificant at low stress intensities.

Table 2.1

Designation and Composition of Some Important Zirconium Alloys

Sn	Chief Alloying Elements (wt.-percent)					Other	Balance
	Fe	Cr	Ni	Nb			
Alloy designation: Zr, unalloyed Zr, 702:							
-	-	-	-	-	-	= 2 percent Hf	Zr
Alloy designation: Zr, reactor grade Zr:							
-	-	-	-	-	-	Hf 0.01 max	Zr
Alloy designation: Zircaloy-2 ¹ :							
1.20- 1.70	0.07- 0.20	0.05- 0.15	0.03- 0.08	-	-		Zr
Alloy designation: Zircaloy-4 ² :							
1.20- 1.70	0.18- 0.24	0.07- 0.13	0.007 max	-	-		Zr
Alloy designation: Zr-2.5 percent Nb:							
0.001 max	0.08	0.01	0.003	2.5	-		Zr
Alloy designation: Ozhennite-0.5:							
0.2	0.1	0.02 max	0.1	0.1	-		Zr
Alloy designation: Zr-0.8 percent Cr:							
-	-	0.83	-	-	-	480 ppm O ₂	Zr
Alloy designation: Zr-Nb-Cu:							
-	-	-	-	-	-	0.5 percent Cu	Zr

Notes: 1. Sum of Fe, Ni, Cr in Zircaloy-2 must range between 0.18 and 0.38 percent.

2. Sum of Fe and Cr in Zircaloy-4 must be 0.28 percent min.

Table 2.2
Deformation Systems in Zircalloys

Type	Plane	Crystal Direction	Twin Shear	Change in c-axis	CRSS Ratios	
					Single Crystal	Polycrystal ^a
For all temperatures and stress ranges:						
Slip	Prism	$\{10\bar{1}0\}\langle 1\bar{2}10\rangle$	-	-	1	1
High temperatures:						
Slip	Basal	$\{0001\}\langle 1120\rangle$	-	-	25	-
Intermediate temperatures, high stress:						
Slip	Pyramidal	$\{10\bar{1}1\}\langle 11\bar{2}3\rangle$	-	-	25	2.00 3.40
High temperature, high stress:						
Slip	Pyramidal	$\{11\bar{2}1\}\langle 1\bar{2}13\rangle$	-	-	-	-
Intermediate temperature, c-axis tension:						
Twin	Pyramidal	$\{10\bar{1}2\}\langle 10\bar{1}1\rangle$	0.167	84.22	0.26	1.64 1.25 1.50 0.60 1.55
Low temperature, c-axis tension:						
Twin	Pyramidal	$\{11\bar{2}1\}\langle 11\bar{2}6\rangle$	0.630	34.84	0.34	1.35 0.50
Low-intermediate temperature, c-axis compression:						
Twin	Pyramidal	$\{11\bar{2}2\}\langle 11\bar{2}3\rangle$	0.225	64.22	0.35	2.00 2.03 1.45
Intermediate-high temperature, c-axis compression:						
Twin	Pyramidal	$\{10\bar{1}1\}\langle 10\bar{1}2\rangle$	0.104	57.05	-	-

^aFrom different investigations.

Table 2.3

Thermochemical Data for Gaseous Iodides

Reaction	H_{298}^0 (kcal/mole)	Derived enthalpies of formation (kcal/mole)
$\frac{3}{4} \text{ZrI}_4(\text{g}) + \frac{1}{4} \text{Zr}(\text{s}) = \text{ZrI}_3(\text{g})$	32.6 ± 1.1	$\text{Hf}_{298}^0(\text{ZrI}_{3,\text{g}}) = -31.1 \pm 1.9$
$\text{ZrI}_4(\text{g}) = \text{ZrI}_3 + \text{I}(\text{g})$	79.8 ± 1.5	$\text{Hf}_{298}^0(\text{ZrI}_{3,\text{g}}) = -30.6 \pm 3.2$
$\text{ZrI}_2(\text{g}) = \text{ZrI}_4(\text{g}) = 2\text{ZrI}_3(\text{g})$	-9.3 ± 3.5	$\text{Hf}_{298}^0(\text{ZrI}_{2,\text{g}}) = -32.6 \pm 4.0$
$\text{ZrI}(\text{g}) = \text{Zr}(\text{g}) + \text{I}(\text{g})$	72.6 ± 2.5	$\text{Hf}_{298}^0(\text{ZrIg}) = 96.3 \pm 2.8$

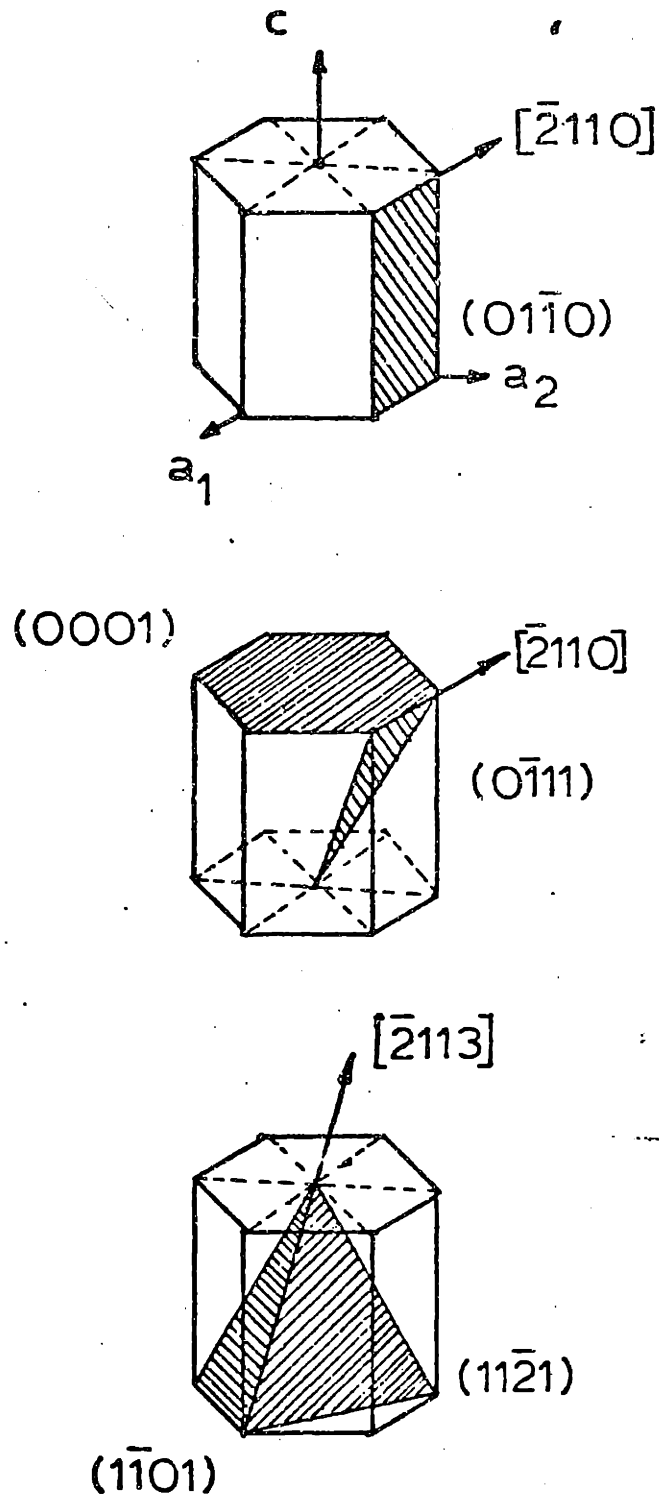


Figure 2.1 Slip systems in α -Zirconium

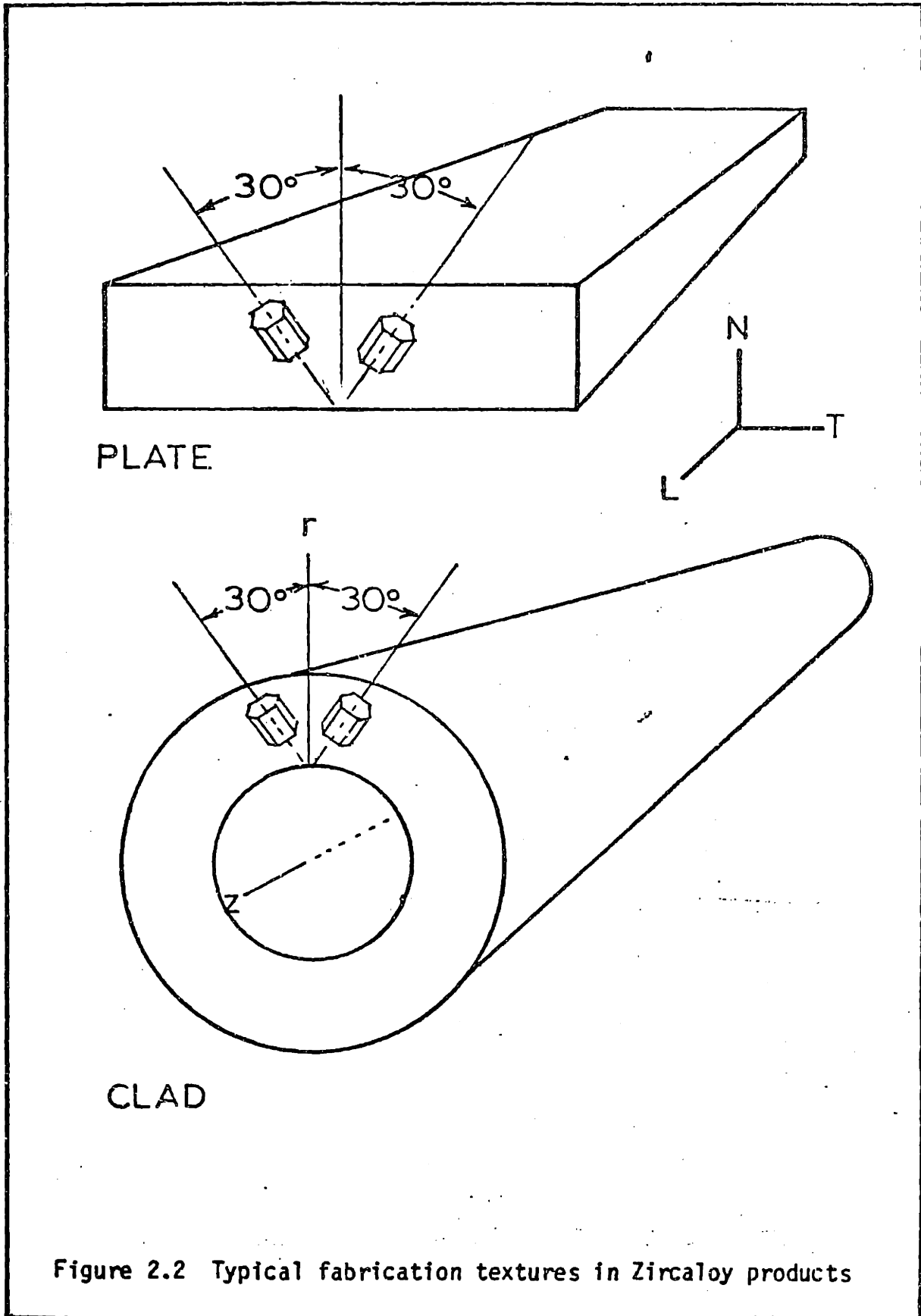


Figure 2.2 Typical fabrication textures in Zircaloy products

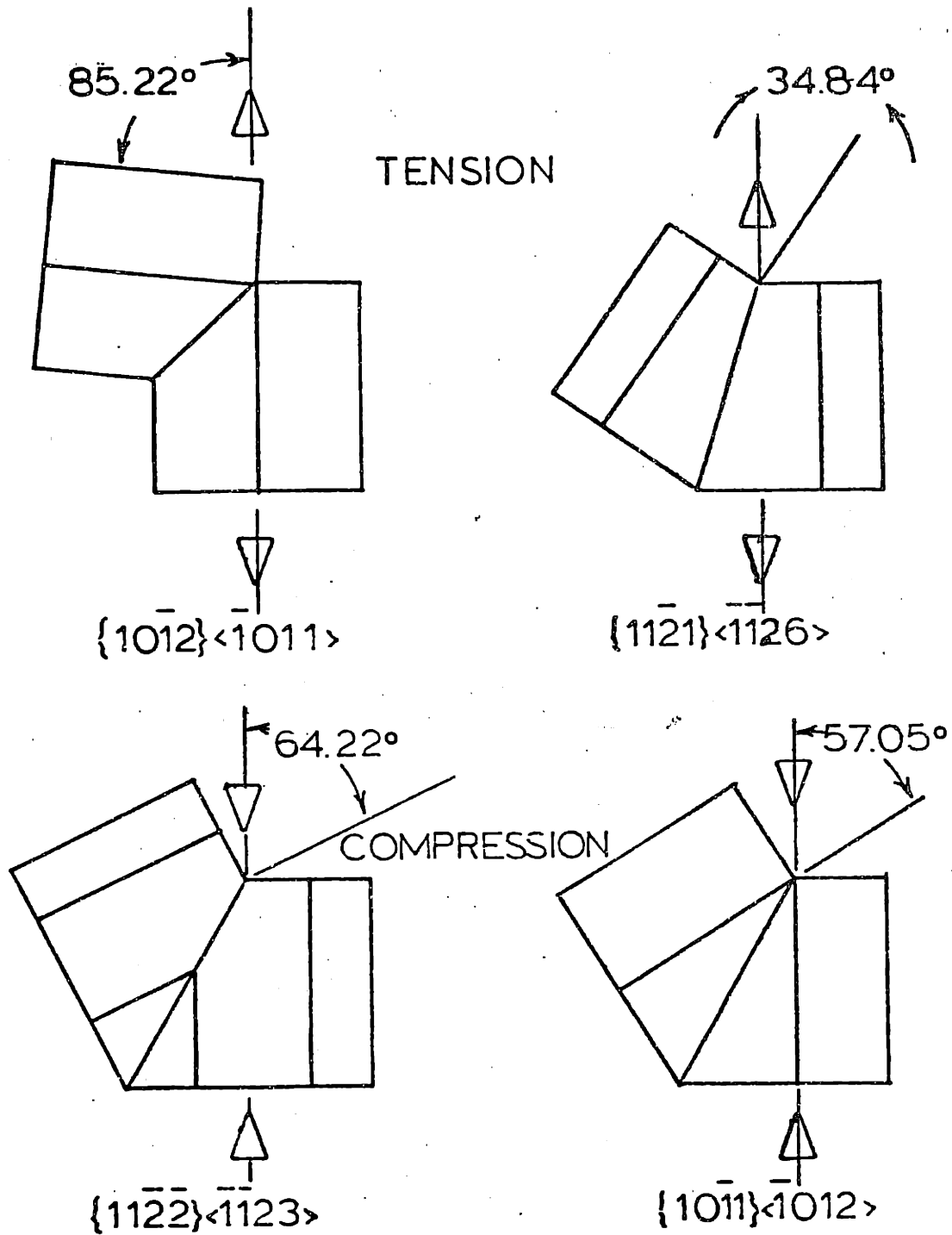


Figure 2.3 Twinning systems in α -Zirconium

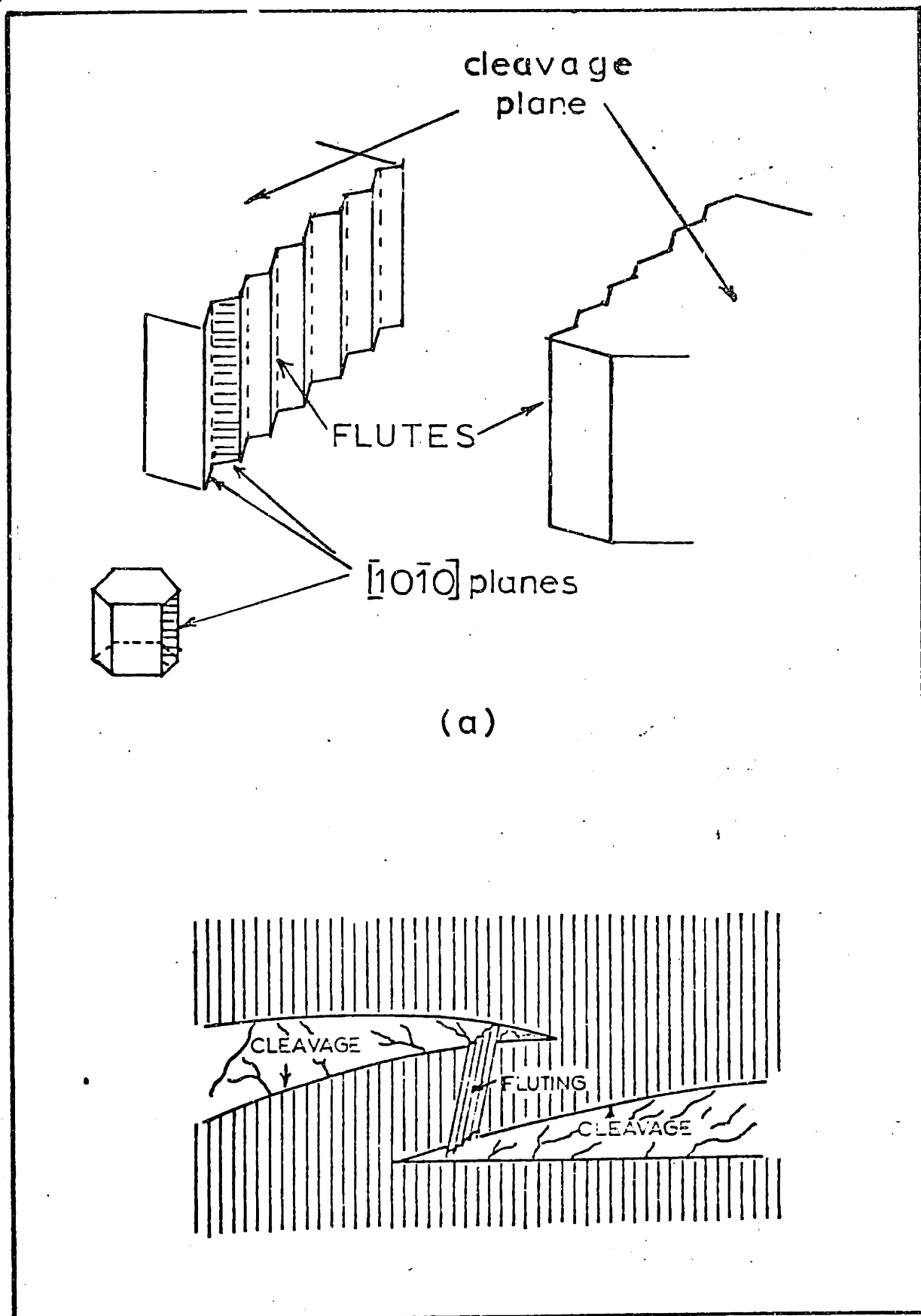


Figure 2.4 (a) Schematic of "fluting", (b) Tearing between overlapping cleavage regions illustrating flute mechanism

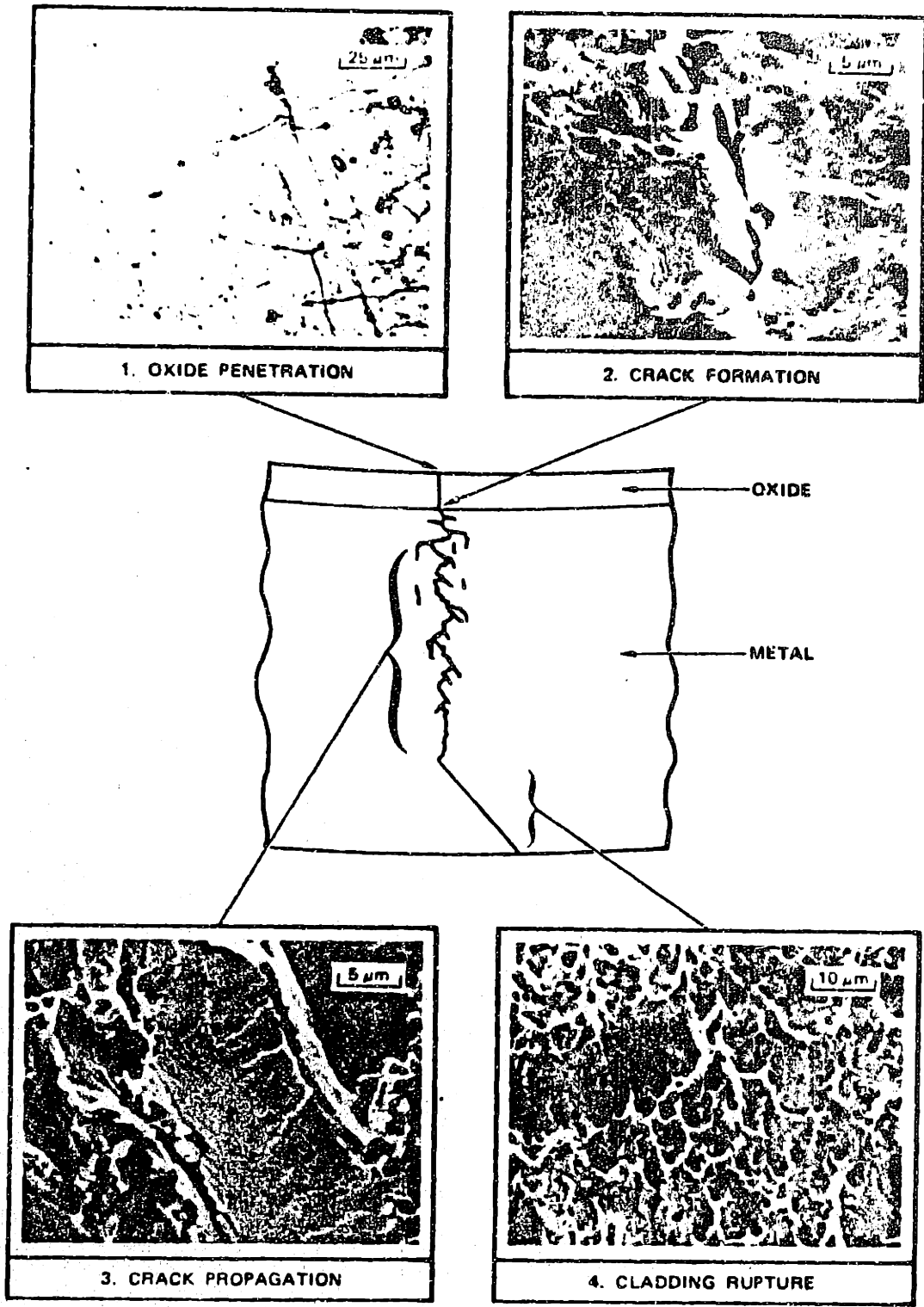


Figure 2.5 The four states of iodine-induced cladding failure

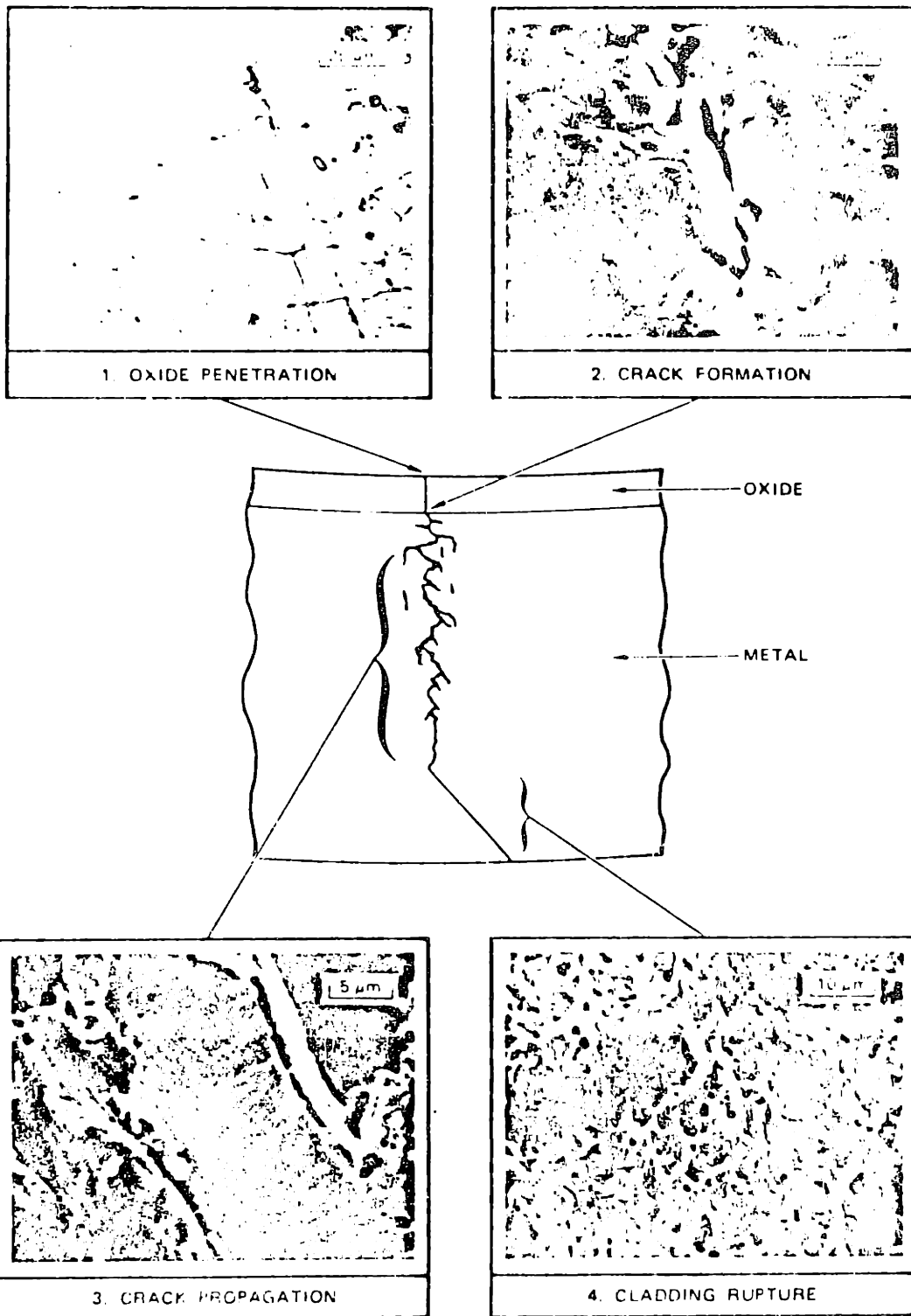


Figure 2.5 The four states of iodine-induced cladding failure

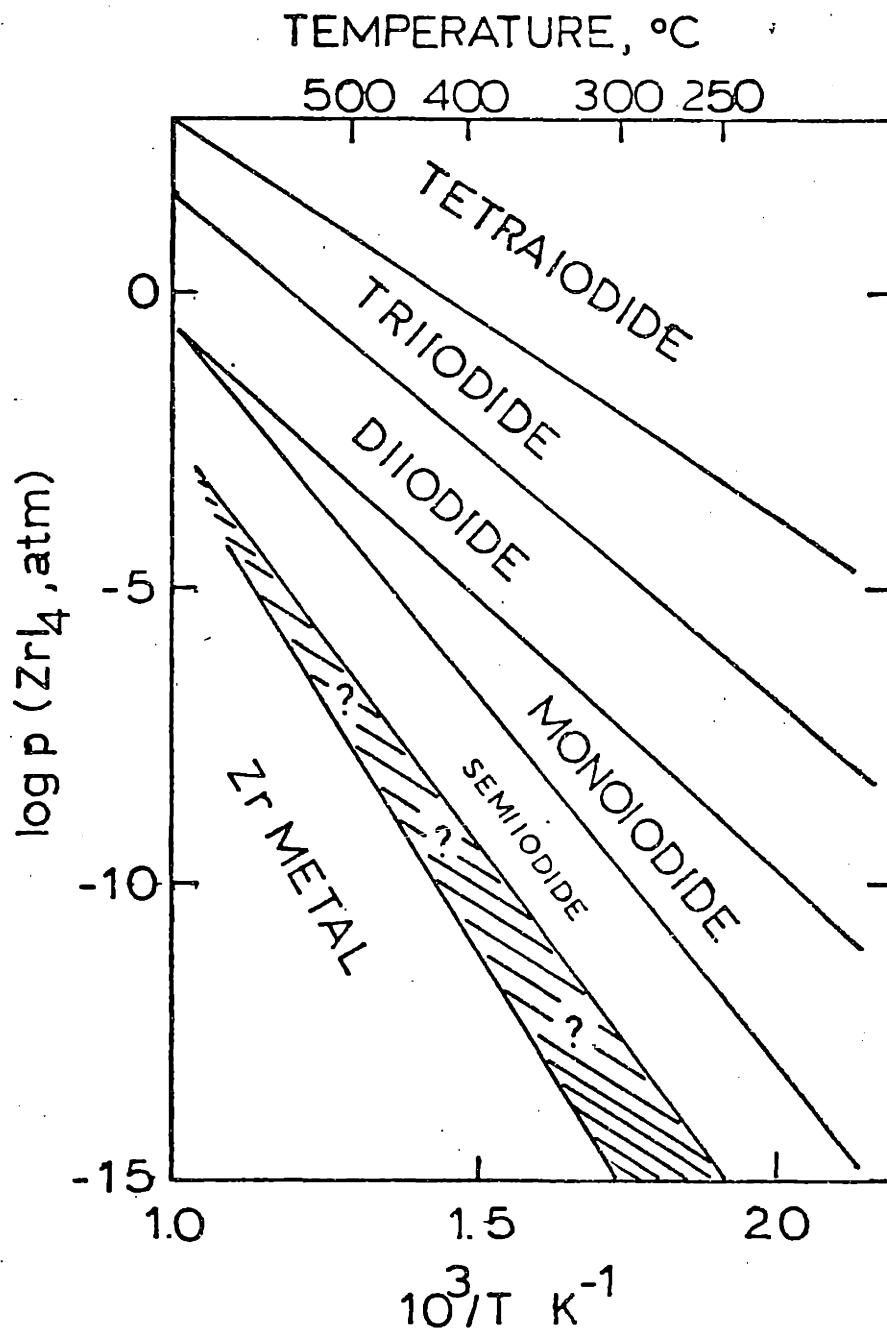


Figure 2.6 Pressures of ZrI_4 in gas in equilibrium with solid zirconium iodide phases. The shaded area indicates the probable location of chemisorption curves for iodine on zirconium

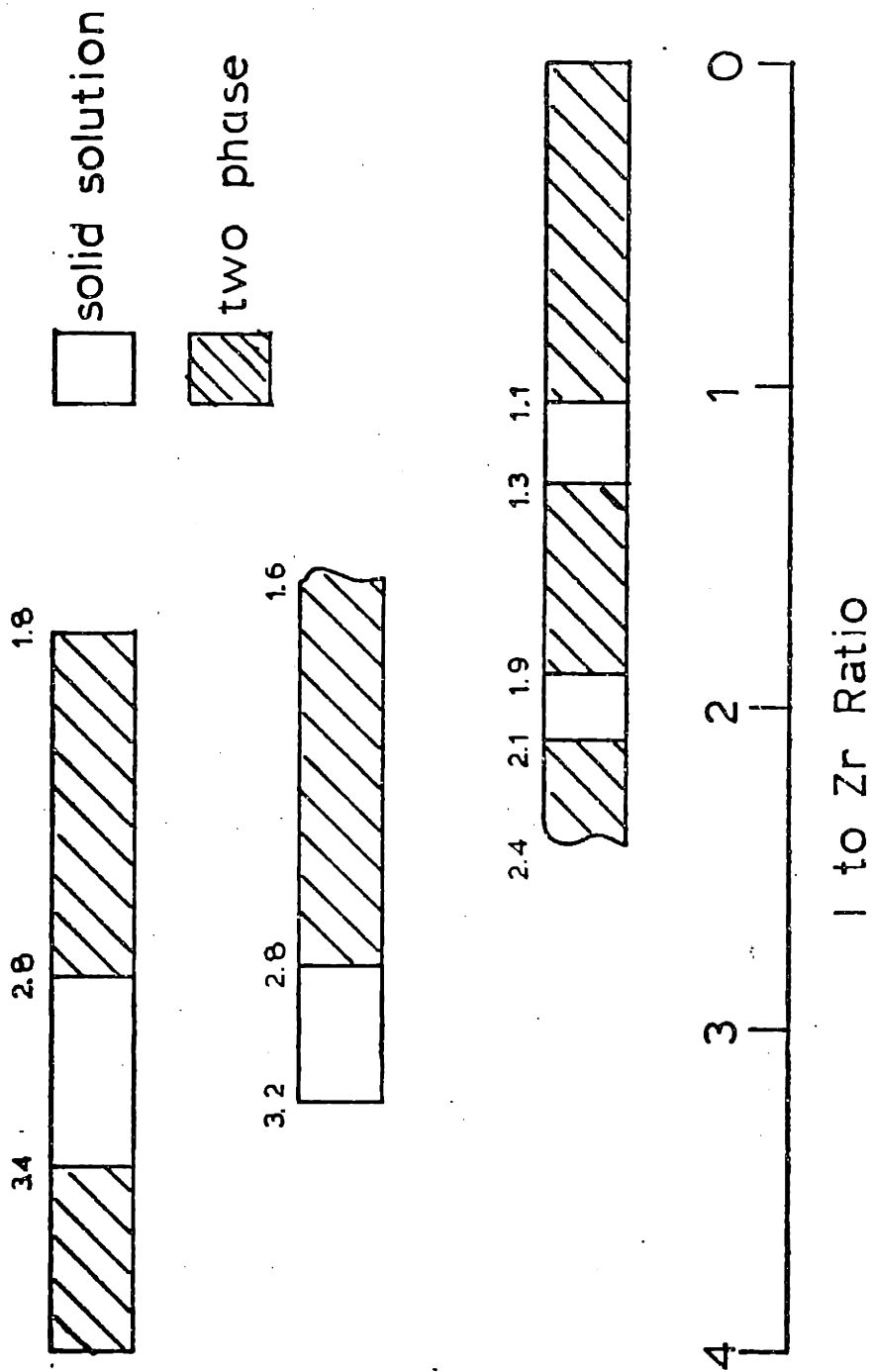


Figure 2.7 Compositions of Zr/I phase stability

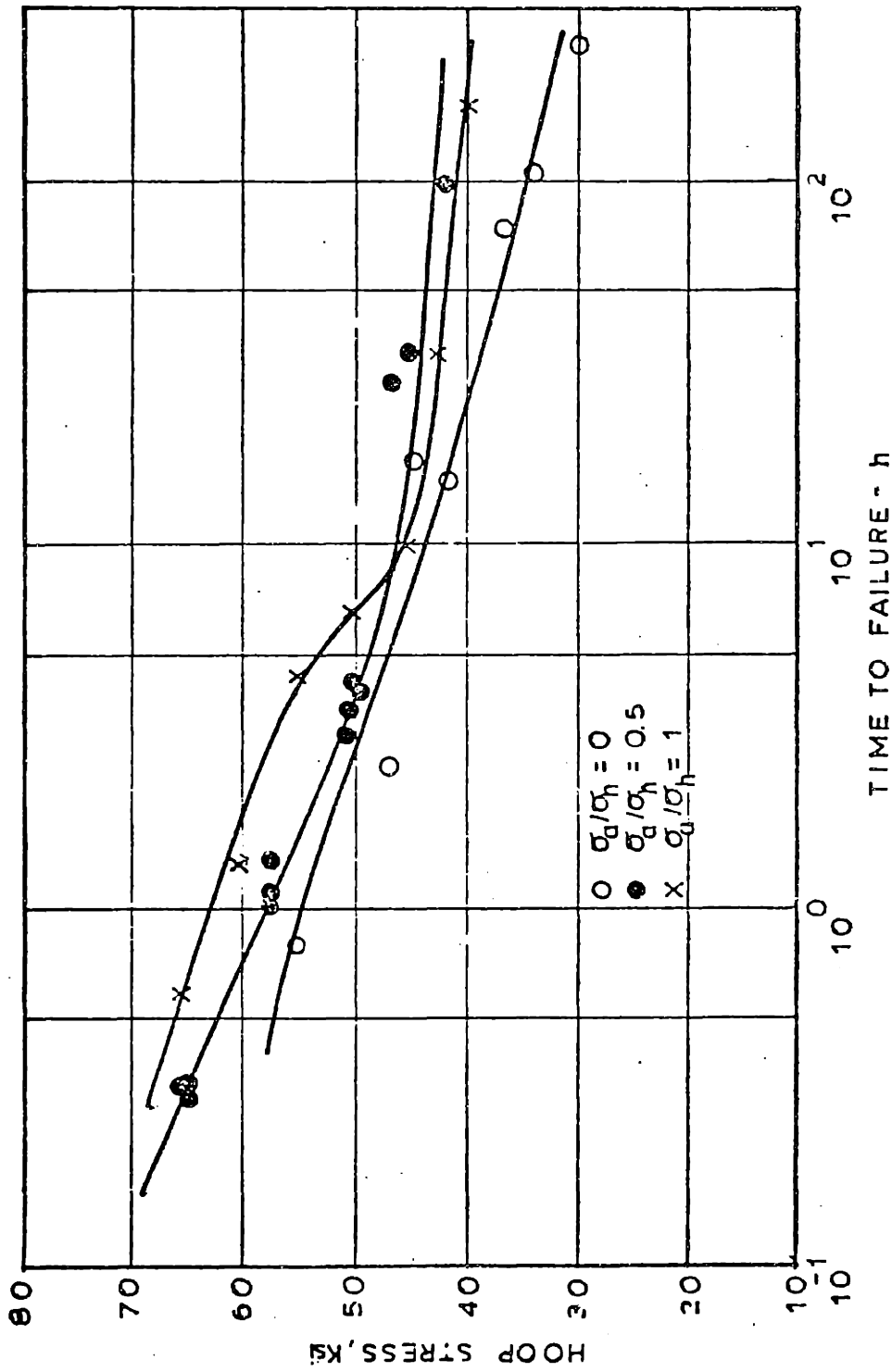


Figure 2.8 Hoop stress vs. time-to-failure for Zircaloy-4 exposed to iodine at 360°C

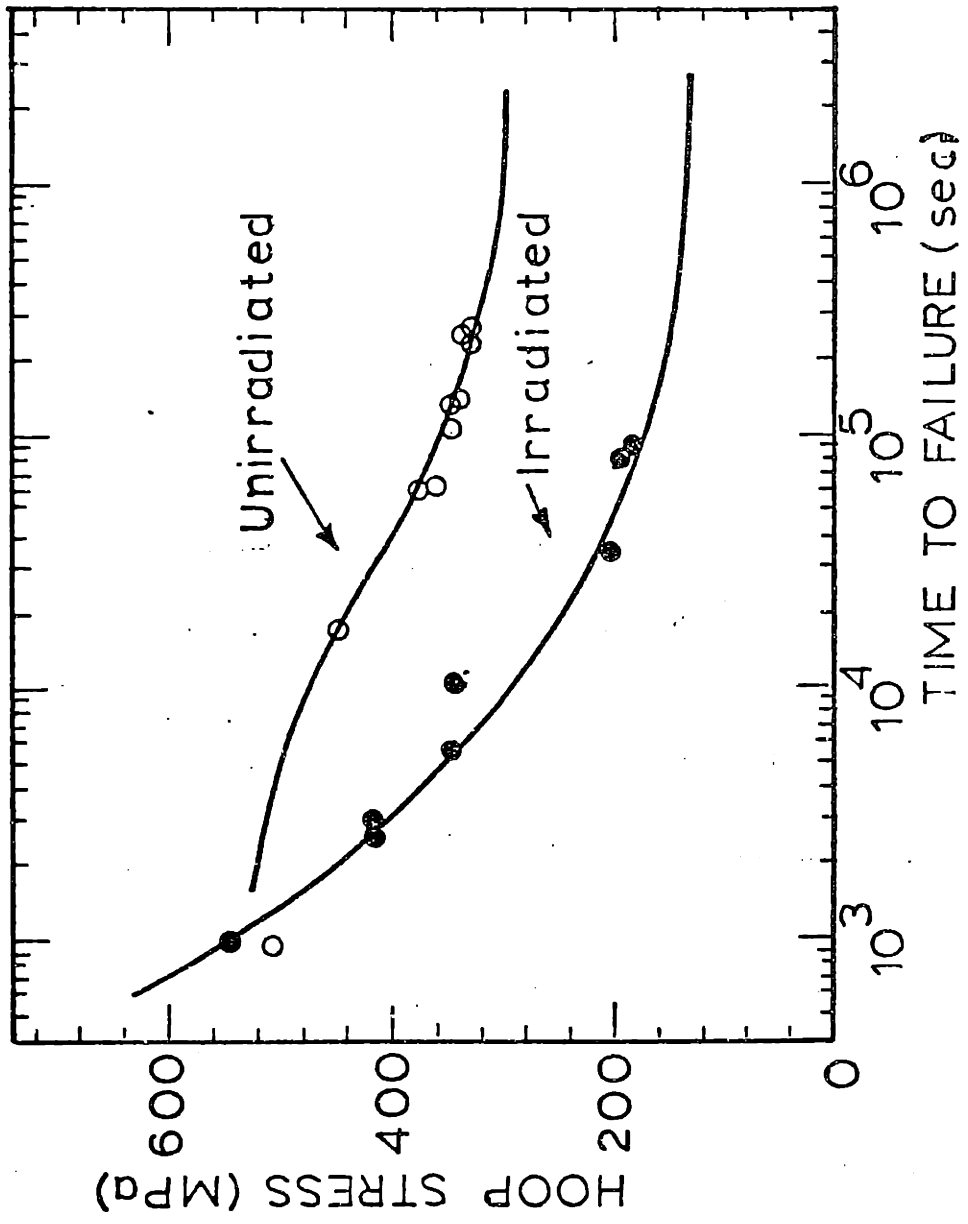
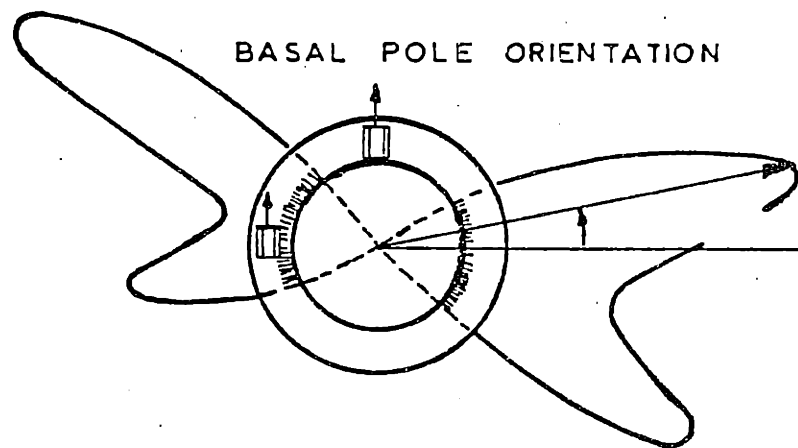
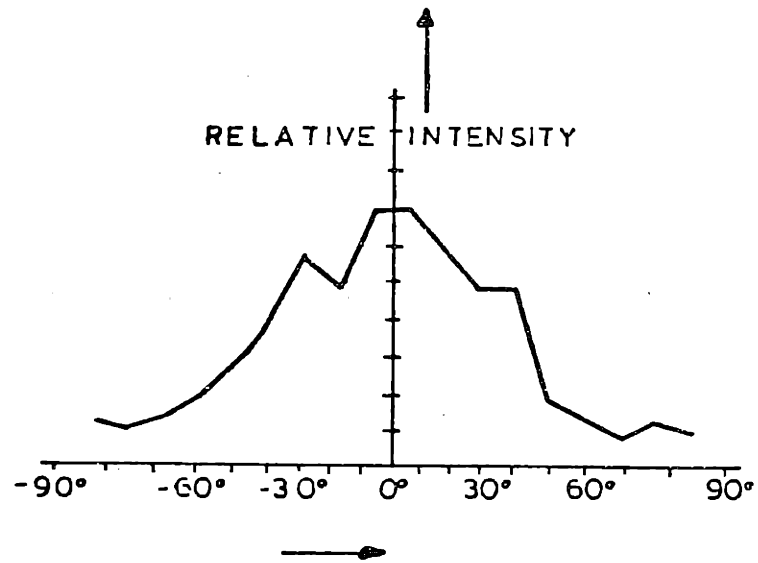


Figure 2.9 Effect of irradiation on time to failure vs hoop stress for Zircaloy at ~320°C



ANGULAR DISTRIBUTION OF
CRACK DENSITY

Figure 2.10 Relation between basal pole orientation and crack density

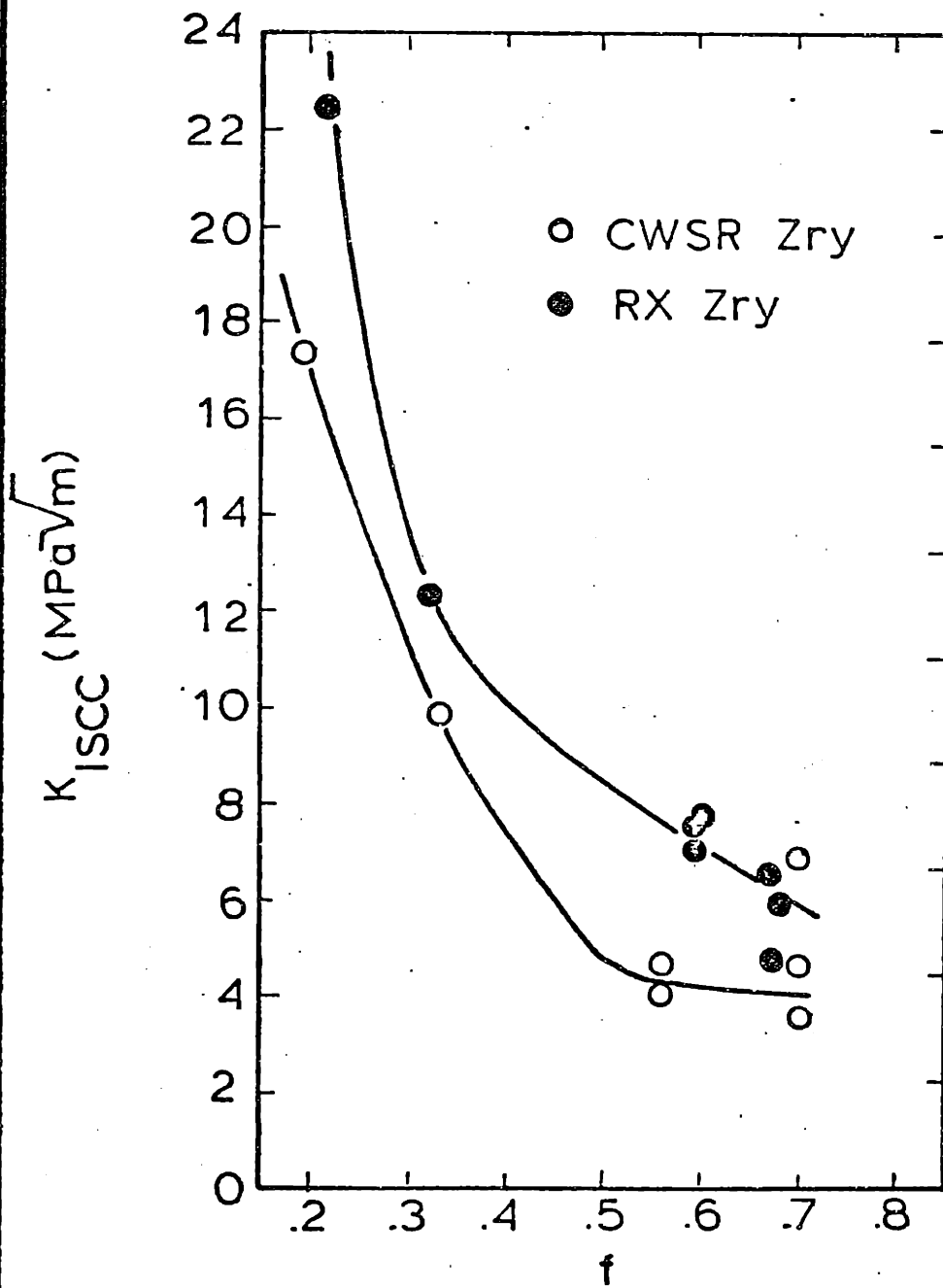


Figure 2.11 Effect of crystallographic texture on $K_{I SCC}$ in Zircaloy

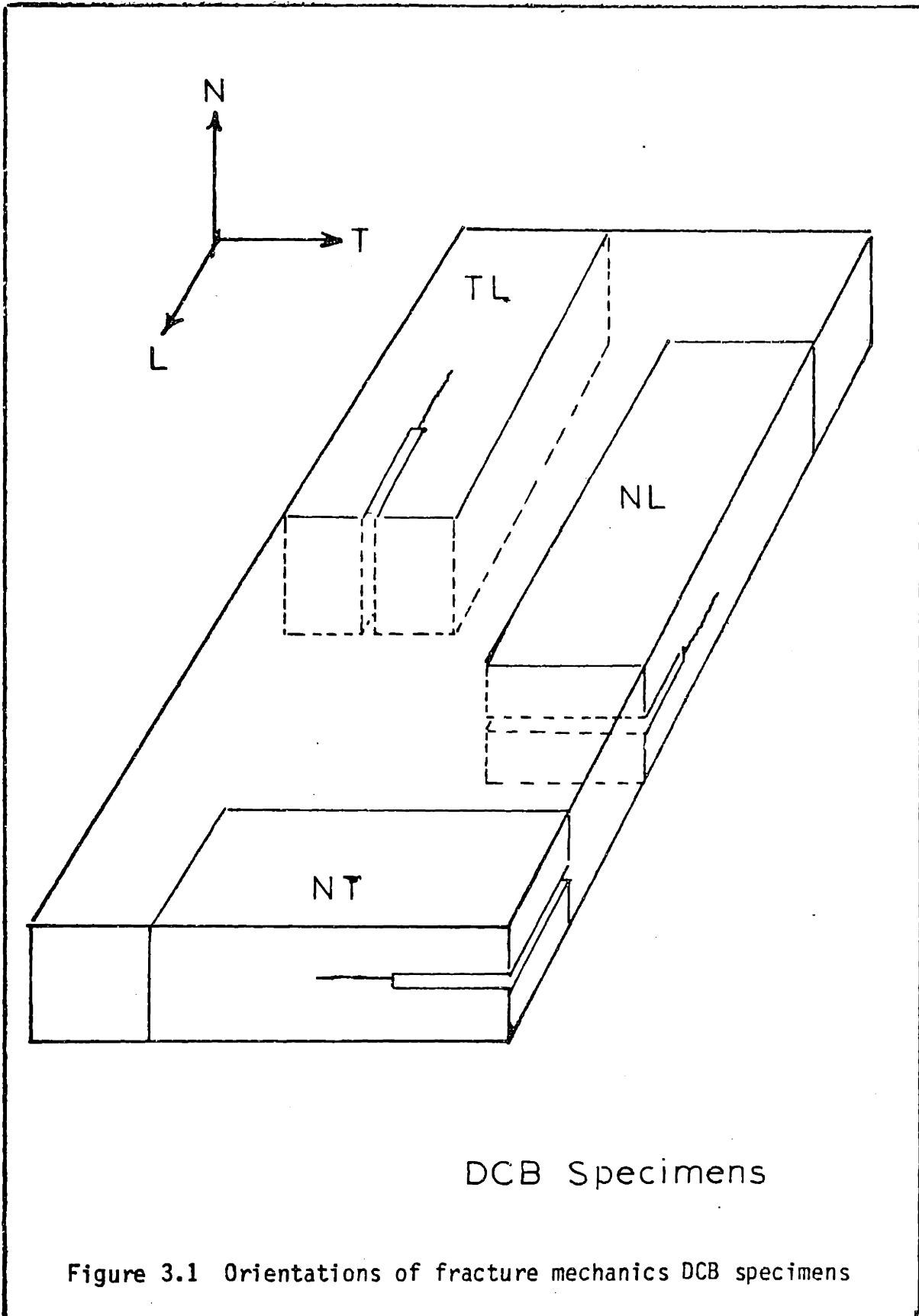
3. PLAN OF WORK

The present study was undertaken to determine the kinetics of iodine-induced crack growth in Zircaloy, using a fracture mechanics approach. There are three main reasons for this study. First, with sufficiently good crack growth data in the low-growth rate regime it might be possible either graphically or analytically to extrapolate the data with some confidence to establish the threshold value for non-propagating cracks (K_{ISCC}). Secondly, kinetic data may provide a means of deducing some critical facts about the fundamentals of the iodine stress corrosion cracking process. Lastly, but not least, one is interested in knowing the rates at which I-SCC cracks can grow since this knowledge makes it possible to deduce the rates of crack initiation in smooth specimens.

Two types of specimens were used. The double-cantilever beam (DCB) specimen for plate materials experiments and pieces (3.0 in long) of Zircaloy tubing containing a fatigue crack for tube-pressurization tests. The DCB specimens are machined from different orientations in the plate as shown schematically in Figure 3.1. In the designation of orientation, the first letter gives the direction of specimen loading (i.e., crack opening) while the second letter indicates the direction of crack growth.

The author is aware of only two other studies which involved a fracture mechanics approach to the kinetics of iodine-induced crack growth in unirradiated Zircaloy. These were conducted by Cox and Wood (18) and Videm and Lunde (35); they have been described in Section

2.7. Both approaches were oversimplified in the way that the experiments were conducted and how the analysis of the data was done. Videm and Lunde, for example, in their study with precracked tubes evaluate the crack growth as the crack extension divided by time, neglecting that the growth speed increases as the cracks become larger. On the other hand, in the work by Cox and Wood velocity vs. stress intensity factor curves for DCB specimens are constructed from a few points only.



4. DESCRIPTION OF MATERIALS

4.1 Plate Material

The plate products were fabricated by Teledyne Wah Chang Albany Corp. (TWCA). The ingot number for the Zircaloy-4 material (plate 9912-4A) was 397523Q and for the Zircaloy-2 material (plate 9908-3A) was 397598Q. Table 4.1 shows the chemical composition of these plates. The fabrication schedules are shown in Table 4.2.

The fabrication schedules were controlled in a way which resulted in two different initial textures. Plate 9912 texture represented that which results from standard commercial plate rolling procedure. Figure 4.1 shows the basal pole figure near the center for this material. The texture consists of one with basal planes parallel to the rolling plane and basal poles in the normal-transverse plane tilted approximately 40 degrees to the transverse direction from the normal direction. Plate 9908 is warm cross-rolled to give a normal (0°) texture. Figure 4.2 shows the (0002) pole figure near the center of the plate for this material. Pole figures were determined using the method of Schultz (36). Texture f-numbers for these materials are listed in Table 4.3.

4.2 Tubing Material

Stress-relieved, reactor-grade Zircaloy-2 tubing was obtained from two suppliers (suppliers A and B). The inside diameter, outside diameter, and wall thickness of both tubing types were nominally 10.9, 12.8, and .94 mm (0.429, 0.504, and 0.037 in.), respectively. The

grain sizes of both tubing types were ASTM No. 11.0 in the longitudinal direction and ASTM No. 11.5 in the transverse direction. The chemical compositions of the two tubings are shown in Table 4.4, and the basal pole figures are shown in Figures 4.3 and 4.4. Values of the Kearns texture parameter for the radial direction (f_r) are also shown in Figures 4.3 and 4.4.

4.3 Microstructure

Microstructure of the materials was examined by polarized light microscopy, with the color contrast between grains being heightened by a thin metal oxide layer applied by anodizing. In this case, a clean polished specimen is required.

The specimen is wet-grounded on 120, 180, 240, 320, 400, and 600 grit silicon carbide paper. Care is used to prevent surface smearing (low hand pressure and low wheel speed).

The specimen is then polished using a combination of mechanical and chemical action. This technique helps prevent smearing of the surface during the polishing steps. Standard polishing wheels are used but are protected by polyethylene sheet under the polishing cloths. Coarse polishing is done on a wheel with nylon on metcloth using a 3- μ m alumina slurry and an acid solution of 250-ml water, 22-ml nitric acid, and 3-ml hydrofluoric acid. The abrasive slurry is applied to the wheel before the acid solution. The wheel is allowed to spin a few seconds at high speed. The specimen is polished then, at a lower speed with a light to moderate hand pressure. The specimen

is rinsed with a squirt bottle of water as soon as it is lifted from the wheel to prevent staining. Polishing is repeated as required. The wheel is rinsed and recharged with abrasive and acid every few minutes.

A finer polish with Nalcoag 1050 is produced using the same procedure on microcloth. This procedure results in a very clean flat surface.

An anodizing solution consisting of 30-ml ethyl alcohol, 35-ml water, 5-ml phosphoric acid, 10-ml lactic acid, 20-ml glycerine, and 2-g citric acid is used; 20 V of direct current are applied for approximately 15 sec to produce a violet color (37). A stainless steel beaker is used as the cathode and a pointed tungsten wire makes a good probe which is contacted to the sample surface, so that the probe material will be anodized in the solution and d-c current leakage will not occur through the probe (short circuit); otherwise, the sample surface will not anodize evenly.

The physical basis for the anodizing technique is the orientation dependence of the growth kinetics of oxides and other surface films, the film growth being slowest for basal surfaces and highest for prism surfaces; in other words there is an inverse correlation between atom packing density and the growth kinetics of anodized films as Green (38) has demonstrated for α -titanium. When the films are grown to an appropriate thickness range, the variation of film thickness associated with local variations of surface orientation result in different interference colors that can be observed through an

optical microscope.

Figure 4.5 illustrates the microstructure of the cold-worked stress-relieved material while Figure 4.6 shows the recrystallized microstructure. The grains of the cold-worked material are flattened with the smallest grain dimension measured through the plate thickness; for both plates that grain dimension is 4-6 μm . The dimensions in the longitudinal direction are in the range of 20-25 μm and in the transverse direction 12-15 μm . The grain size for the recrystallized plate is 8-10 μm .

Table 4.1
Chemical Composition of Zircaloy Plates

<u>Chief</u> <u>Alloying Elements</u>	<u>Plate</u>	
	9912 (Zircaloy-4)	9908 ((Zircaloy-2)
Sn	1.52w/o	1.51w/o
Fe	.20w/o	.14w/o
Cr	.11w/o	.10w/o
Ni	< 35 ppm	.05w/o
O	1160 ppm	1310 ppm

Table 4.2

Fabrication Schedules for Zircaloy Plates

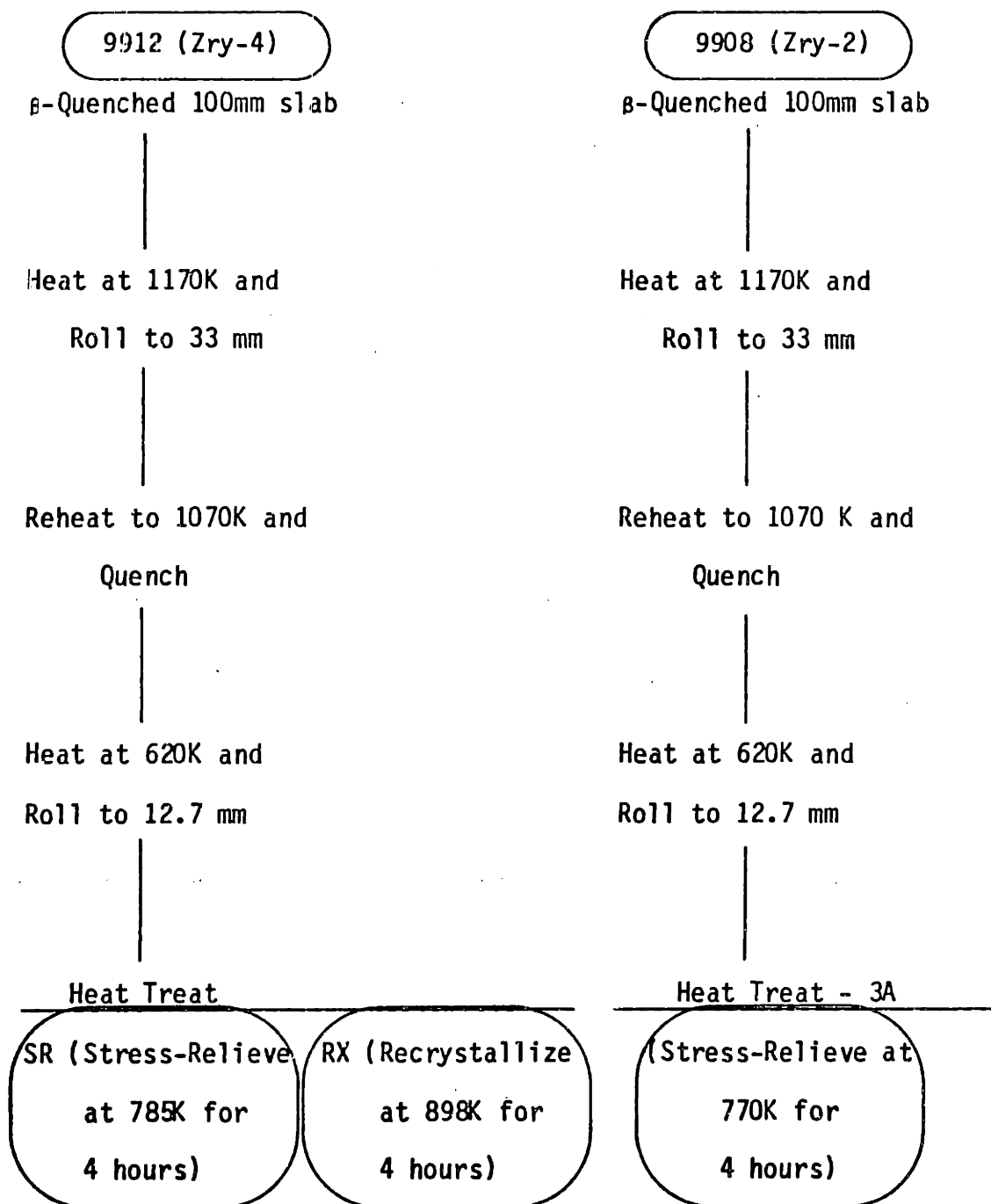


Table 4.3
Kearns' f-Number for Zircaloy Plates

f-number	9912		9908-3A
	SR	RX	
f_N	.56	.59	.70
f_T	.33	.32	.19
f_L	.09	.09	.09

Table 4.4
Chemical Analyses of Tubing from Suppliers A and B^a

<u>Element</u>	<u>Supplier A</u>	<u>Supplier B</u>
Sn (wt.-percent)	1.47	1.51
Fe (wt.-percent)	0.15	0.14
Cr (wt.-percent)	0.11	0.07
Ni (wt.-percent)	0.07	0.05
O	1170	1395

^aChemical analyses supplied by Exxon Nuclear Co., Inc., Richland, WA.

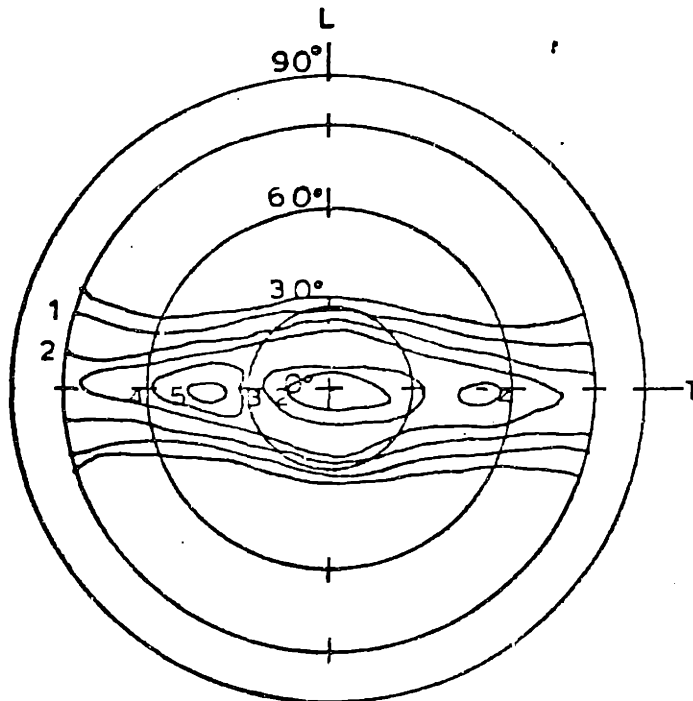


Figure 4.1 Basal pole figure for Zircaloy-4 plate 9912-SR at mid-thickness

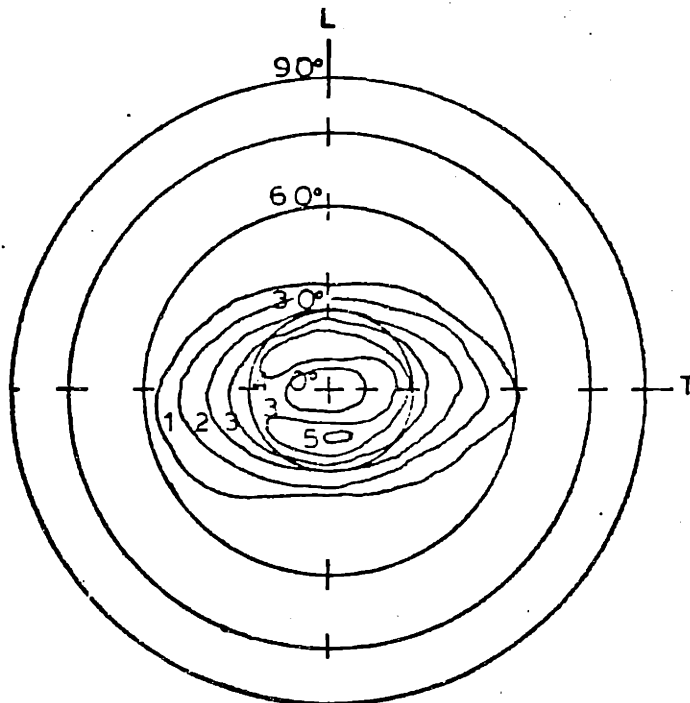


Figure 4.2 Basal pole figure for Zircaloy-2 plate 9908-3A at mid-thickness

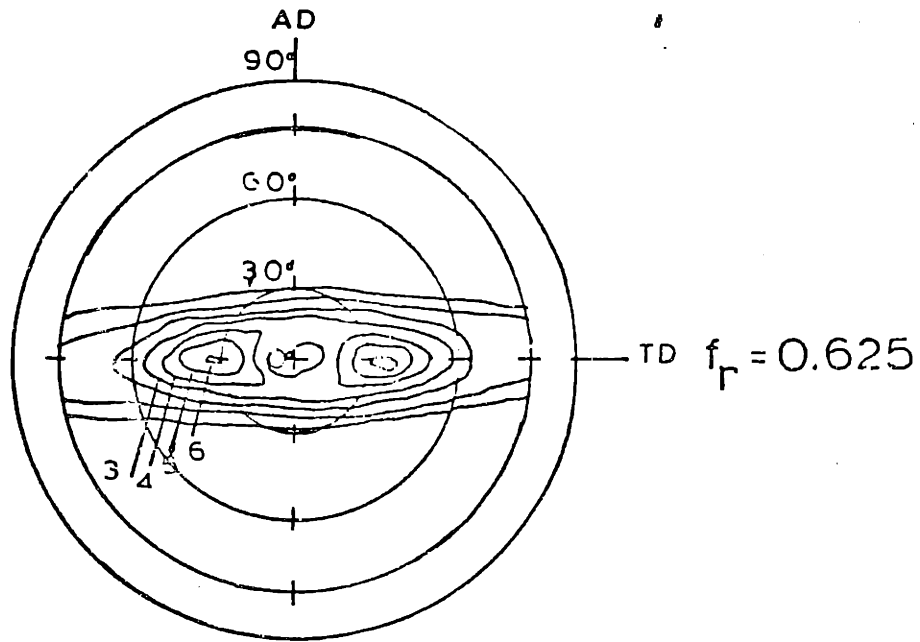


Figure 4.3 Basal pole figure for stress relieved Zircaloy-2 tube from supplier A at midwall

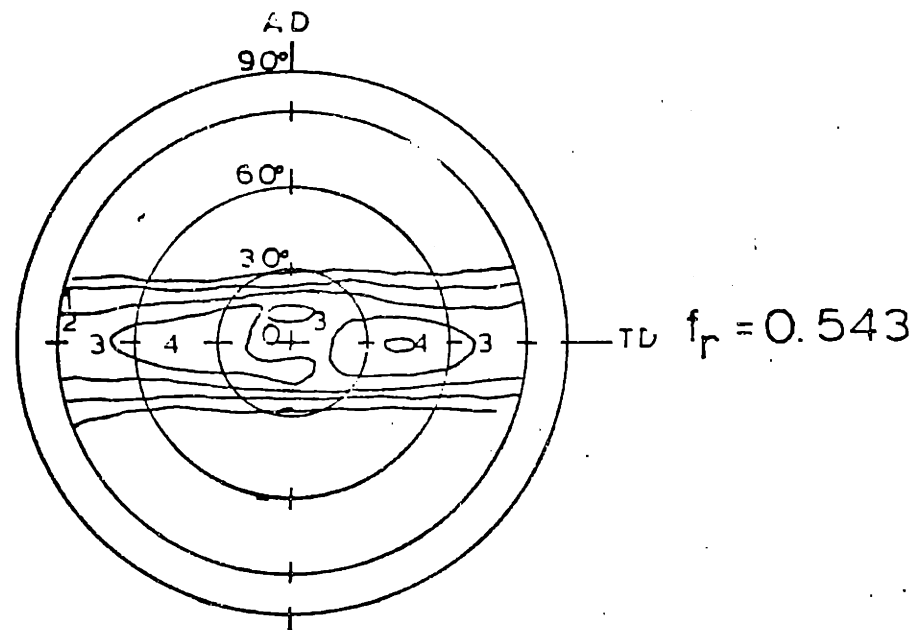


Figure 4.4 Basal pole figure for stress relieved Zircaloy-2 tube from supplier B at midwall

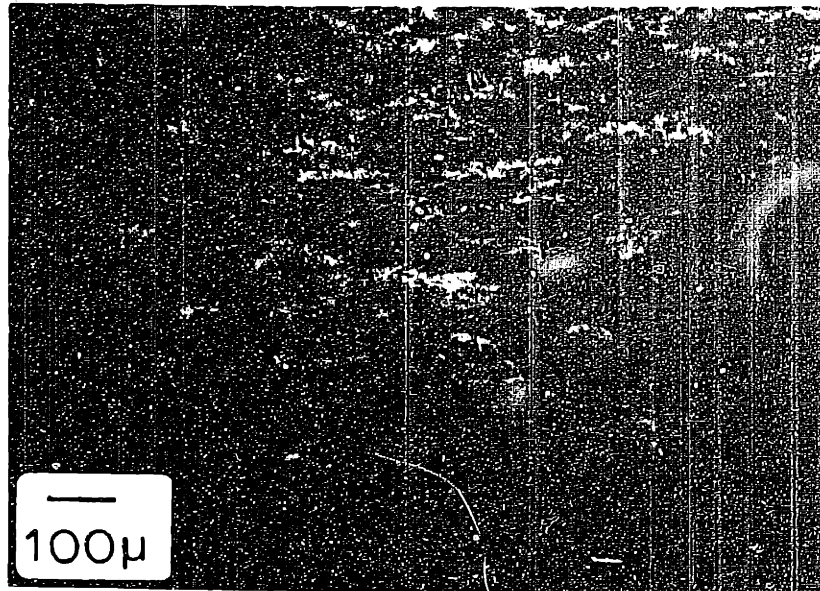


Figure 4.5 Microstructure of the Zircaloy-4 plate 9912-SR

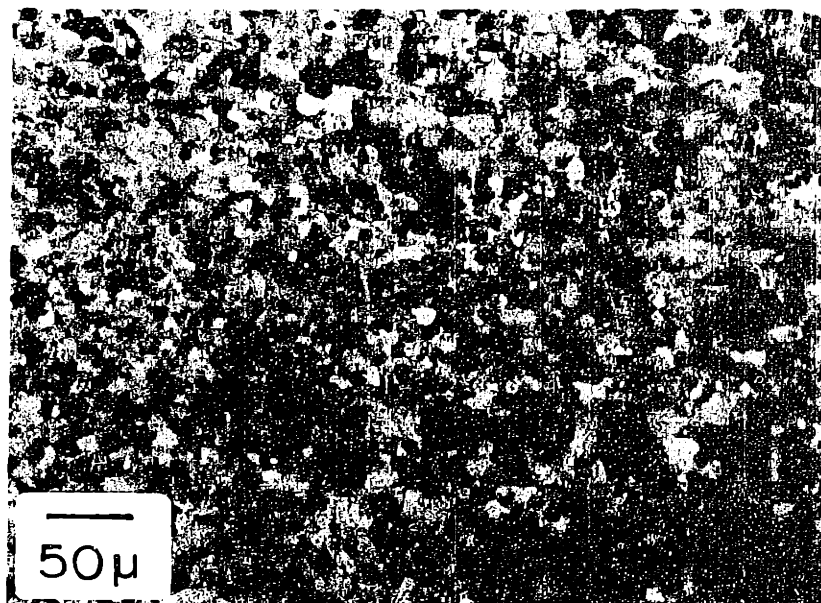
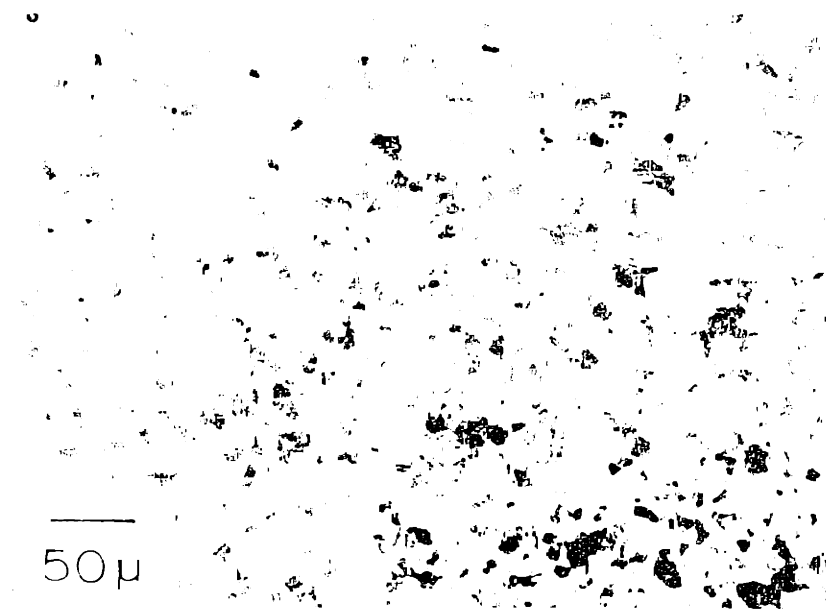
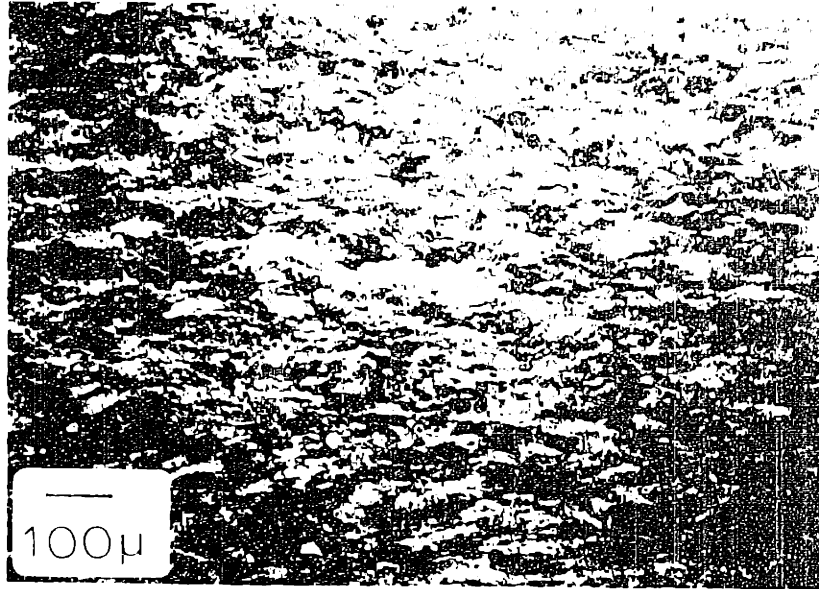


Figure 4.6 Microstructure of the Zircaloy-4 plate 9912-RX



5. EQUIPMENT AND TEST PROCEDURES

5.1 Crack Propagation Tests

5.1.1 Fracture Mechanics Specimen

The double-cantilever beam (DCB) specimen design was used in this program since it provides an economical and convenient method for measuring crack velocity as a function of stress intensity factor. The specimen is illustrated in Figure 5.1.

Stress intensity factor for this type of design can be calculated using a curve of compliance versus crack length and the equations:

$$G = (P^2/2b) \cdot dc/da \quad (5.1)$$

$$K_I = (G \cdot E)^{1/2} \quad (5.2)$$

where G is the strain energy release rate, P is the load, b is the specimen thickness, c is the specimen compliance (reciprocal stiffness) when the crack length a is measured from the load point (centerline of loading bolt), and E is the modulus of elasticity.

Alternatively, an approximate analytical expression for compliance as a function of crack length can be obtained using beam theory. However, it has been shown (39) that in addition to the bending and shear deflections that may be calculated from beam theory, some deflections also occur because of rotations at the assumed built-in end of the beam. By treating this contribution of compliance as an increase in crack length, the following expression for compliance was obtained (40):

$$c = (2.3EI) \cdot ((a + a_0)^3 + h^2 a) \quad (5.3)$$

where I is the moment of inertia of one of the arms, $I = bh^3/12$; a_0 is an empirical rotation correction equal to $0.6h$; and h is one-half the specimen height.

By differentiating Eq. (5.3) with respect to a , substituting into Eqs. (5.1) and (5.2) the following expression for K_I can be derived:

$$K_I = (2P/bh^2) \cdot (3h(a + a_0)^2 + h^3)^{1/2} \quad (5.4)$$

To perform a stress-corrosion test using this specimen, the stressed specimen is exposed to the corrosive environment, and the crack length a is measured on the side of the specimen as a function of time. The crack tip velocity is measured from the slopes of the crack length versus time curve. Stress intensities corresponding to each measured velocity can be calculated from Eq. (5.4) if the corresponding a and P are known. The crack length at which growth ceases (if this occurs) is then used to calculate K_{ISCC} . This procedure is illustrated schematically in Figure 5.2.

5.1.2 Environmental Control System

SCC growth tests were conducted at 25, 100, and 310°C in highly purified argon plus iodine gas environment. The gas purification system and test chamber illustrated in Figures 5.3 and 5.4 respectively, were able to deliver a constant partial pressure of iodine of minimal water vapor and metal iodide contents.

High purity argon (five 9's minimum) was passed through two columns that further purify the gas stream. The dierite and $\text{MgClO}_4\text{-P}_2\text{O}_5$ column remove residual water vapor and ascarite removes CO_2 . The gas is then passed through a column of iodine crystals (reagent grade, better than 99.8 percent) maintained at room temperature, so that it becomes saturated with iodine vapor. The I_2 plus Ar gas stream is then circulated through a molecular sieve column (Linde 4A) maintained at $150 \pm 5^\circ\text{C}$ to eliminate water vapor associated with the iodine crystals (and also to permit passage of the iodine). Next the gas enters in a glass bead condensing tower which is a volume filled with Pyrex balls to give a large surface area. This tower is maintained in most of the experiments at room temperature to give the desired partial pressure of iodine (41) ($40 \text{ Pa} = 0.3 \text{ Torr}$).

A significant amount of iodine was trapped by the molecular sieve, but the proportion that accumulated on the glass beads probably contained less than 1 ppm absorbed water vapor (42).

During test, the high purity iodine plus argon gas was continuously passed through the specimen test chamber at $150 \text{ cm}^3/\text{min}$ with a total pressure of 15 psi. Iodine was trapped from the exit gas with Linde 4A molecular sieve at room temperature.

The gas purification system was constructed with glass, thick-walled Teflon tubing, Teflon Swagelok fittings and high vacuum glass/viton/Teflon O-ring sealed valves. These materials are known to be inert to iodine attack.

The test chamber was made with glass and gold-plated stainless

steel to preclude volatile metal iodides from the test environment. The chamber has mechanical feed-through to permit the application of an external load to the specimen on a universal testing machine (Instron).

The test temperature was controlled by means of an ATS split furnace; this furnace has sufficient volume to accept the test chamber. The furnace controller was a Leeds and Northrop Electromax III SCR type control coupled to a Leeds and Northrop zero voltage power package. Specimen temperature measurement is achieved by a chromel-alumel thermocouple.

Prior to tensile loading, the specimen was held at the test temperature for about one hour while the iodine plus argon gas stream circulated. In the meantime, exposed glass parts were warmed with the flame of a propane torch.

5.1.3 DCB-Specimen Preparation

The DCB-specimens are pre-notched with a 0.3 mm wire saw to a depth of 0.5-1.0 mm. The surface for observation of the propagating crack is polished in the same way as for metallography. Then, the specimens are fatigue pre-cracked in a MITS closed-loop hydraulic machine. The maximum stress intensity range during pre-cracking is about 10 ksi in with $R = 0.1$ (see also Appendix C).

The tensile loading is applied to the specimen by means of Zircaloy pull-rods. The specimen is loaded to an initial displacement and the crack growth is monitored optically through a viewing port in

the furnace by a traveling telescope. The load level and the crack length are noted as the crack grows.

5.2 Tube Pressurization Tests

5.2.1 Fatigue Pre-Cracking of Tubing

The method developed by Lemaignan et al. (43) was used for cracking Zircaloy-2 cladding tubes. The principle of the method is to compress the tube between two diametrically opposite generators using the device shown in Figure 5.5.

The jig is mounted in a fatigue machine (MTS). The upper plate is made of stainless steel and the curved surface in the bottom plate has a diameter slightly larger (1.15x) than the outside diameter of the tube to be precracked. This last requirement is to avoid the formation of two diametrically opposite cracks.

The fatigue machine is set in strain control. Under the applied load, the tube becomes oval. The maximum traction stresses are induced in the inside surface, right below the point of contact. The variation in the load and therefore in the stress with time makes it possible to introduce a fatigue crack in the upper inside surface of the tube since the deformation is assymmetric.

The transmission of a ponctual compressive load to the tube O.D. could lead to a very sharp stress distribution and to irregular cracking. Therefore a steel plate is placed between the load application point and the tube to spread the compressive loading over a region of the upper generator of the tube. The length of the zone

of contact, therefore the size of the crack, varies with the respective stiffnesses of the plate and the tube.

During test, the development of a crack leads to a decrease of the stiffness of the tube. Then, in monitoring the change in the compliance of the system (i.e., the ratio between the applied load and the resultant deformation), it is possible to follow the crack evolution.

For a given initial constant displacement, crack advance leads to a reduction in the load; therefore, after a certain amount of propagation the crack will be arrested. If the machine were run in load control as in the method presented by Petterson (44) there would be a chance of introducing plastic deformation in the tube after the cracking.

The reduction in load during test is monitored by an oscilloscope. The initial displacement is chosen to induce maximum traction stresses correspondent to a few thousand cycles in fatigue life as it is given by the S-N curves (45).

A typical crack is shown in Figure 5.6. The ratio length vs depth of the crack is a function of the thickness of the upper plate.

5.2.2 Closed-End Tube Pressurization Test Procedures

After fatigue pre-cracking, 75 mm (3.0 in) long test tubing specimens from both suppliers were tested in the as-received condition. Before testing the specimens were cleaned in acetone and rinsed with methanol.

The tube pressurization system (Figure 5.7) and experimental

procedures are described in detail elsewhere (46). Briefly, 5 mg of reagent grade iodine crystals (corresponding to $\sim 0.2 \text{ mg/cm}^2$) and a volume displacing Zircaloy mandrel were placed inside the test specimen. The tubing was connected to the pressurization system with stainless steel Swagelok fittings, and successively purged and backfilled with high purity argon several times to reduce the partial pressure of air and water vapor inside the specimen to very low levels.

The specimen was then heated to 320°C and internally pressurized with high-purity argon to the selected hoop stress. Stress is calculated from the formula:

$$\sigma = ((D_{id}^2 + D_{od}^2)/(D_{od}^2 - D_{id}^2)) \cdot p$$

where D_{id} and D_{od} are the inside and outside diameters, respectively, and p is the pressure inside the specimen.

Time-to-failure was taken as the time from initial pressurization to the sudden pressure decreases, which is monitored by an in-line pressure transducer.

5.2.3 Fractography

Observations of the fracture surface were made on some of the failed specimens. To obtain samples suitable for scanning electron microscope (SEM) examination, a ring section containing the SCC crack was cut from the failed specimen. The ring is cut axially so that the failure region is at the apex of one of the two half-rings. Then the

failure section is broken open at liquid nitrogen temperature by bending the half ring that contains the crack.

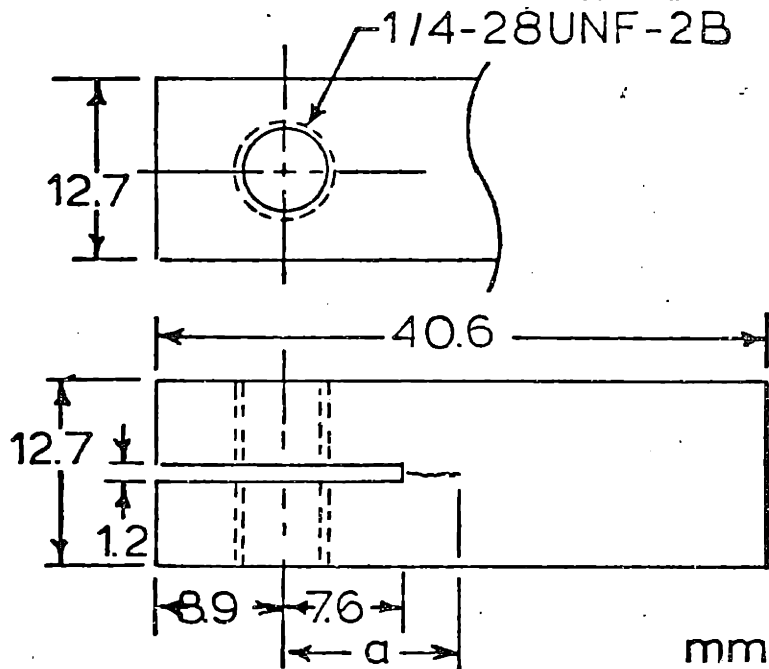


Figure 5.1 Schematic of fracture mechanics DCB specimens

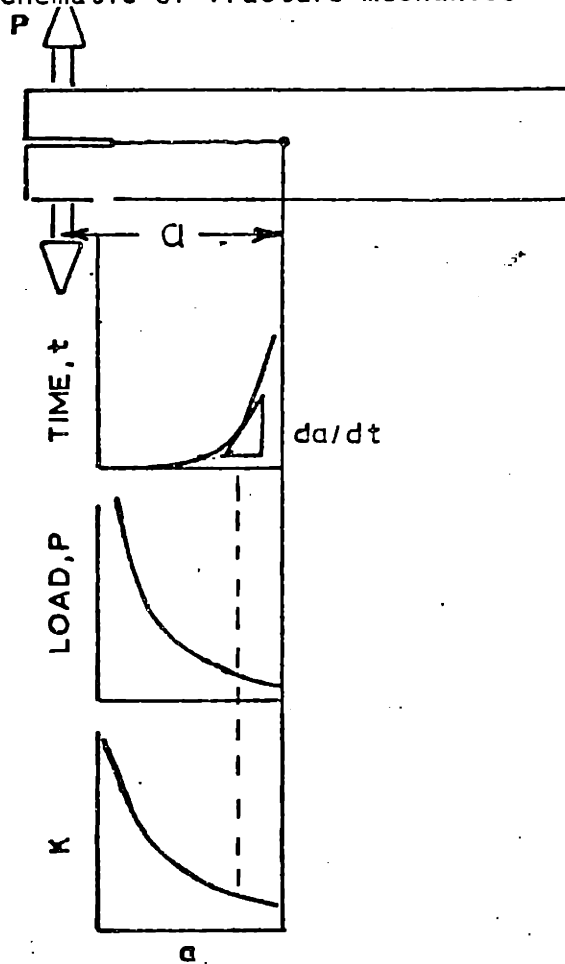


Figure 5.2 Schematic of the crack growth rate test. Effect of crack growth on load and stress intensity factor

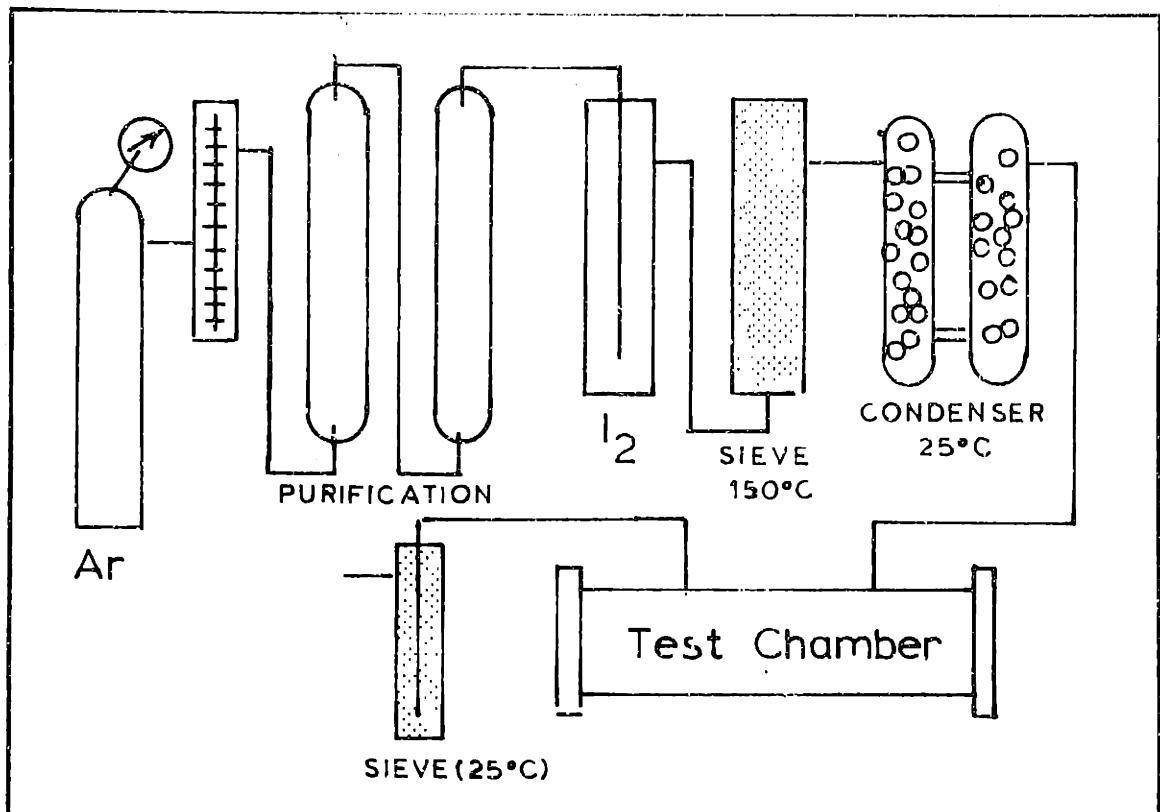


Figure 5.3 Diagram of the flowing gas (Ar + I_2) controlled atmosphere system

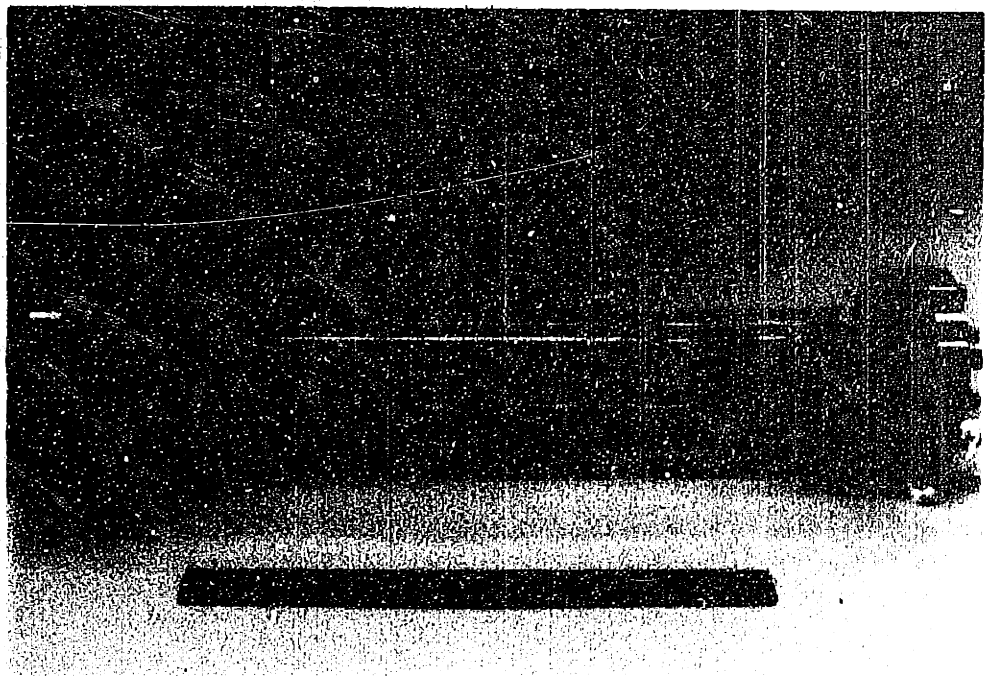


Figure 5.4 I-SCC growth test chamber

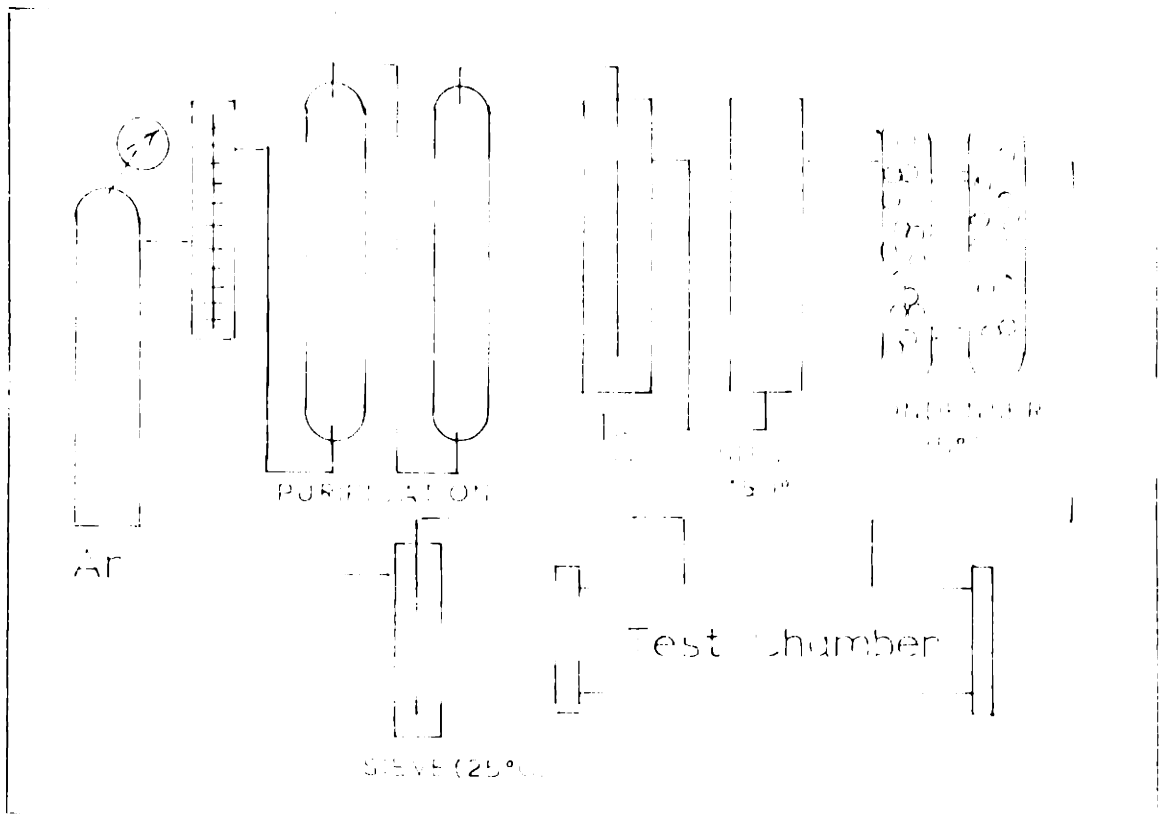


Figure 5.3 Diagram of the flowing gas (Ar + I₂) controlled atmosphere system

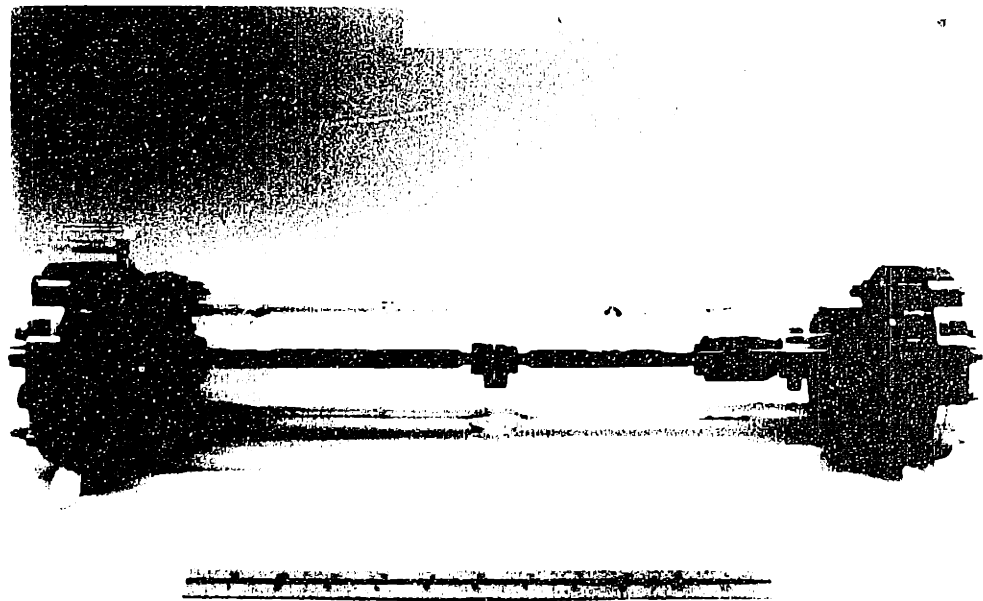




Figure 5.5 Device used for fatigue precracking of tubes.

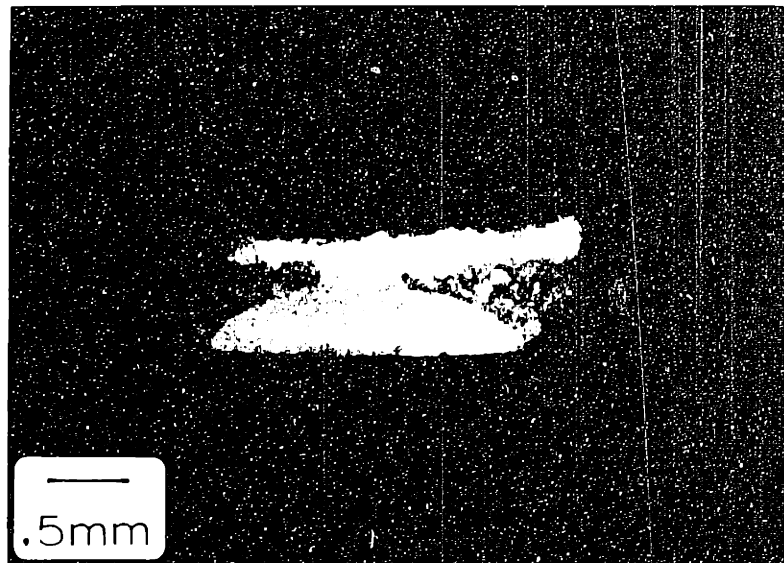


Figure 5.6 Optical macrograph of a fatigue precracked tube



Figure 5.5 Device used for fatigue precracking of tubes

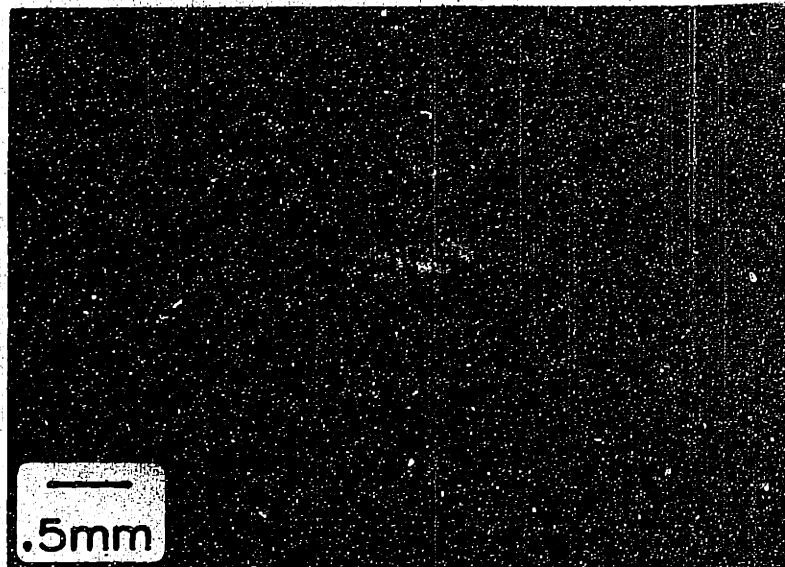


Figure 5.6 Optical macrograph of a fatigue precracked tube

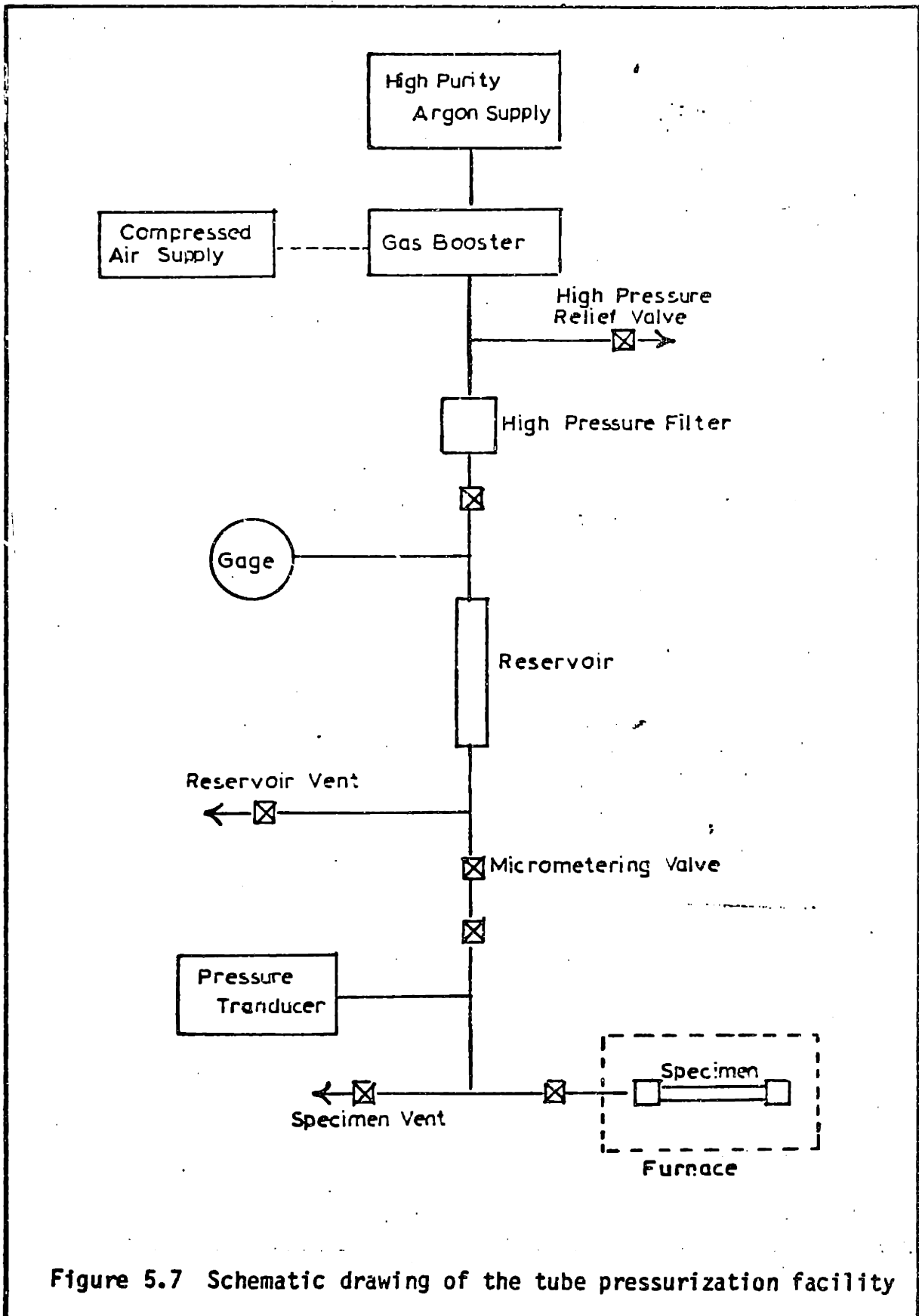


Figure 5.7 Schematic drawing of the tube pressurization facility

6. DATA REDUCTION AND ERROR ESTIMATION

6.1 Crack Growth Tests

In order to calculate the growth rate da/dt the crack length, a , versus time, t , data are reduced to fit a third degree polynomial by the least-squares technique using a computer program (47). The da/dt values are estimated from the derivative of the fitted curve.

6.1.1 Uncertainty in Crack Length (a)

The crack lengths were measured optically with a "home-built" traveling telescope. An estimation of an accuracy of ± 0.1 mm for this instrument was found.

Crack propagation was allowed to proceed a minimum of 1.0 mm between measurements to avoid the effect of the plastic zone of the previous measurement.

6.1.2 Uncertainty in K

The stress intensity factor is a function of the load (P), crack length (a), and materials parameters (b and h). The error in K is approximately the sum of the products of the errors in each parameter times the effect that parameter has on the final value of K .

6.1.2.1 Uncertainty in Load (P)

Load cell calibration, zeroing, and balancing procedures of the testing machine before experiments are the major sources of error in load. An estimation of ± 10 lbs for this error was determined.

The uncertainty in the specimen thickness, b , was found to be ± 0.5 mm and in the half-height, h , the uncertainty was ± 1.0 mm. Based on these values, an analysis of the uncertainty in the stress intensity factor, K , was carried out using the error propagation technique given by Bevington (48). An uncertainty of less than $2.0 \text{ MPa}\sqrt{\text{m}}$ was obtained.

6.1.3 Uncertainty in Temperature

In the crack propagation tests the uncertainty in temperature was $\pm 5^\circ\text{C}$.

7. RESULTS

7.1 Crack Propagation Tests

7.1.1 Crack Growth as a Function of Stress Intensity Factor

Iodine stress corrosion crack growth was observed in the plate material for all orientations tested and at all temperatures investigated (i.e., 310°, 25°, and 100°C).

Optical metallography and scanning electron microscopy were used to characterize the cracking process.

Figure 7.1 shows the general appearance of the cracks for specimens of the 9912 plate (40° texture) in the NT orientation, at three temperatures.

A detail of the crack tip region for both cold-worked stress-relieved, and recrystallized material tested at 310°C is presented in Figure 7.2.

The fracture surfaces of the specimens tested at 310°C are shown in Figures 7.3 and 7.4.

An unusual feature is evident in the TL-orientation specimen. The fracture surface is extremely rough with deep troughs extending into the specimen, perpendicular to the plane of macroscopic crack growth. These troughs are related to preferential cracking near the basal planes.

7.1.2 Shape of the da/dt vs. K Curves

In general, there is a threshold for stress corrosion cracking denoted K_{ISCC} , below which the rate of crack growth is very low (e.g., less than 10^{-10} m/sec). Above this level, increase in stress

intensity produces increases in the crack growth rate. A point may be reached where further increases in the stress intensity do not produce further increase in the crack growth rate. This can be understood in terms of a transport-controlled step in which the maximum potential for acceleration of this step by the crack tip stress field has been exceeded. At some value of K near K_{IC} , the process becomes mechanically dominated and crack advance is very rapid, with final failure occurring at K_{IC} . An SCC curve incorporating these ideas is shown in Figure 7.5.

The general appearance of da/dt vs K behavior at 310°C of the 9912-SR material for three different orientations is shown in Figure 7.6. Two successive regions of behavior are apparent. A low- K region (Regime I) exhibited strong K -dependent SCC growth, and a high- K region (Regime II) where the K -dependence of da/dt is weaker. Cox and Wood (18) have studied SCC crack growth in Zircaloy DCB specimens in iodine vapor at 300°C . The data they measured are plotted in the same figure for comparison.

Figure 7.7 shows the effect of the heat treatment on the crack growth behavior of specimens of 9912-plate, NL orientation. For the same stress intensity factor value, the crack growth rate was higher for the stress-relieved material. At low stress intensity values there was some evidence of intergranular cracking in the recrystallized material.

In the interval of stress intensity factor tested, from 17.2 to 12.3 ksi the crack growth rate for the specimen 9908-3A (0° of

texture), NT orientation tested at 310°C under 40 Pa of iodine was found to be independent of K and with a value of 2.38×10^{-4} cm/sec.

Figure 7.8 gives the crack growth rate as a function of stress intensity for specimens of 9912-SR Zircaloy plate (NT orientation) tested at 25°, 100°, and 310°C.

Assuming a da/dt value at $K = 25\text{Ksi}\sqrt{\text{in}}$ for the specimen tested at 100°C as a pseudo Regime II value and additionally assuming that the Regime II behavior was controlled by a single Arrhenius-type equation of the form

$$da/dt = A \cdot \exp(-Q/RT)$$

where A is the rate constant,

Q is the apparent activation energy per mole

R is the gas constant, and

T is the absolute temperature

the apparent activation energy, Q, may be calculated from the gradient of an Arrhenius plot ($\ln da/dt$ vs $1/T$) of the Regime II data. This is shown in Figure 7.9, where $Q = 2.9$ kcal/mole.

7.1.3 Fractography

Valuable information can be obtained by a close examination of the fracture surface. The bulk of the fracture surface caused by stress corrosion cracking in iodine vapor at elevated temperatures usually exhibits transgranular cleavage. The features which may be observed however, are very varied, particularly for different types of

specimens (i.e., different orientation, different heat treatment, etc.) and it may be advantageous to consider the fractographic features of each type of specimen separately.

Figure 7.10 illustrates two features observed in a specimen of the 9912-SR material, NT orientation tested at a lower iodine pressure (4 Pa): (a) transgranular cleavage in the SCC region and (b) "dimples" in the fast fracture region.

The influence of orientation of the specimen and of the texture of the material are illustrated in Figures 7.11 to 7.13 which show the fracture surfaces of specimens from plates 9912-SR and 9908-3A at 310°C under 40 Pa of iodine.

The fracture surface of the specimen of the 9912-SR material, TL orientation tested at 310°C under 40 Pa of iodine was heavily covered with a layer of some reaction product (Figure 7.14a). This occurred after the crack was propagated so that the deposit covers a normal SCC fracture surface after cleaning (Figure 7.14b).

The surface cleaning of the TL specimen was done by application of the replica stripping techniques followed by a chemical etching. In the replica stripping technique by successively stripping plastic acetate replicas from the fracture surface, corrosion and dirt particles can be lifted away. The mixture used for chemical etching was (49):

HCl (1.190 specific gravity)	3 ml
2-Butyne-1,4-diol (35 percent aqueous sol.)	4 ml
Deionized water	50 ml

This specimen was immersed in the inhibited HCl in a beaker at room temperature and the beaker was placed in an ultra-sonic cleaner for no more than 30 seconds.

Figures 7.15 to 7.17 show typical fractographic features of the surface of the recrystallized Zircaloy plate, NL orientation. "River patterns" generated when a cleavage crack passes from one grain to an adjacent grain with a slightly different orientation can be seen in Figures 7.15 and 7.16. The river patterns indicate the local direction of crack growth.

In the tests run at lower temperatures (i.e., 25°, and 100°C) little crack branching was observed at high values of K, but multiple nucleation at the initial crack starter did lead to overlapping cracks and ductile webs running parallel to the crack propagation direction as can be seen in Figure 7.18a. A scanning electron micrograph of the fracture surface of this region is shown in Figure 7.18b.

Scanning electron microscopy revealed a tendency for extensive "fluting" in the transgranular fractures in iodine at room temperature and also at 100°C as can be seen in Figures 7.19 and 7.20 respectively.

7.2 Tube Pressurization Tests

7.2.1 Time-to-Failure of Precracked Specimens

In keeping with the description of surface flaws in stressed components in fracture mechanics analysis, the tubing precracks can be classified as semi-elliptical planar cracks with an aspect ratio ($a/2c$). This type of flaw is illustrated in Figure 7.21.

Table 7.1 summarizes the results of the tube pressurization experiments with precracked tubing specimens.

For the present experiments, we did not find it necessary to determine the size of the fatigue cracks before the SCC exposure, as the different type of fractured zones could be easily distinguished either by optical microscopy or by scanning electron microscopy. Figure 7.22 illustrates this point.

7.2.2 Fractography

Fractographic appearance of the supplier B tubing after failure in I-SCC tube pressurization test (at 320°C in 0.2 mg/cm² of iodine) is shown in Figures 7.23 and 7.24. Some evidence of "fluted" region can be observed in Figure 7.23c (see arrow).

Two aspects of the fracture surface of a specimen of supplier A tubing are shown in Figure 7.25. The stress intensity factor at the surface for the semi-elliptical crack is between 10-20 percent lower than at the center of the crack.

Table 7.1

Results of the Tube Pressurization Experiments

Specimen	a_0/t	$a_0/2c_0$	σ_a (ksi)*	t_f (min)	t_f (min) smooth**
A2	.40	.26	42	293.9	4.10^3
A3	.60	.24	30	65.7	∞
B1	.37	.39	40	68	262
B2	.41	.22	37.5	179.4	400
B4	.55	.16	37.6	17.3	400

* σ_a is the applied stress.

**Time-to-failure in smooth specimen.

obs: Specimens A1 and B3 did not precrack in fatigue.

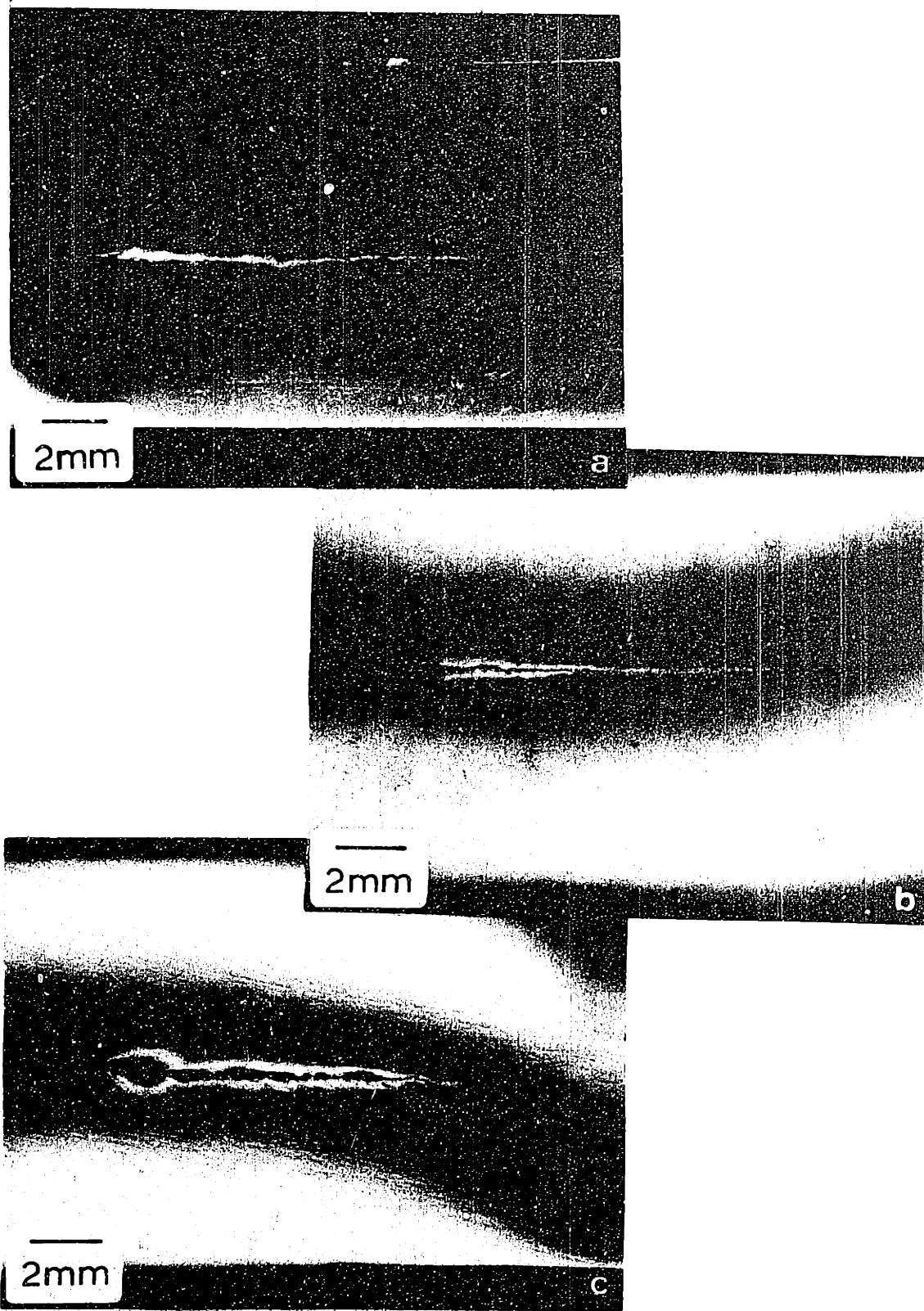


Figure 7.1 Profiles of I-SCC fracture of 9912-SR Zircaloy plate, NT orientation (a) 310°C, (b) 25°C, (c) 100°C

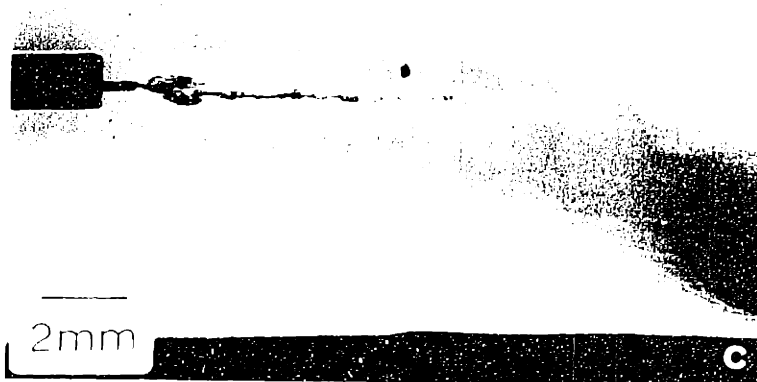
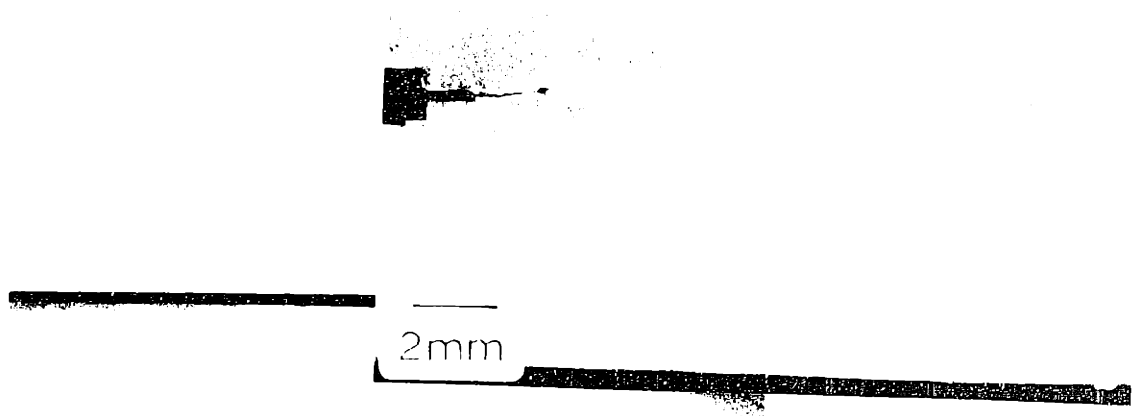
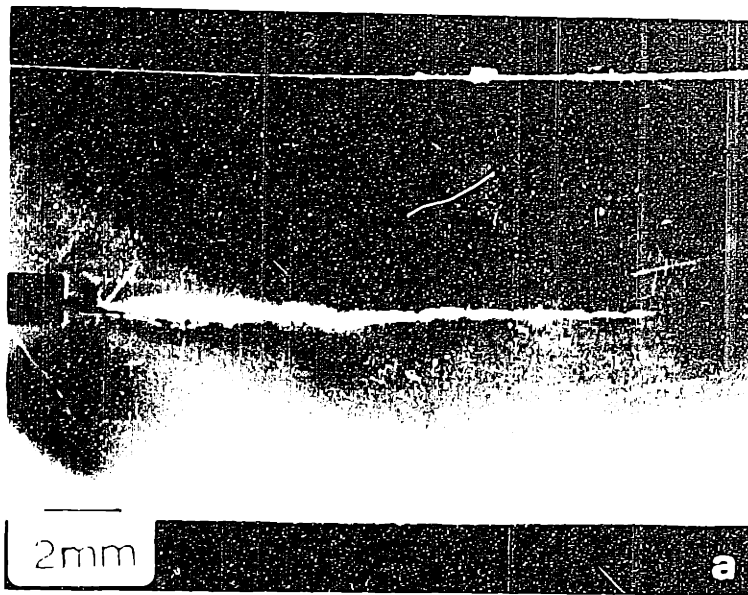


Figure 4.1 Profiles of 1-300 for lines of 99% purity at different orientations (a) 30° , (b) 75° , (c) 15° .

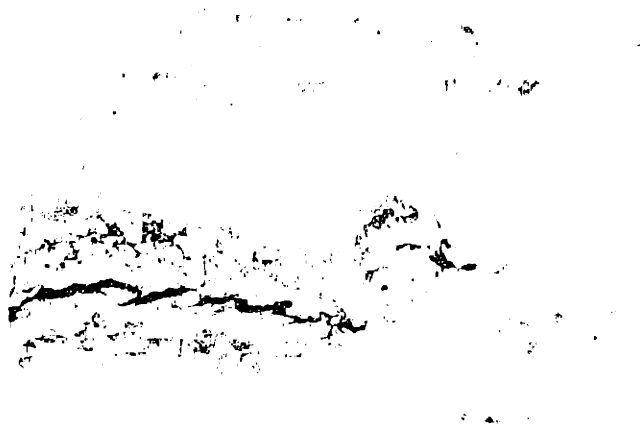
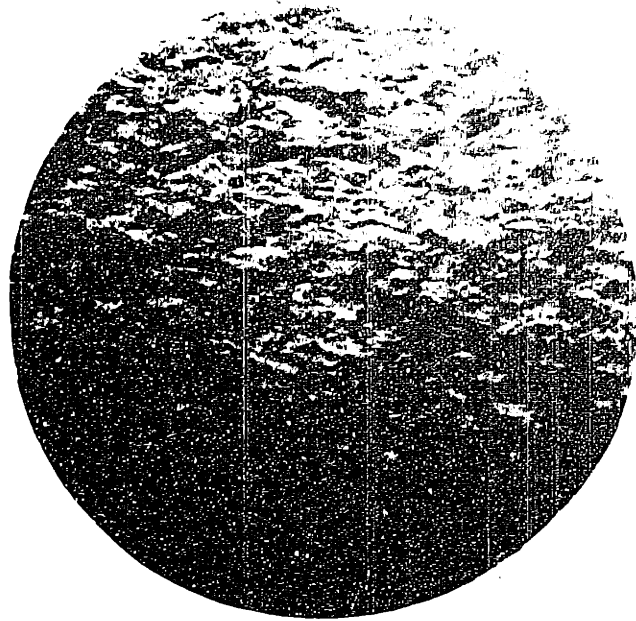


Figure 7.7 Artificially prepared surface of a metal specimen after stress relieving, and in crystalline structure at 1000°C.

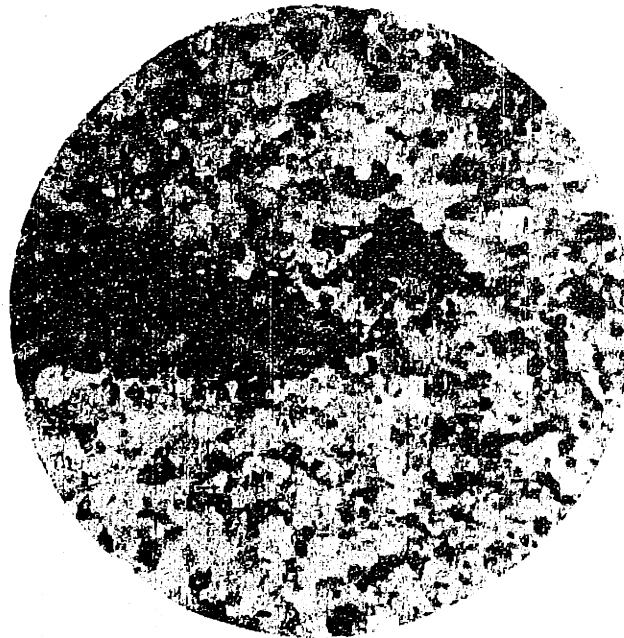
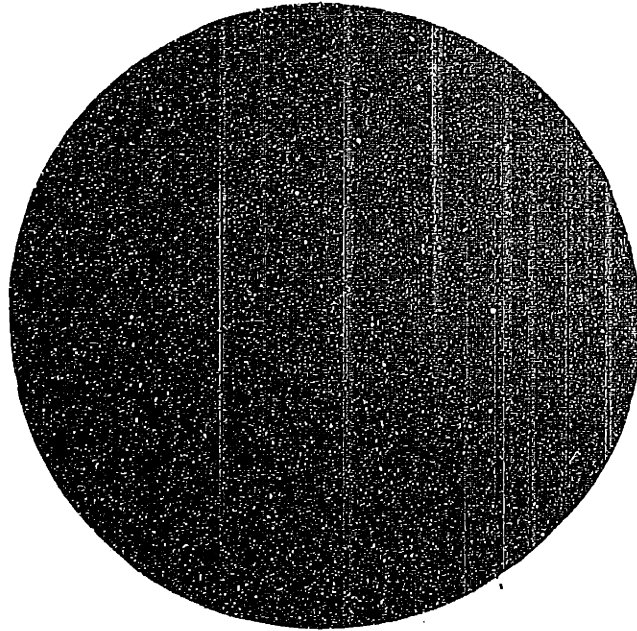


Figure 7.2 Optical micrographs of the crack-tip region in cold-worked stress relieved, and in recrystallized Zircaloy at 310°C

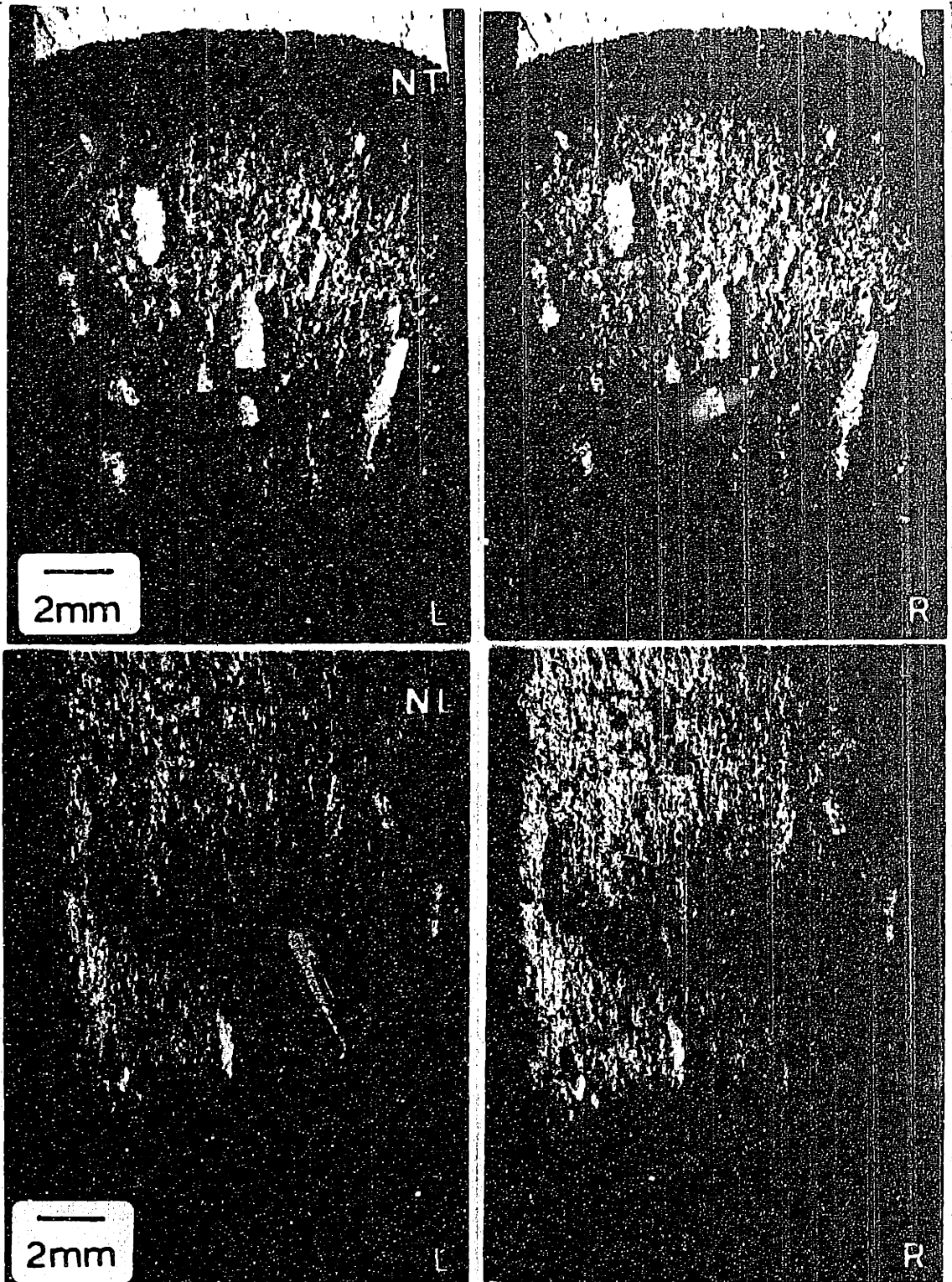
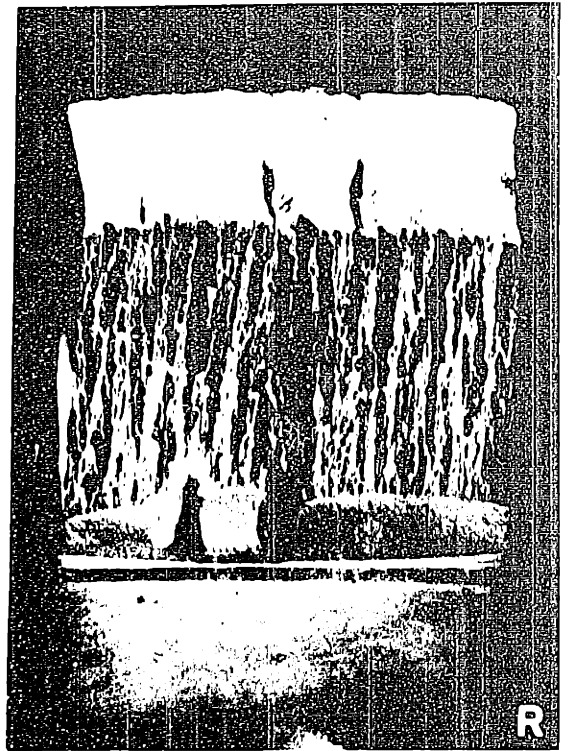
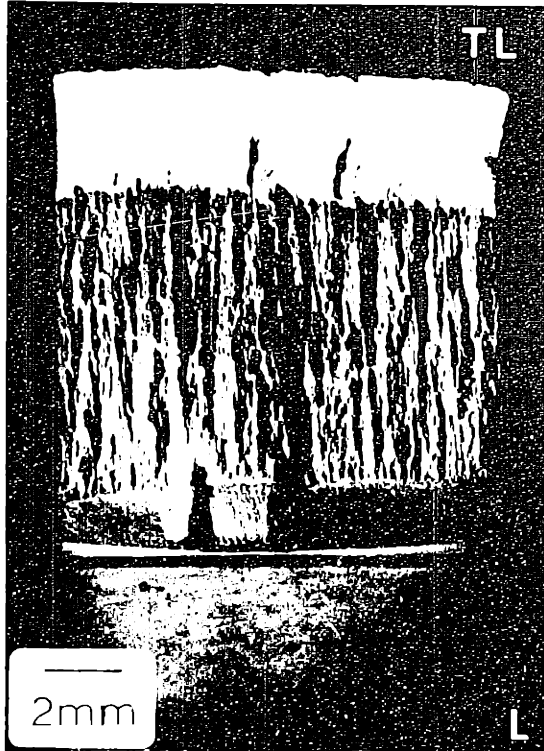


Figure 7.3 Fracture surface of the 9912-SR Zircaloy specimen tested at 310°C. NT and NL orientation. Stereo pair

INTENTIONAL DUPLICATE EXPOSURE



INTENTIONAL DUPLICATE EXPOSURE



INTENTIONAL DUPLICATE EXPOSURE

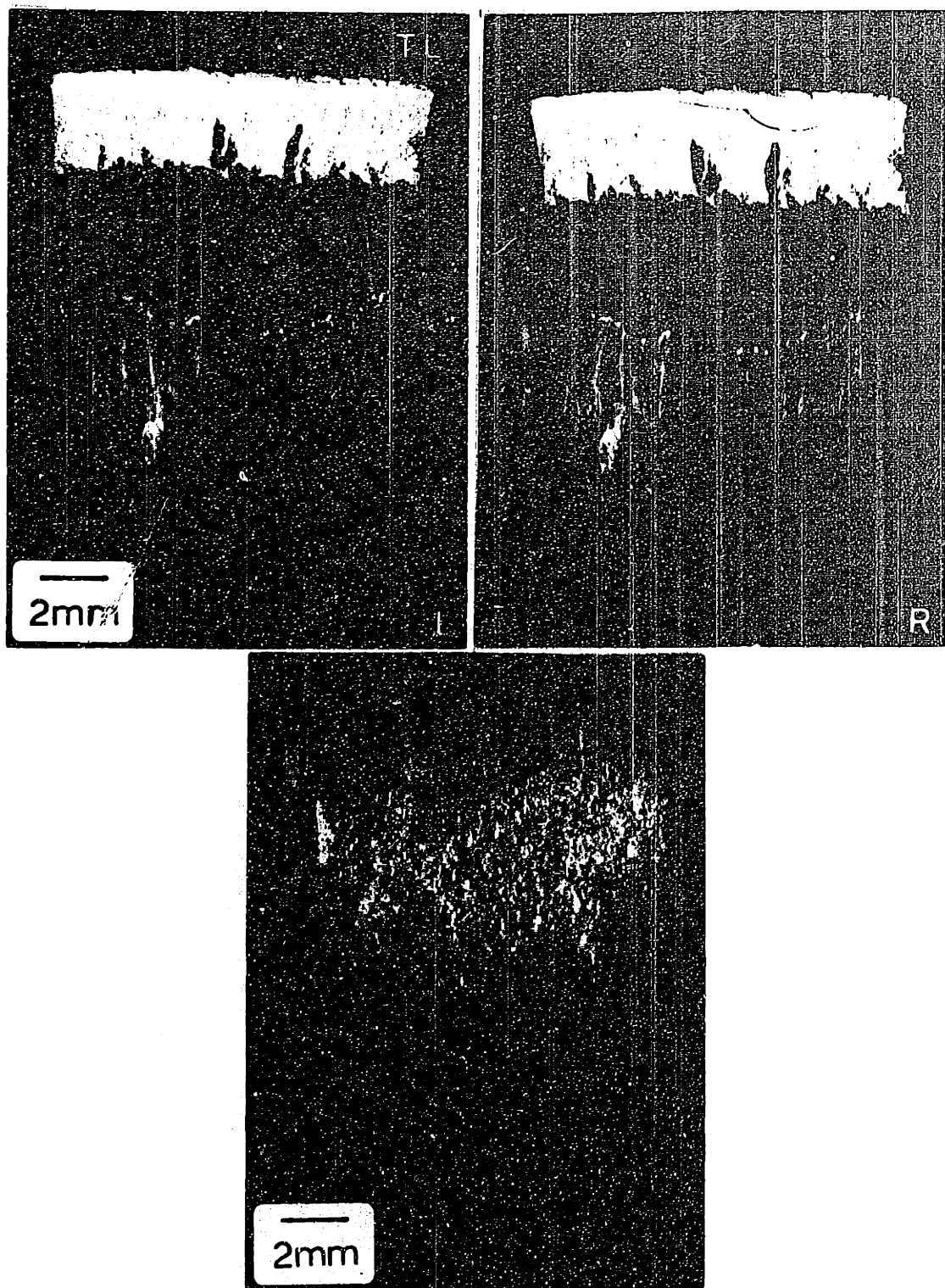
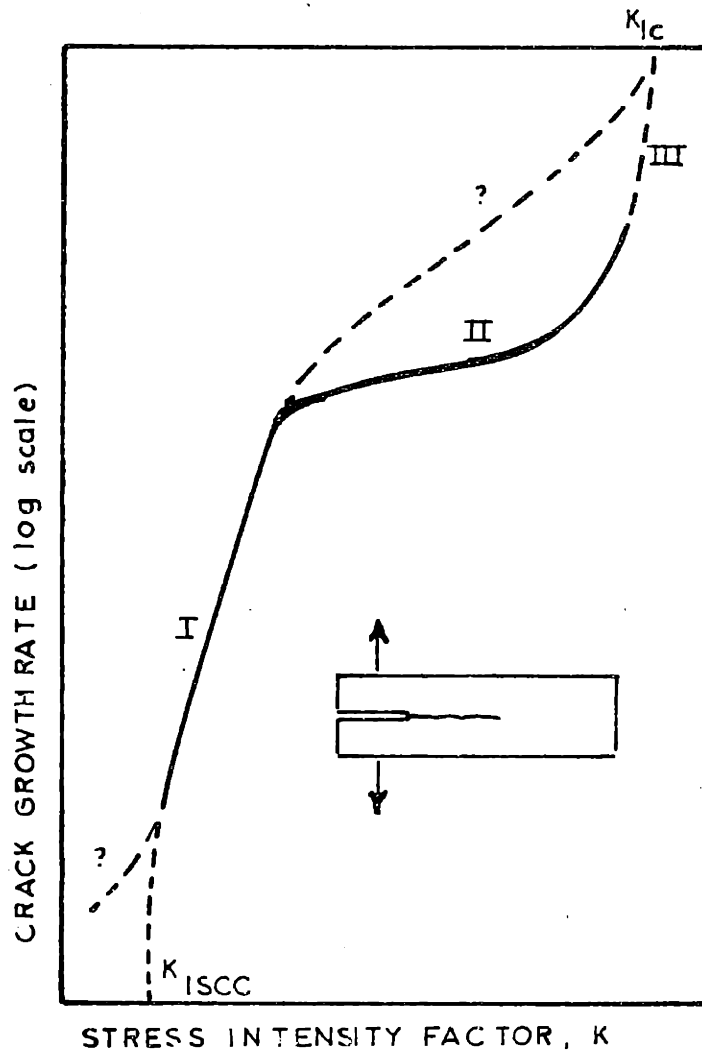


Figure 7.4 Fracture surface of (a) 9912-SR Zircaloy plate, TL orientation. Stereo pair. (b) 9908-3A Zircaloy plate. NT orientation. Both tested at 310 °C



7.5 da/dt vs K regimes schematic

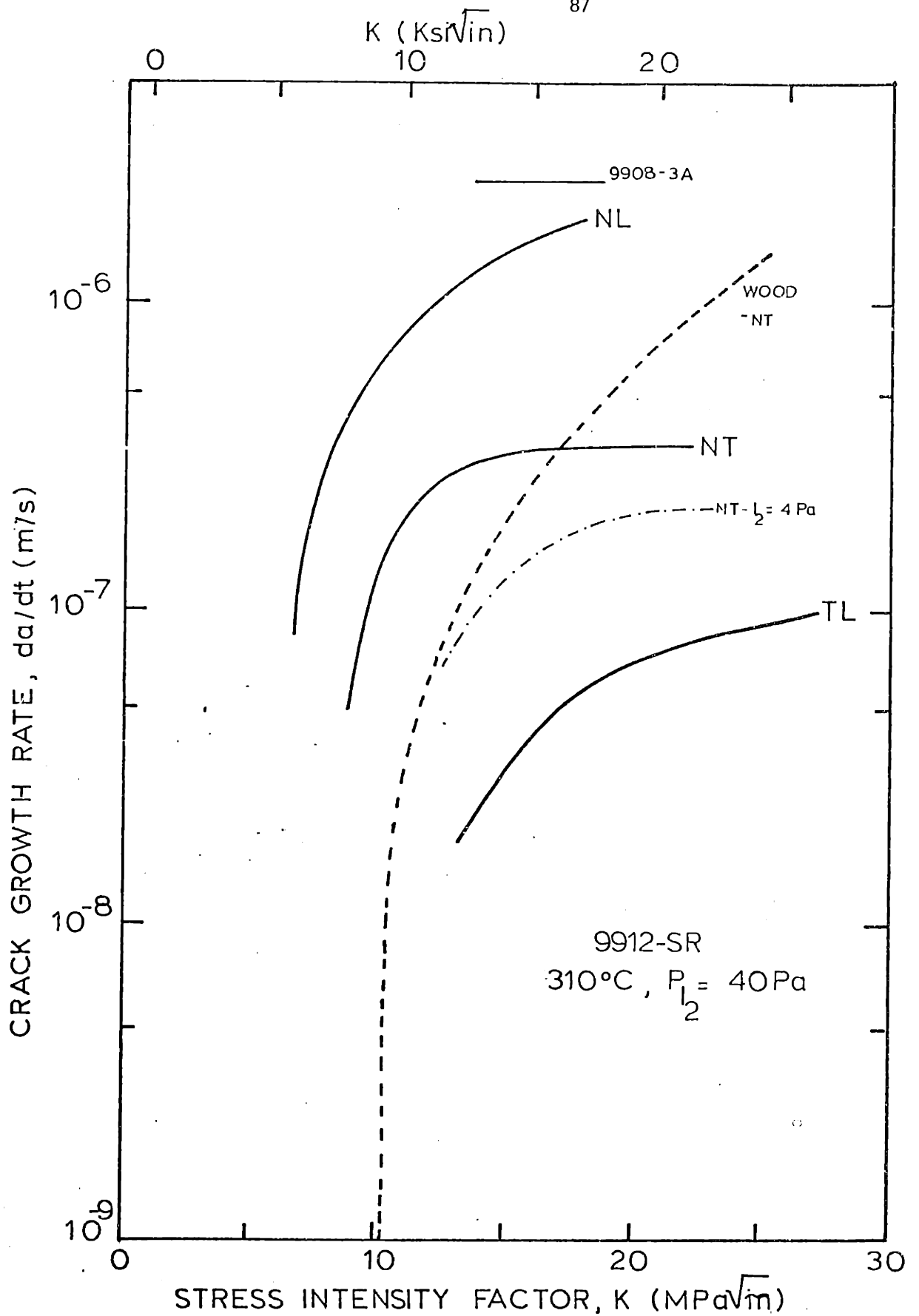


Figure 7.6 da/dt vs K behavior for specimens tested at 310°C

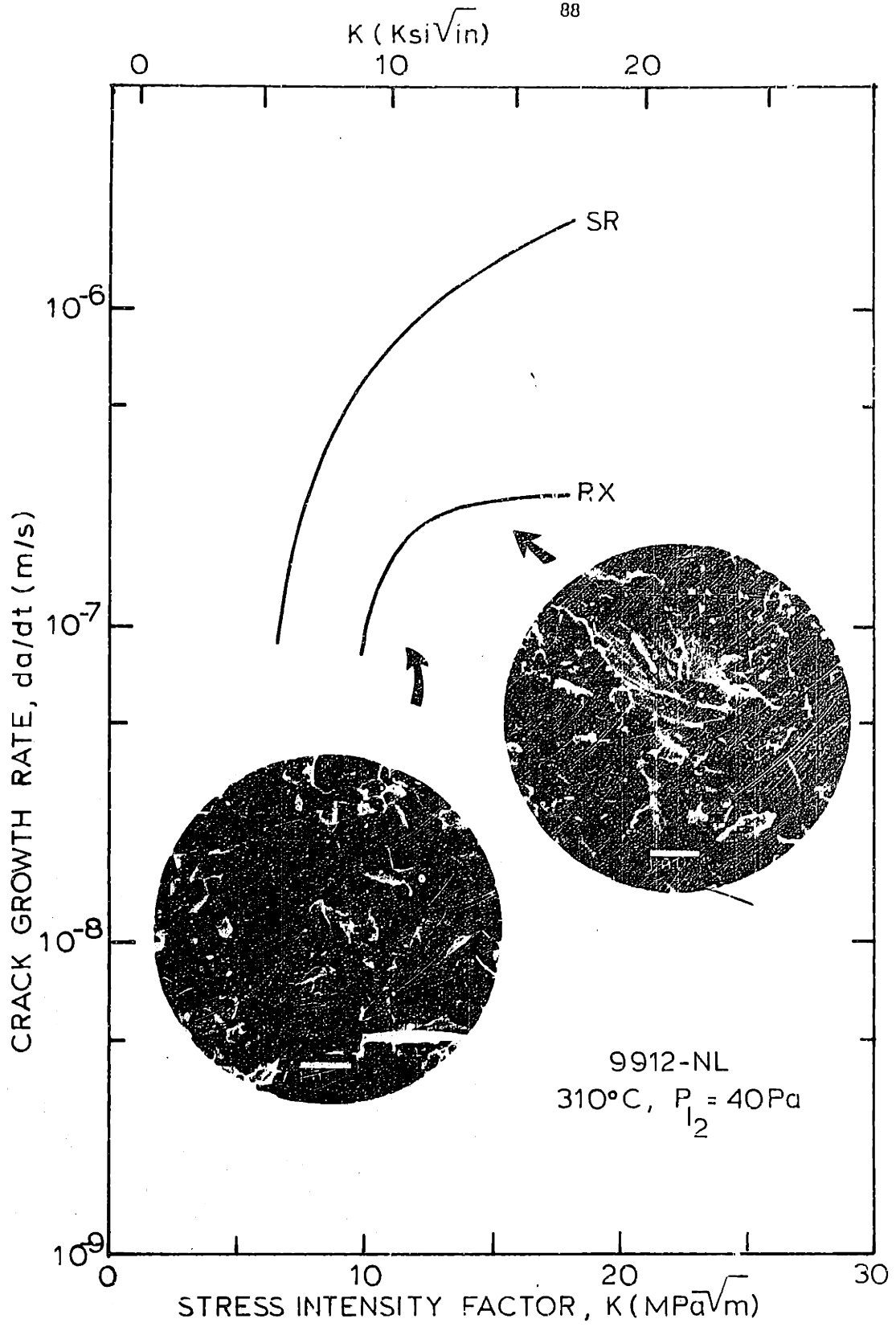


Figure 7.7 da/dt vs K curves for 9912 material in the NL orientation in two heat treated conditions: cold-worked stress relieved, and recrystallized

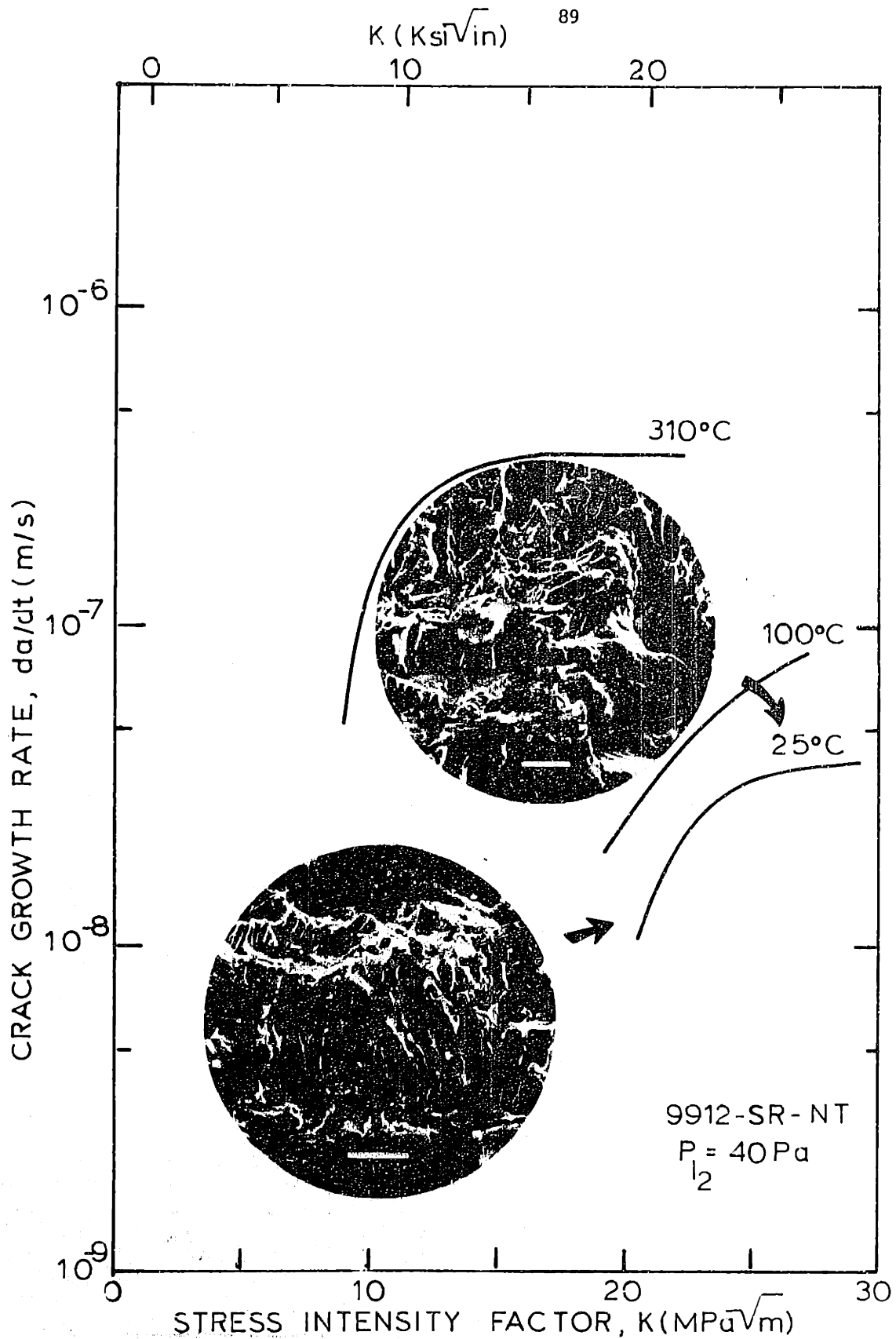


Figure 7.8 Effect of temperature on the da/dt vs K behavior for 9912-SR Zircaloy plate, NT orientation

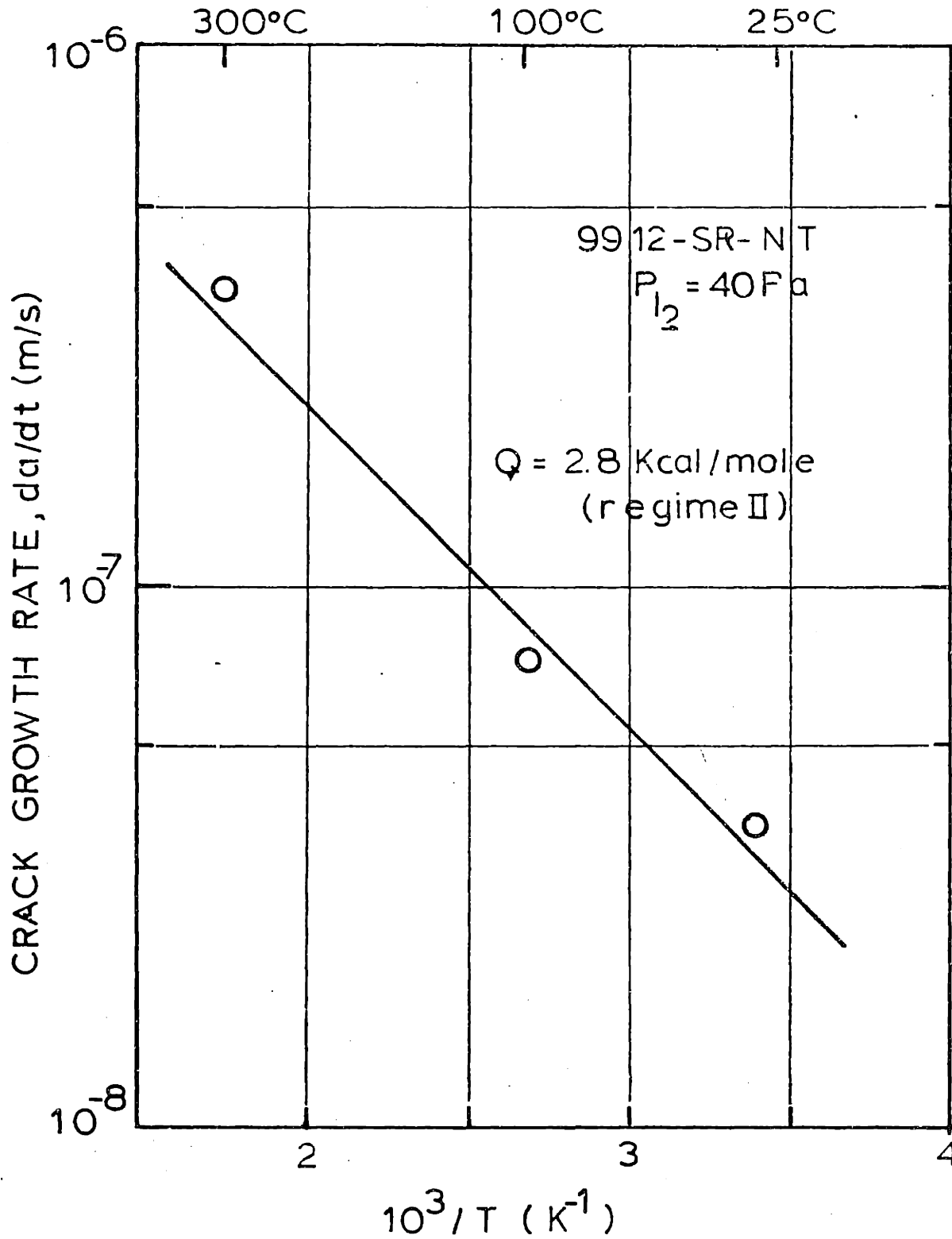
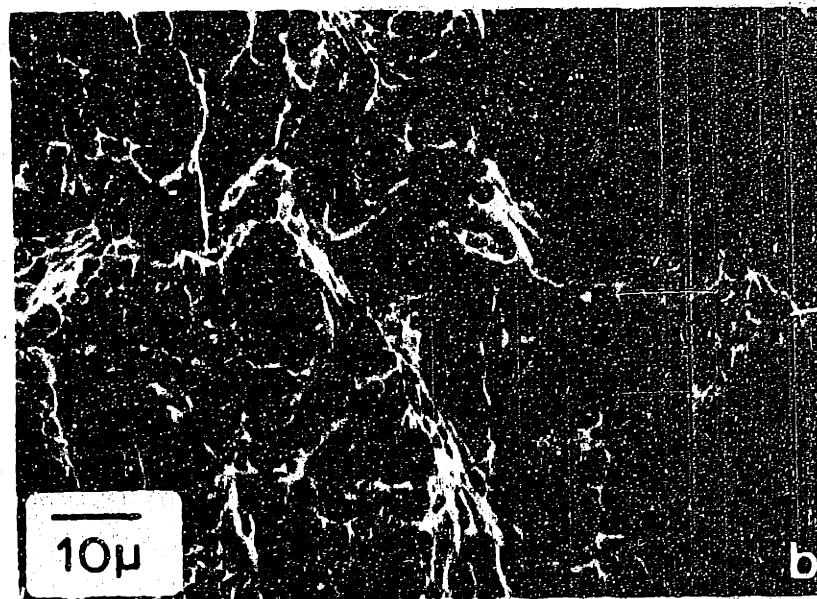
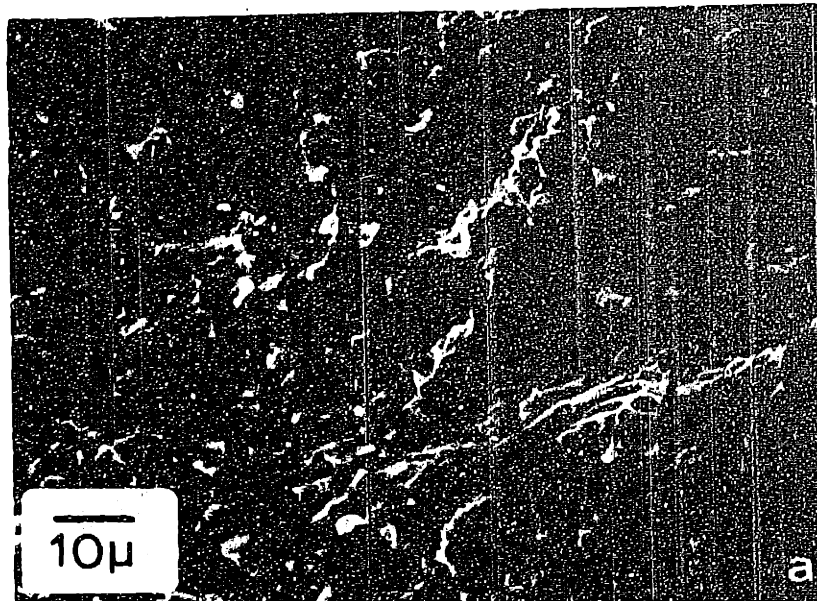
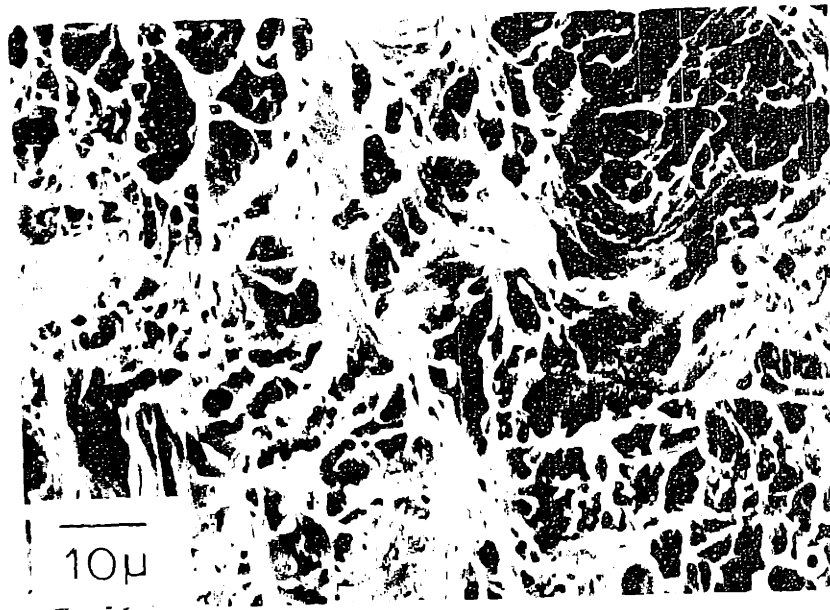
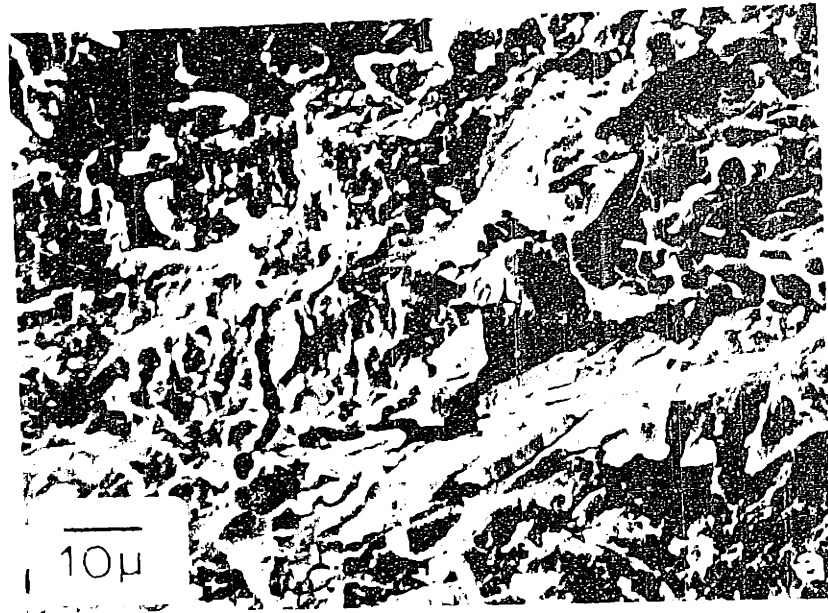


Figure 7.9 Arrhenius analysis of regime II-SCC growth behavior for 9912-SR Zircaloy, NT orientation

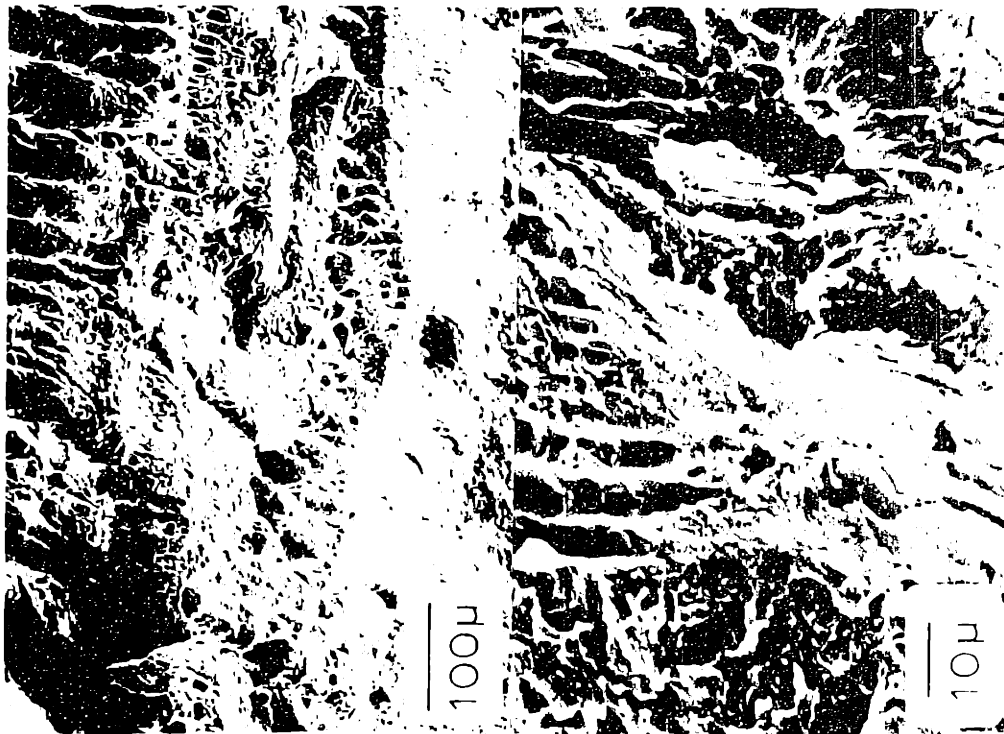
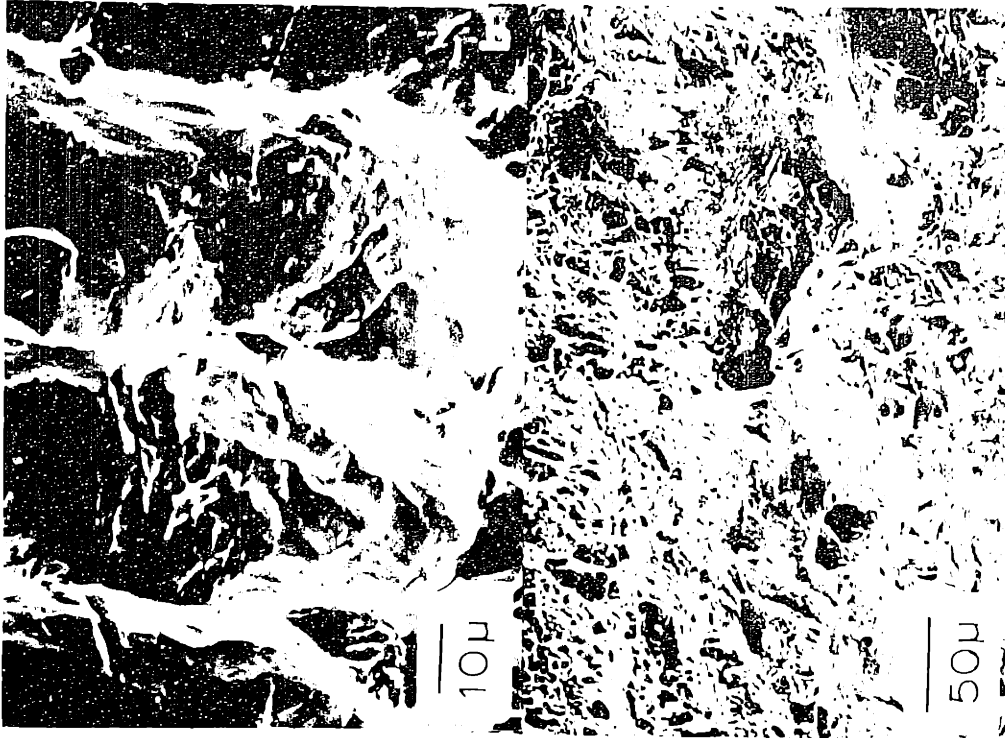


7.10 Scanning electron micrograph of the fracture surface of 9912-SR specimen. NT orientation tested under 4 Pa of Iodine. (a) Transgranular cleavage in the SCC region, (b) Dimples in the mechanical overload region.



7.10 Scanning electron micrograph of the fracture surface of 9912-SR specimen. Hl orientation tested under 4 Pa of Iodine. (a) Transgranular cleavage in the SCC region, (b) Dimples in the mechanical overload region.

INTENTIONAL DUPLICATE EXPOSURE



INTENTIONAL DUPLICATE EXPOSURE

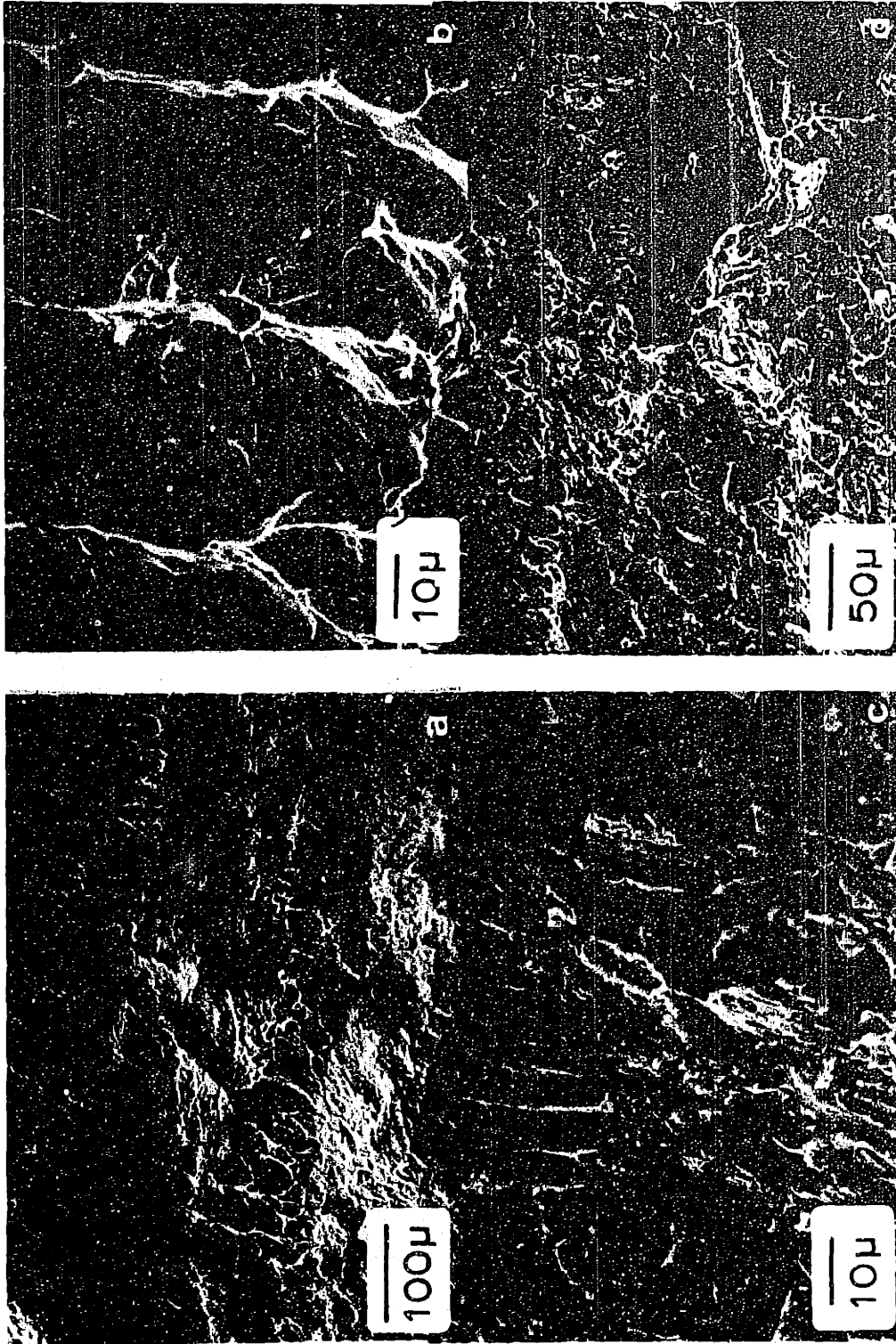


Figure 7.11 Scanning electron micrographs of the 9912-SR material, NI orientation tested under 40 Pa of iodine at 310°C. (a) Transition from the fatigue region to the SCC region (b) Detail showing fluting features (c) Detail of SCC region (d) Transition from SCC to ductile overload. The crack growth is from bottom to top

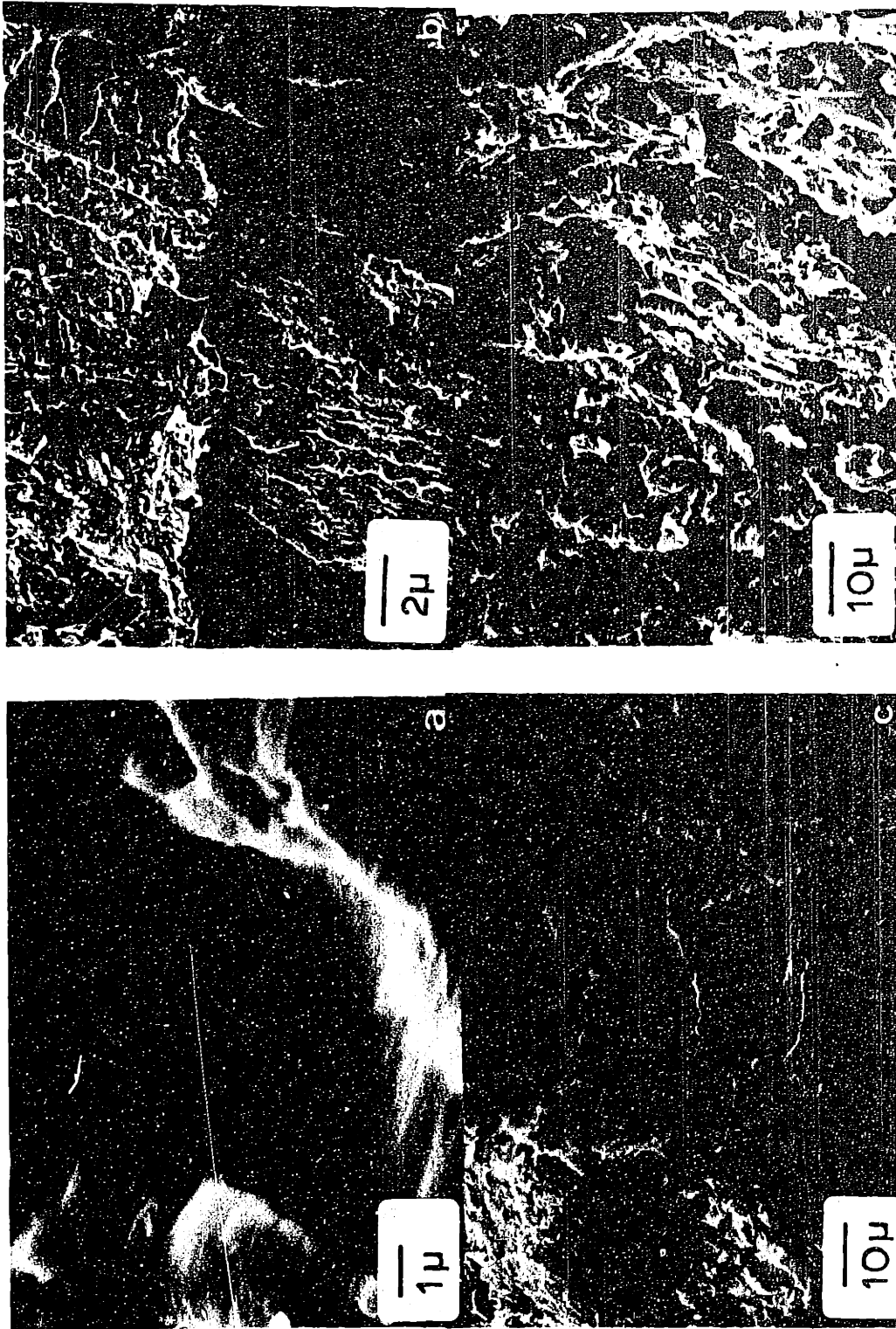
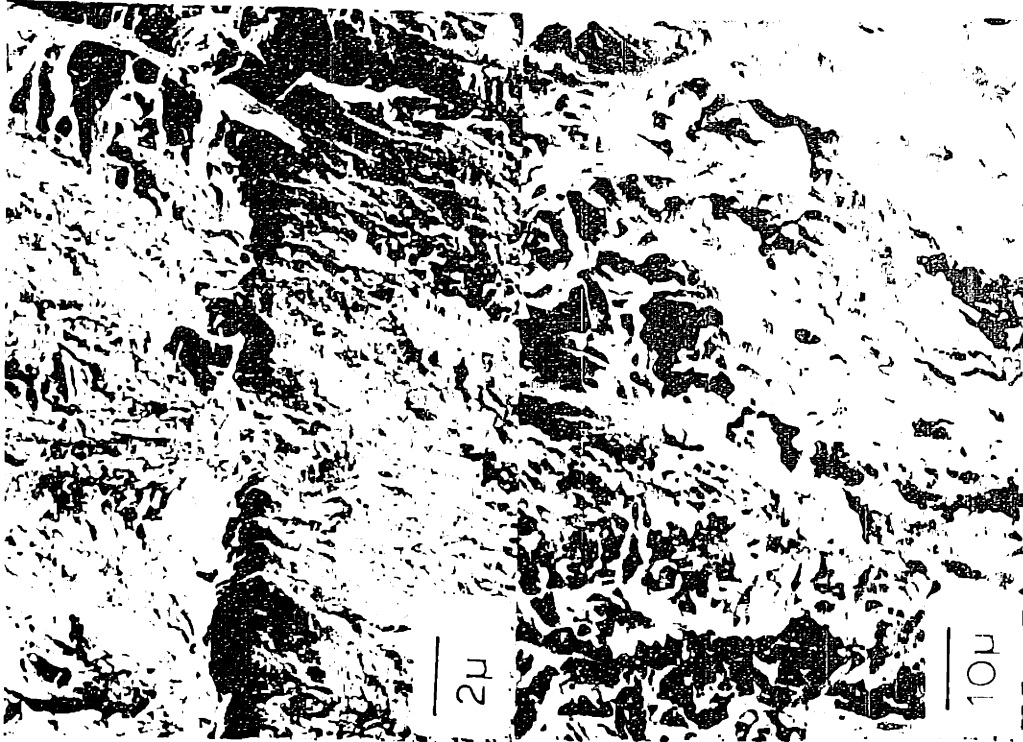


Figure 7.12 Scanning electron micrographs of the 9912-SR material, μL orientation tested under 40 Pa of iodine at 310°C (a) Detail of the precrack region showing fatigue striations (b) Transition from fatigue to SCC (c) Detail showing fluting (d) SCC region at low K value. Crack growth is from bottom to top



INTENTIONAL DUPLICATE EXPOSURE

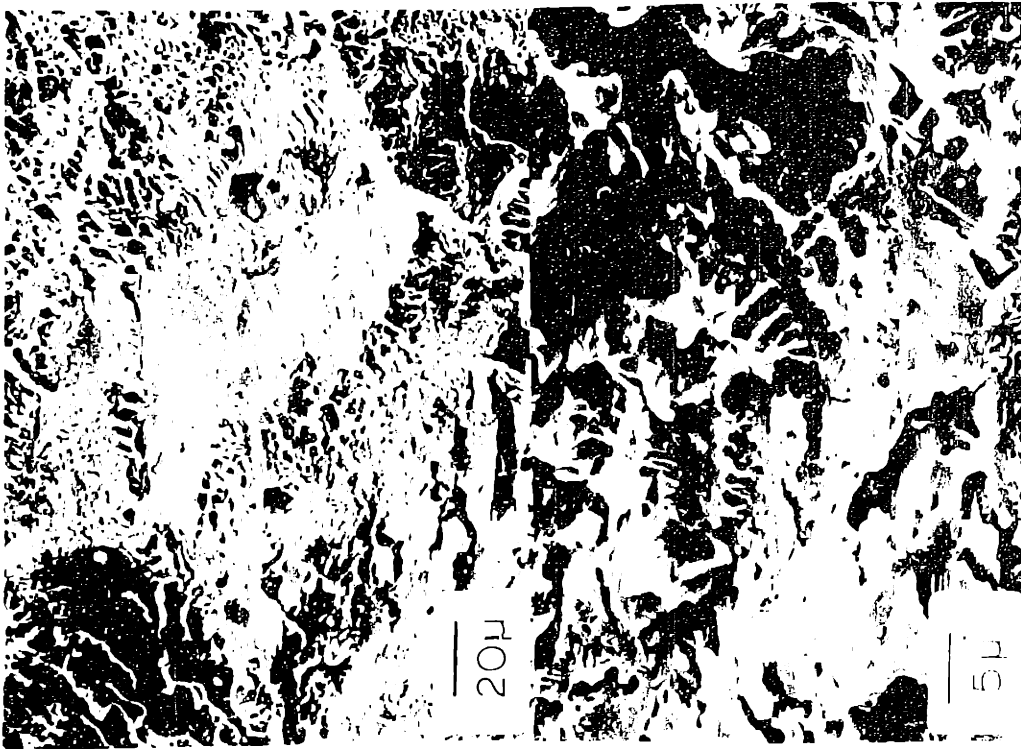


Figure 2. Scanning electron micrographs of the 3305-3A material. (a) and (b) are at 1000x magnification. (c) and (d) are at 5000x magnification.

Figure 3. Scanning electron micrographs of the 3305-3A material. (a) and (b) are at 1000x magnification. (c) and (d) are at 5000x magnification.

Figure 4. Scanning electron micrographs of the 3305-3A material. (a) and (b) are at 1000x magnification. (c) and (d) are at 5000x magnification.

Figure 5. Scanning electron micrographs of the 3305-3A material. (a) and (b) are at 1000x magnification. (c) and (d) are at 5000x magnification.

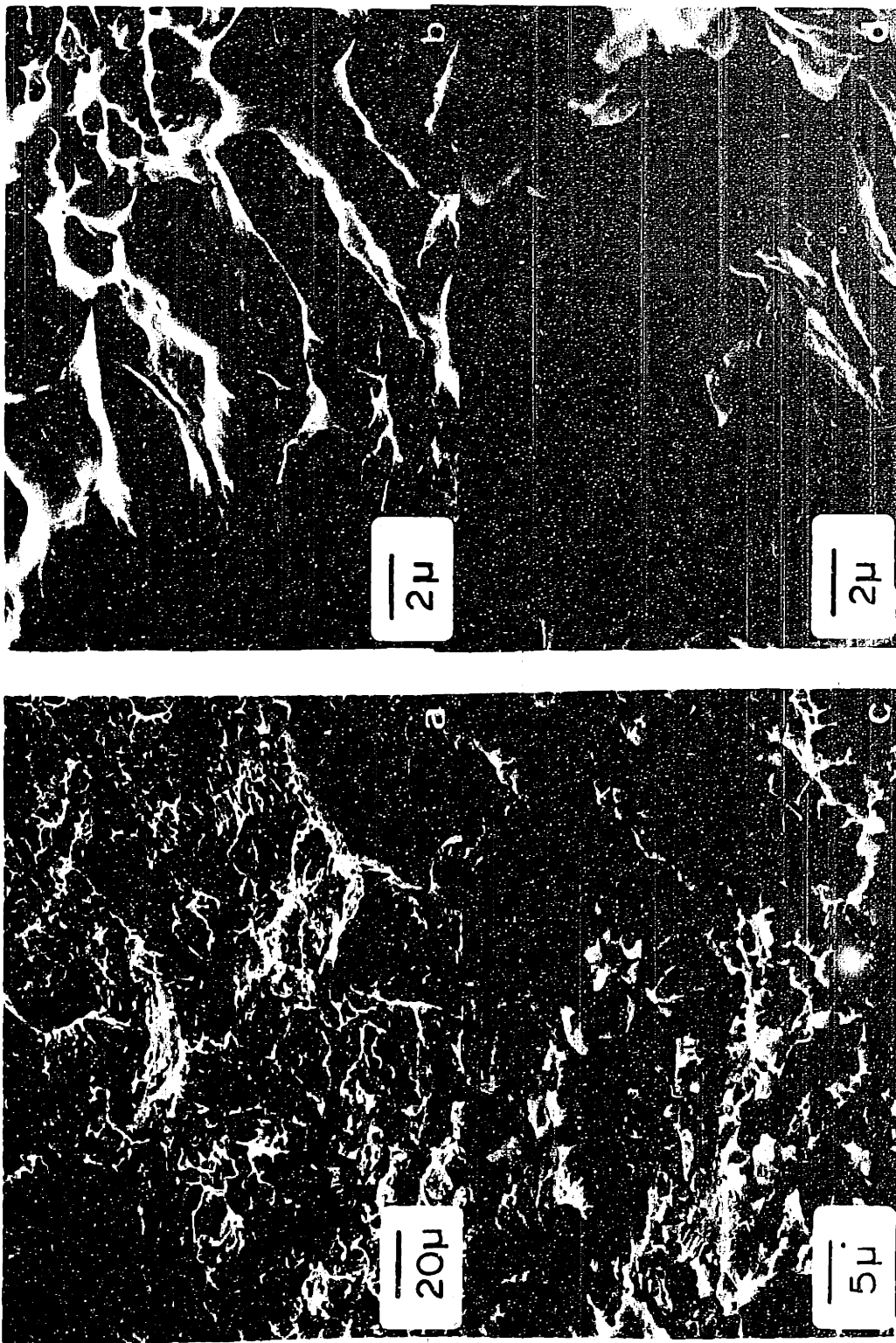


Figure 7.13 Scanning electron micrographs of the 9908-3A material, NT orientation tested under 40 Pa of iodine at 310°C (a) SCC region near the mechanical overload region at the top left (b) Flutes (c) SCC region showing embryonic ductile features ("stitching") (d) Detail of transgranular cleavage

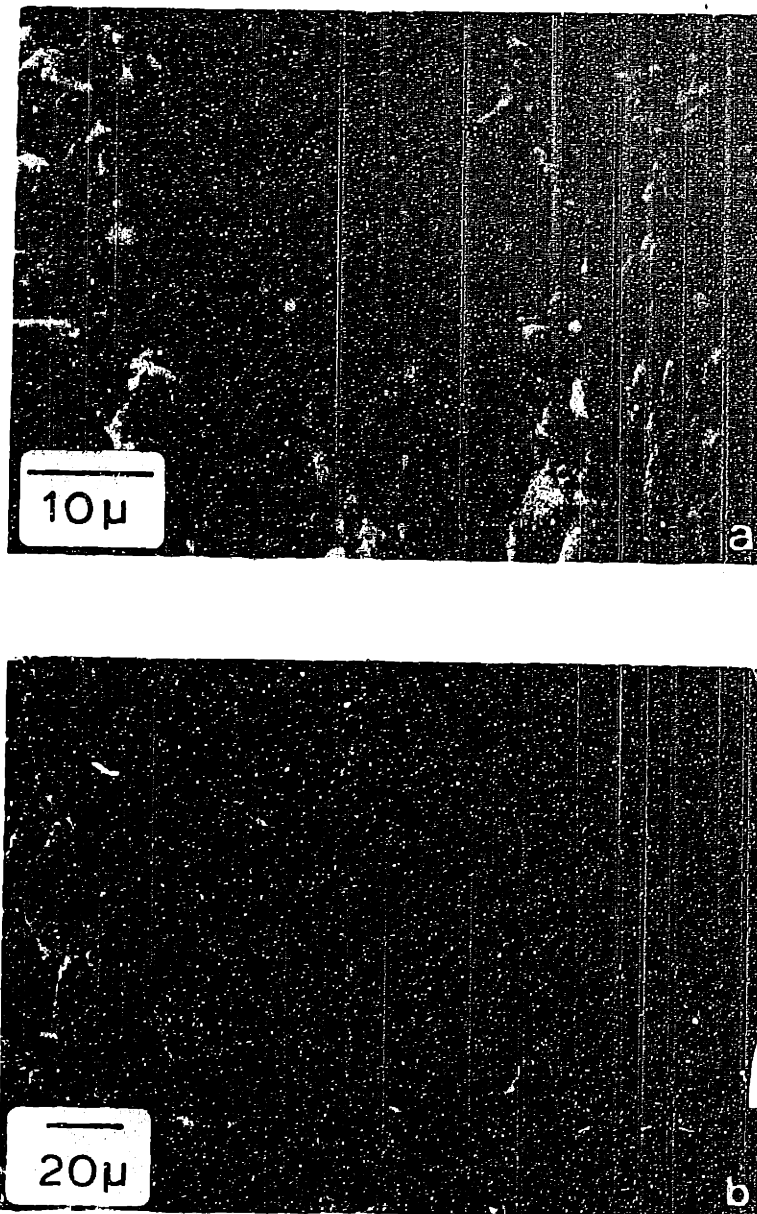


Figure 7.14 Scanning electron micrographs of the 9912-SR material, TL orientation tested under 40 Pa of iodine at 310°C (a) Corroded fracture surface, (b) Clean fracture surface showing transgranular cleavage

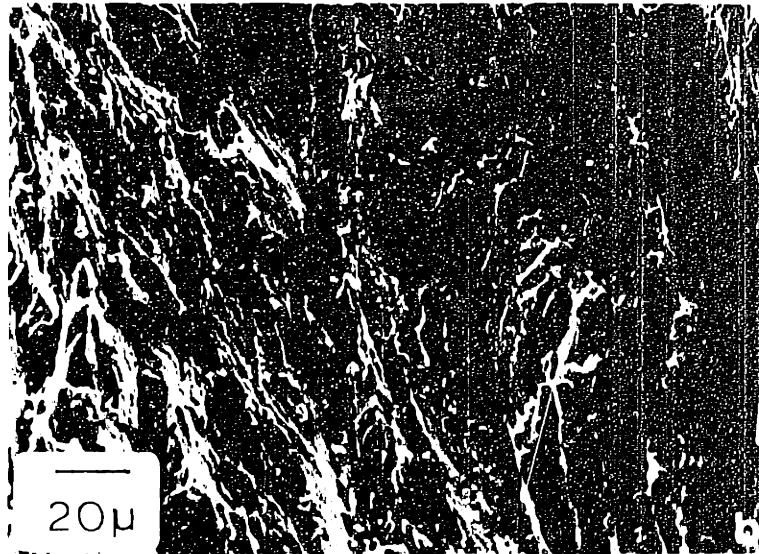


Figure 7.14 Scanning electron micrographs of the fracture surface of a fiber orientation tested in parallel to the fiber axis at 20°C. (a) Parallel fracture surface, and (b) perpendicular to the fiber axis (transverse fracture).

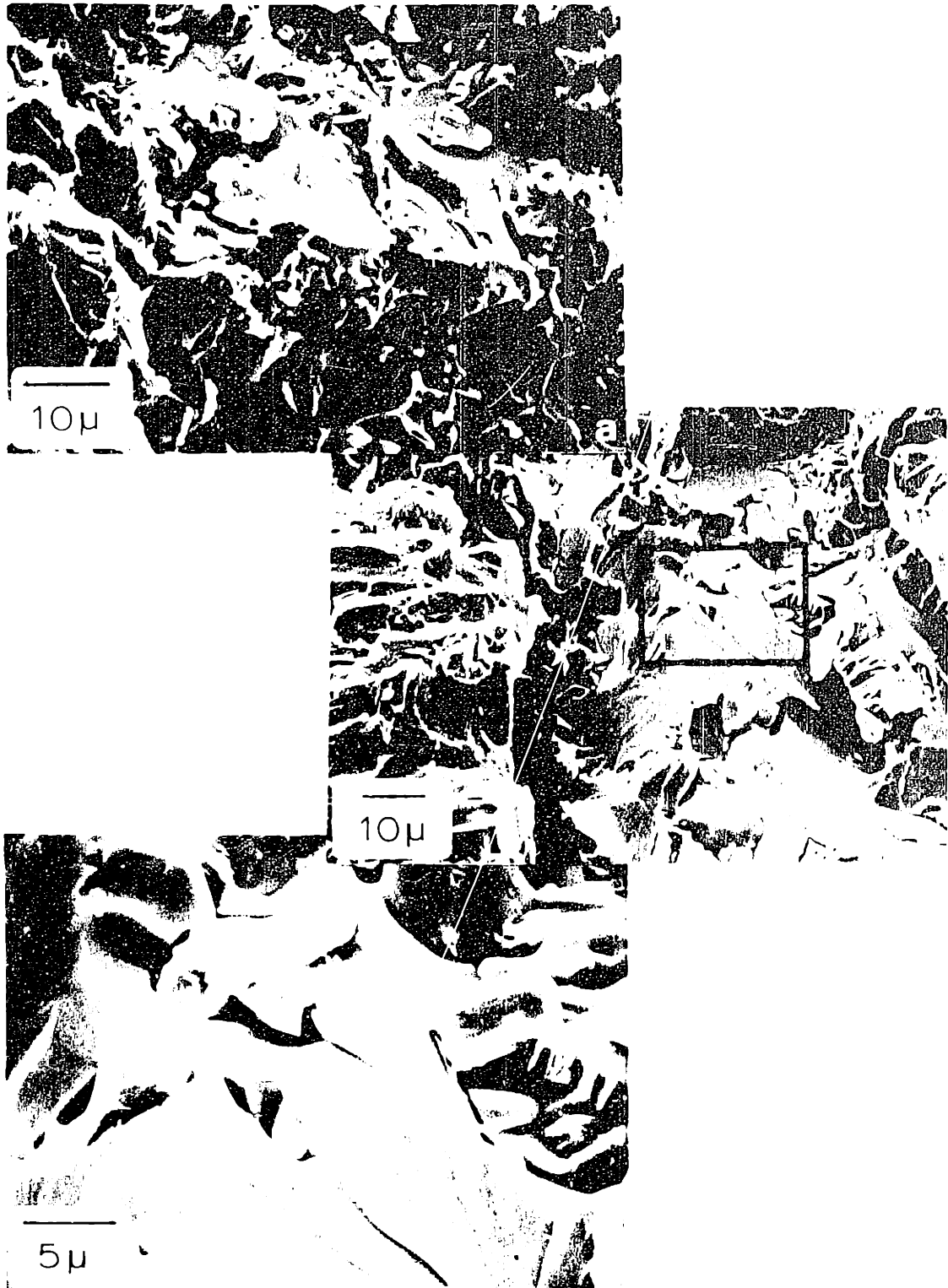


Figure 7.15 Fracture surface of the recrystallized Al alloy plate, 001 orientation tested at 310°C under 40 Pa of iodine.
 (a) Transgranular cleavage at high K . (b) Transgranular cleavage at low K ($\approx 10 \text{ MPa}\sqrt{\text{m}}$) (c) Enlargement of inset area in (b) showing river patterns

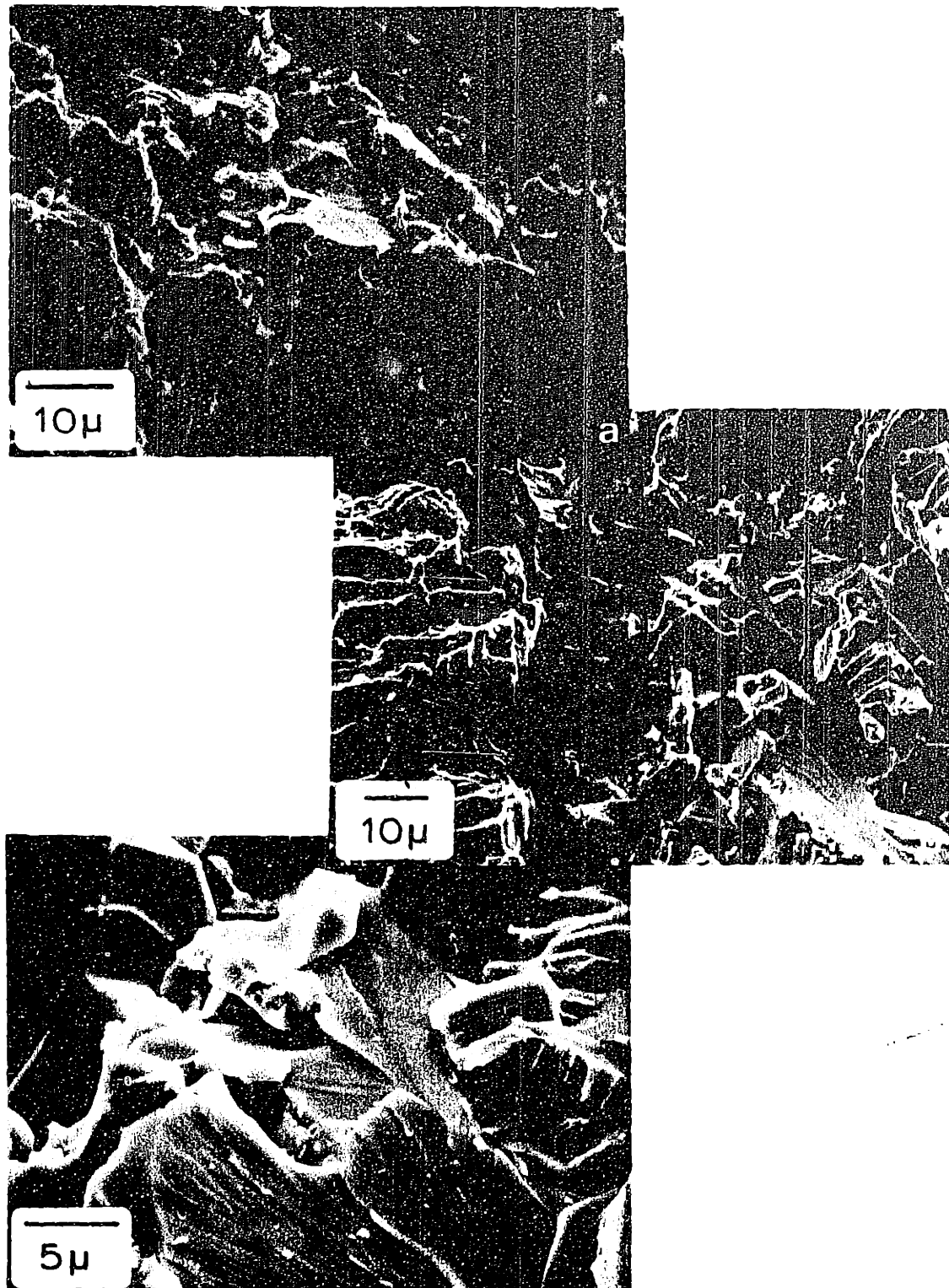
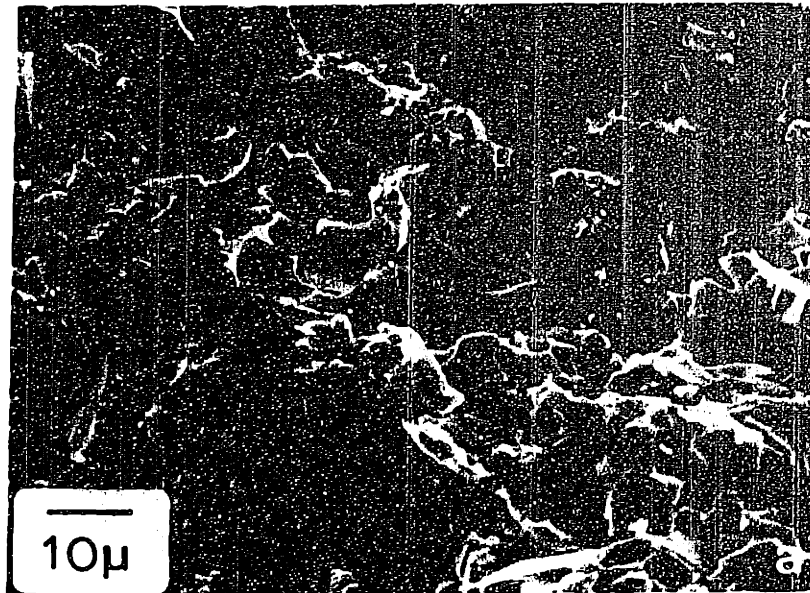
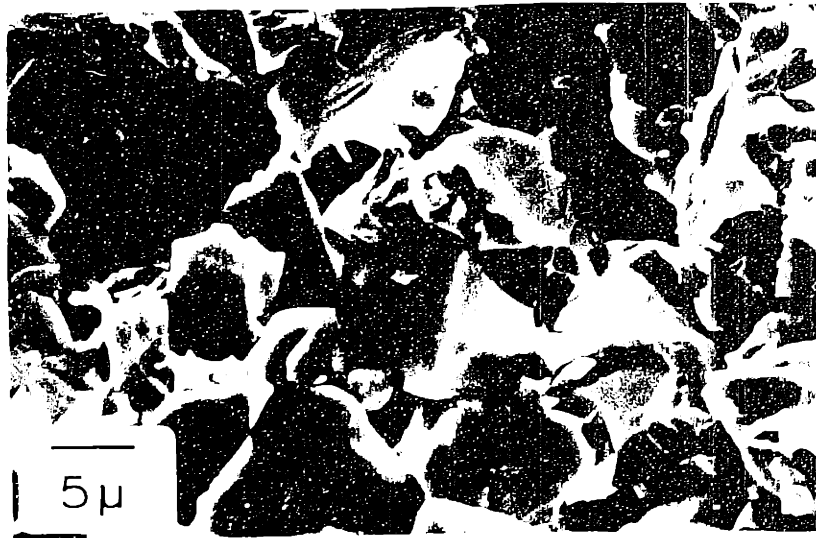
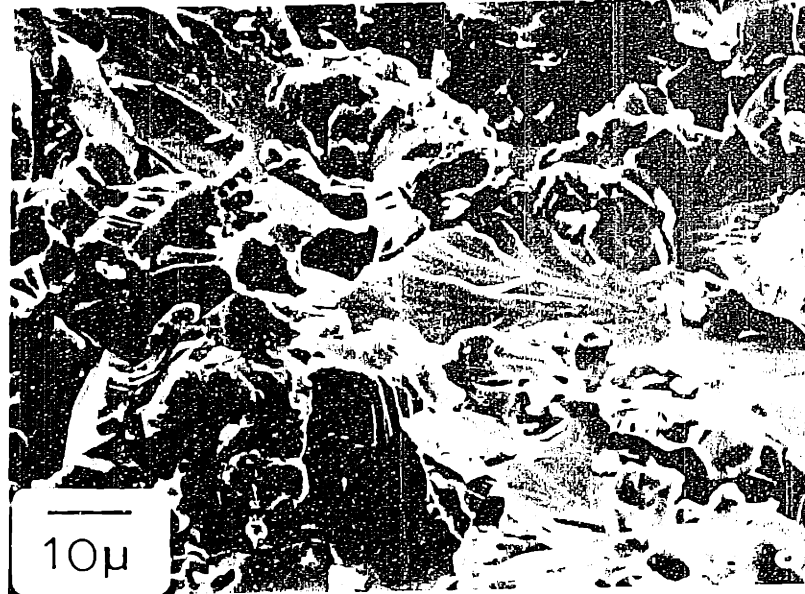


Figure 7.15 Fracture surface of the recrystallized Zircaloy plate, NL orientation tested at 310°C under 40 Pa of iodine.
 (a) Transgranular cleavage at high K (b) Transgranular cleavage at low K (~ 10 MPa m) (c) Enlargement of inset area in (b) showing river patterns



7.16 Fracture surface of the recrystallized Zircaloy material, NL orientation tested under 40 Pa of iodine at 310°C. K approximately $10 \text{ MPa}\sqrt{\text{m}}$ (a) transgranular cleavage, (b) Intercrystalline fracture.



7.16 Fracture surface of the recrystallized Zircaloy material, NL orientation tested under 40 Pa of iodine at 310°C. K approximately 10 MPa \sqrt{m} (a) transgranular cleavage, (b) Intercrystalline fracture.

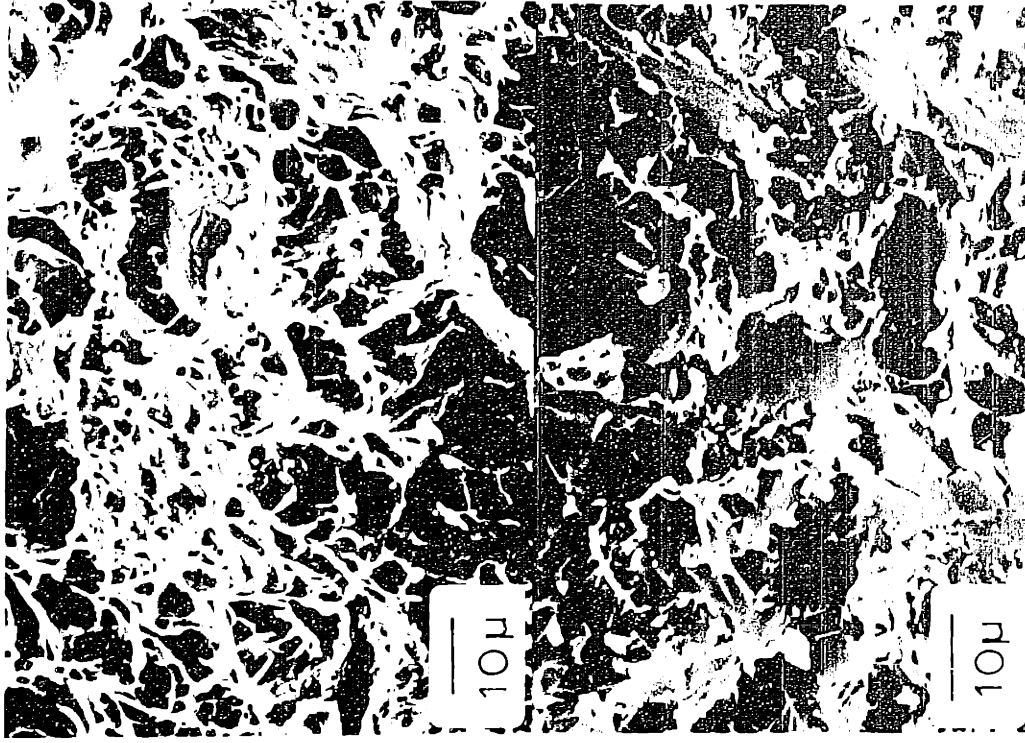
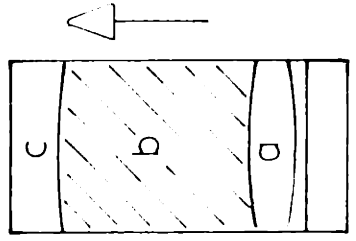


Figure 7.17 Scanning electron micrographs of the fracture surface of the recrystallized Zircaloy plate, 1/4 orientation tested at 310°C under 40 Pa of iodine. (a) Fatigue striations in the precrack region (b) Transgranular cleavage in the SCC zone (c) Dimples in the mechanical overload region



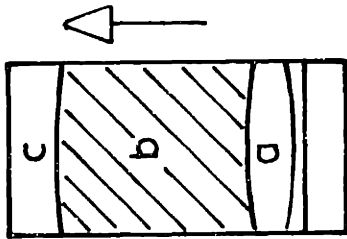
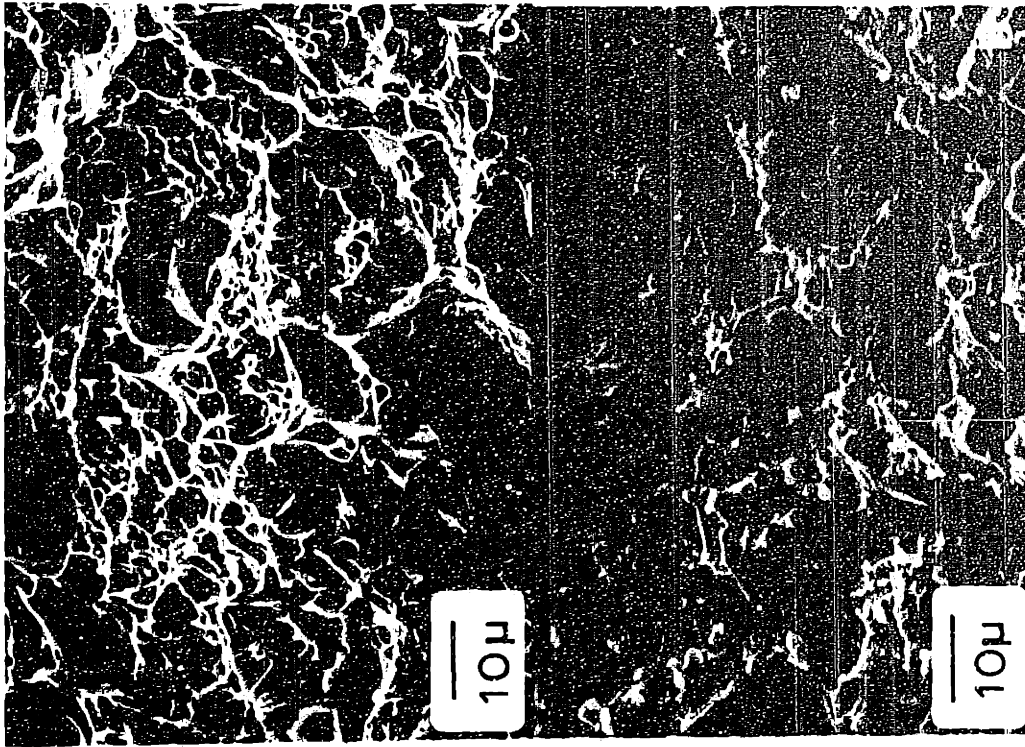


Figure 7.17 Scanning electron micrographs of the fracture surface of the recrystallized Zircaloy plate, NL orientation tested at 310°C under 40 Pa of iodine. (a) Fatigue striations in the precrack region (b) Transgranular cleavage in the SCC zone (c) Dimples in the mechanical overload region

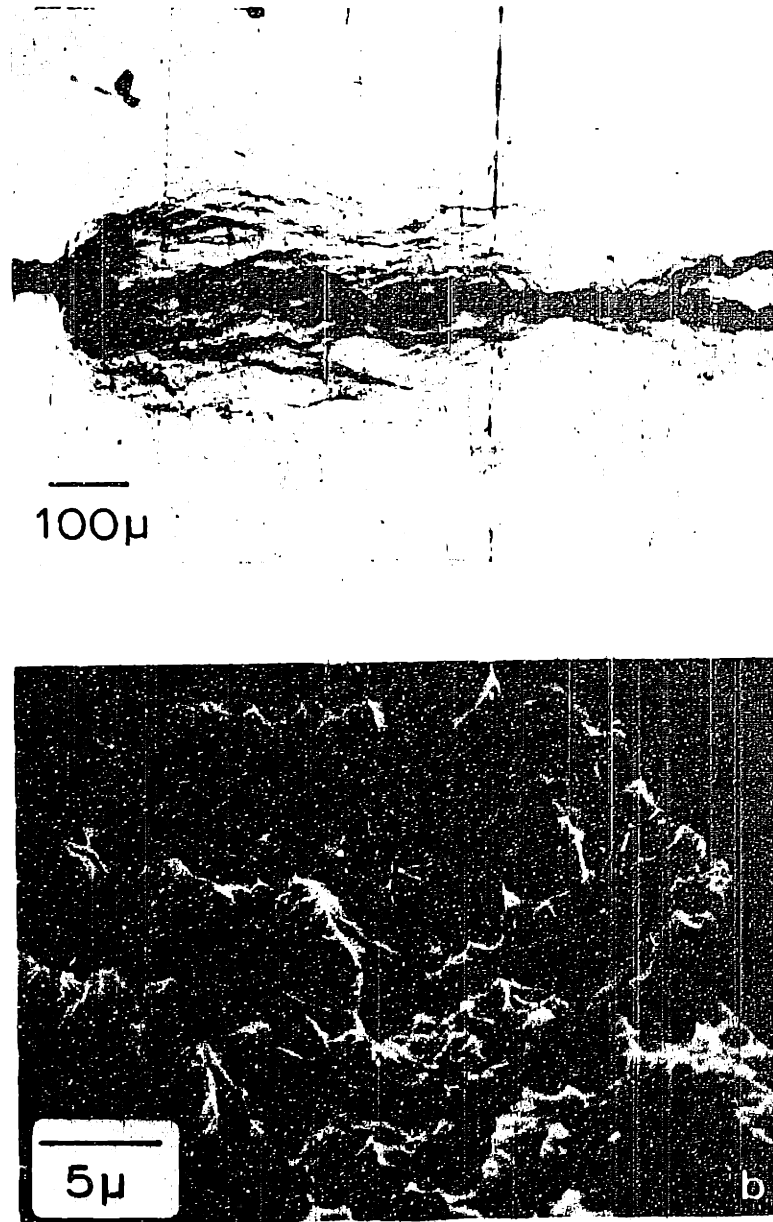


Figure 7.18 (a) Optical micrograph of the stress corrosion crack near the notch in the 9912-SR plate NT orientation, tested under 40 Pa of iodine at room temperature, (b) Scanning electron micrograph of the SCC region

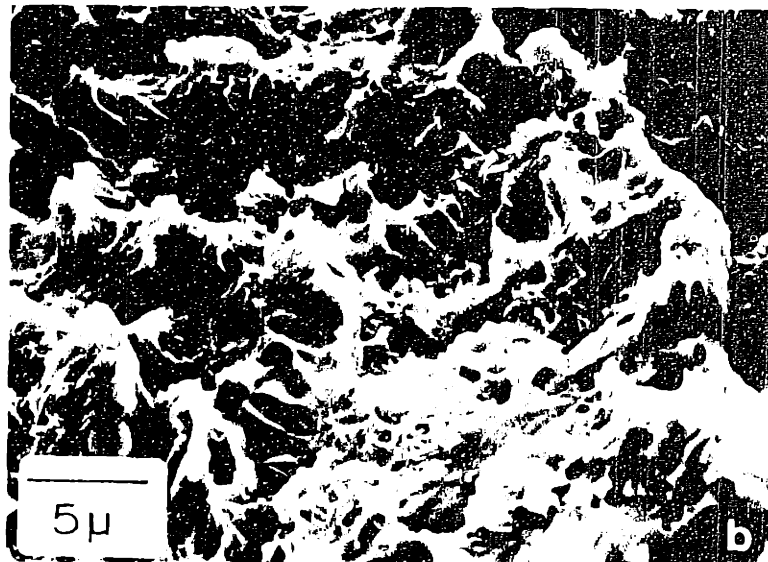
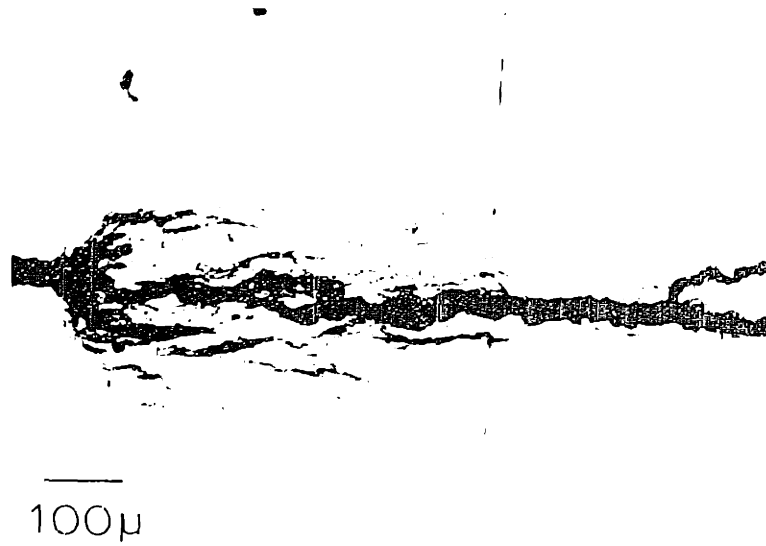


Figure 7.18 (a) Optical micrograph of the stress corrosion crack near the notch in the 9912-SR plate NT orientation, tested under 40 Pa of iodine at room temperature, (b) Scanning electron micrograph of the SCC region

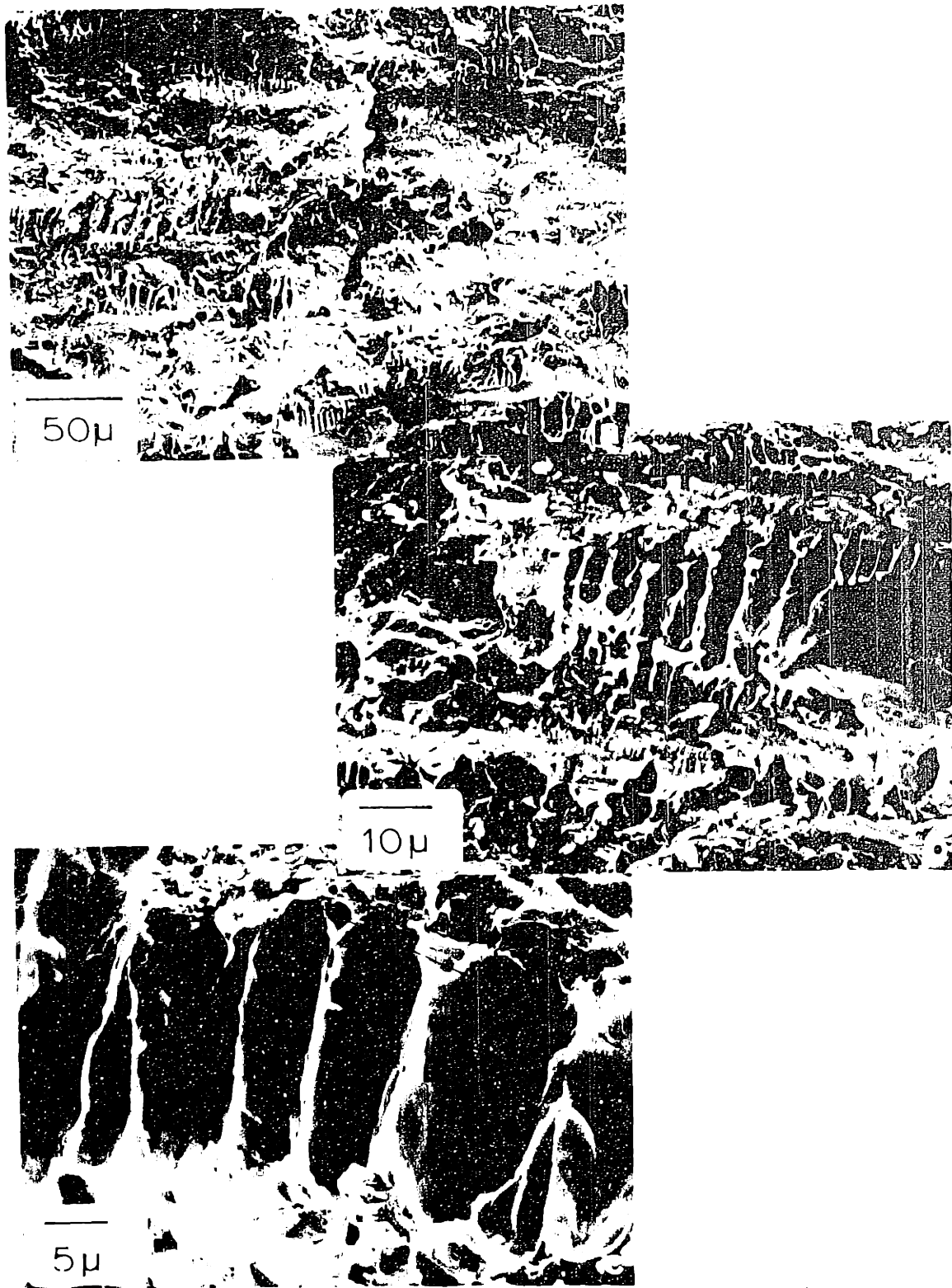


Figure 7.1 Fracture surface of low-β-β-titanium alloy, showing a ductile fracture process. The fracture surface is highly textured, with a complex network of ridges and valleys. The fracture process is highly ductile, and the fracture surface is highly textured. The fracture surface is highly textured, with a complex network of ridges and valleys. The fracture process is highly ductile, and the fracture surface is highly textured.

INTENTIONAL DUPLICATE EXPOSURE

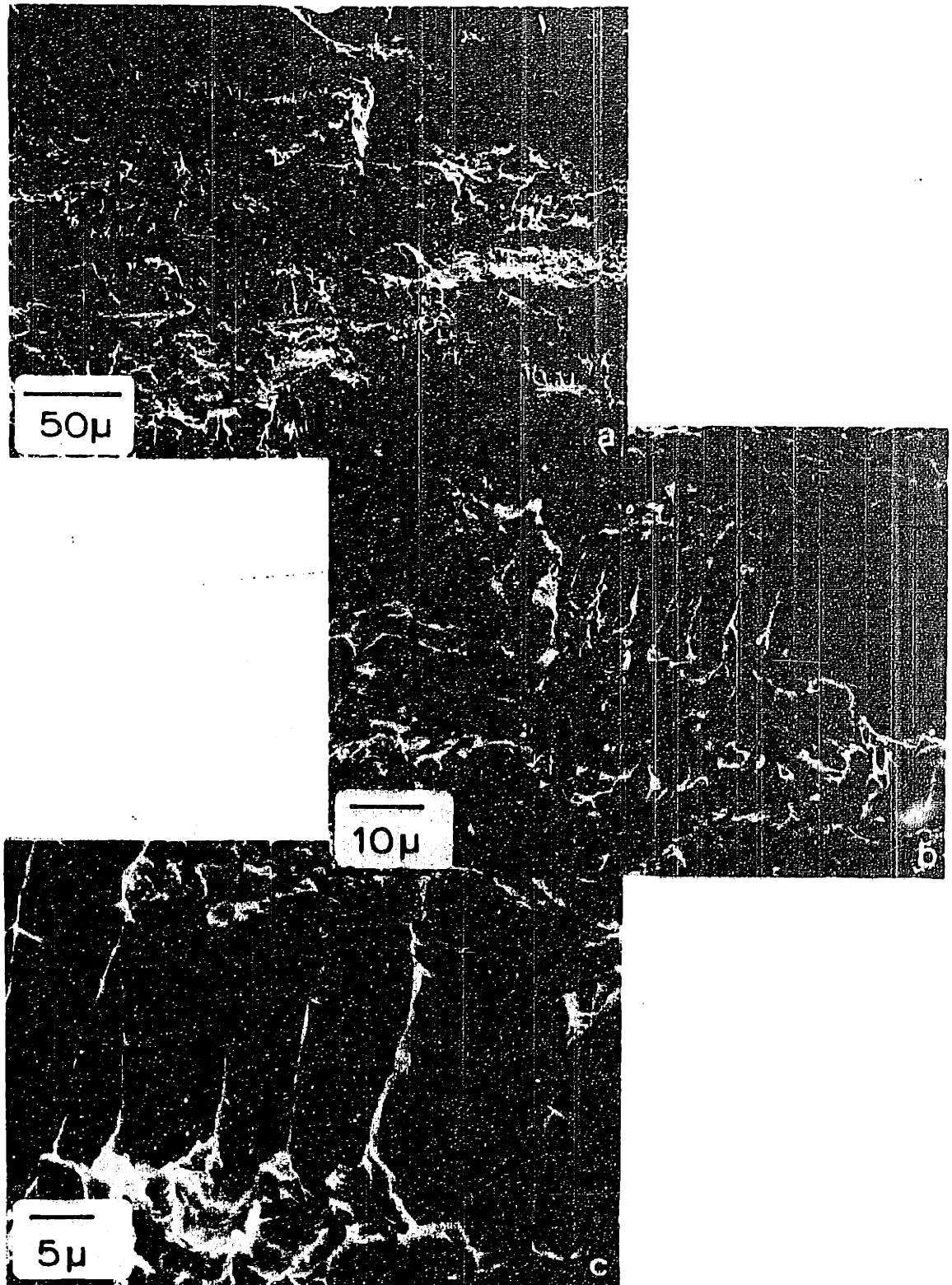


Figure 7.19 Fracture surface of the 9912-SR Zircaloy material, .1T orientation tested under 40 Pa of iodine at room temperature showing fluting plus transgranular cleavage at three magnifications.

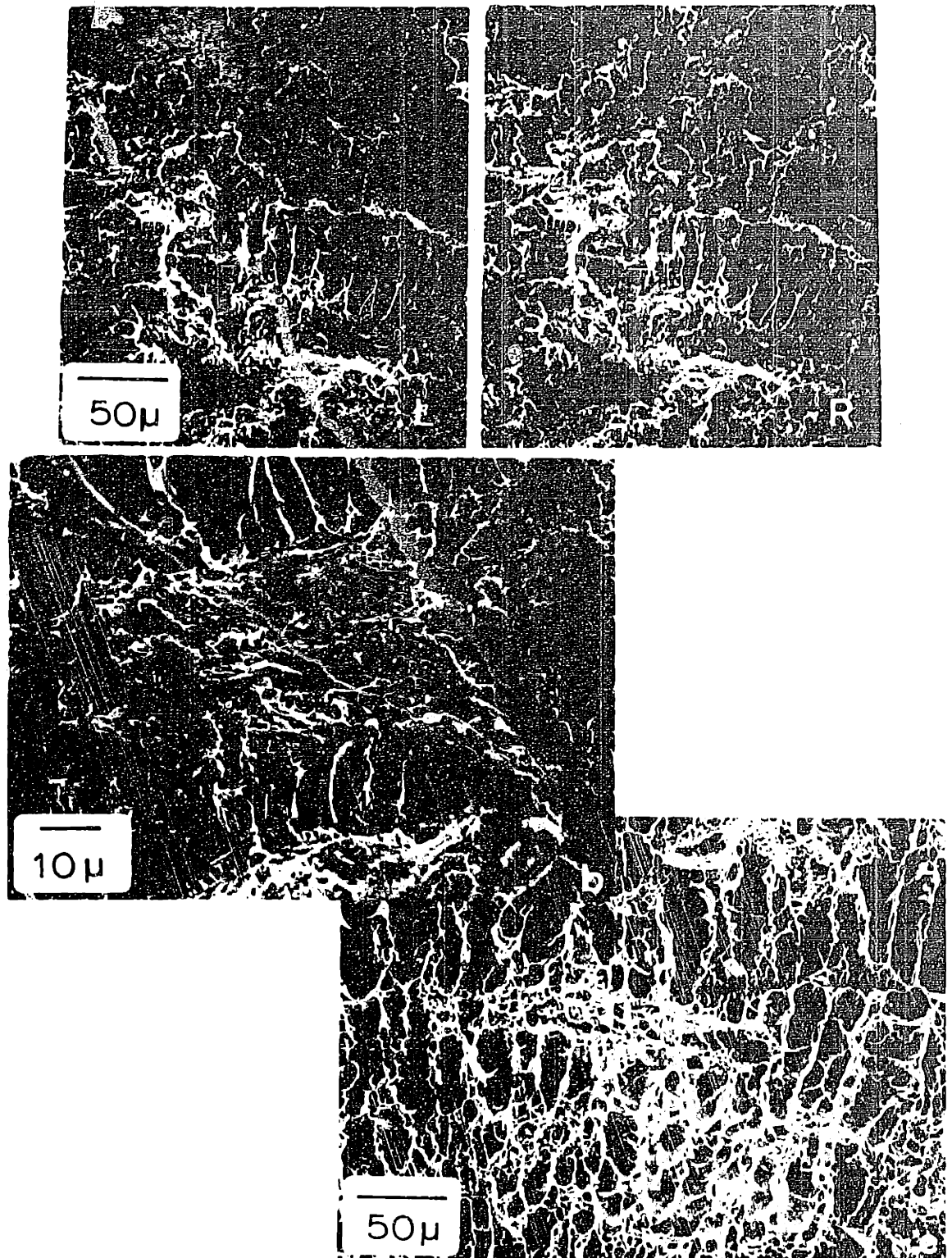
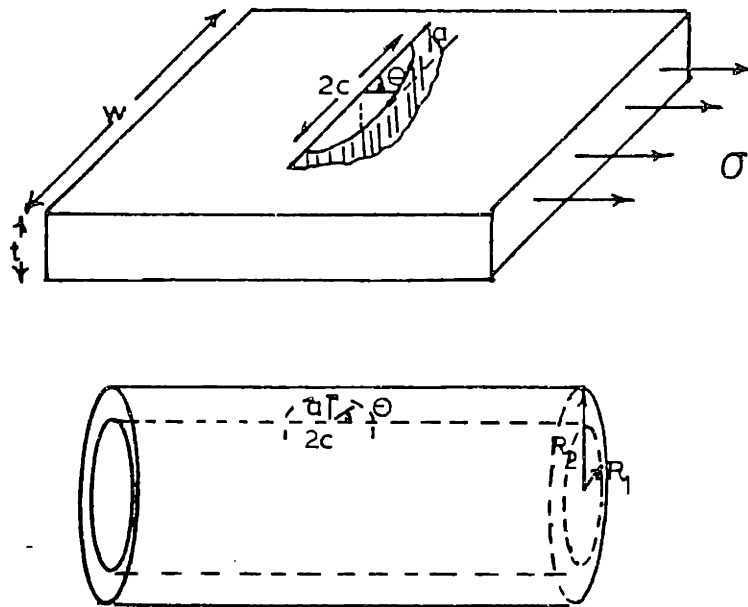


Figure 7.20 Scanning electron micrographs of the fracture surface of the 9912-SR Zircaloy plate, AT orientation tested under 40 Pa of iodine at 100°C. (a) Stereo pair showing fluting plus transgranular cleavage, (b) SCC region at low K , (c) Fluting plus dimples in the fast fracture region.



semi-elliptical cracks

Figure 7.21 Schematic of semi-elliptical crack

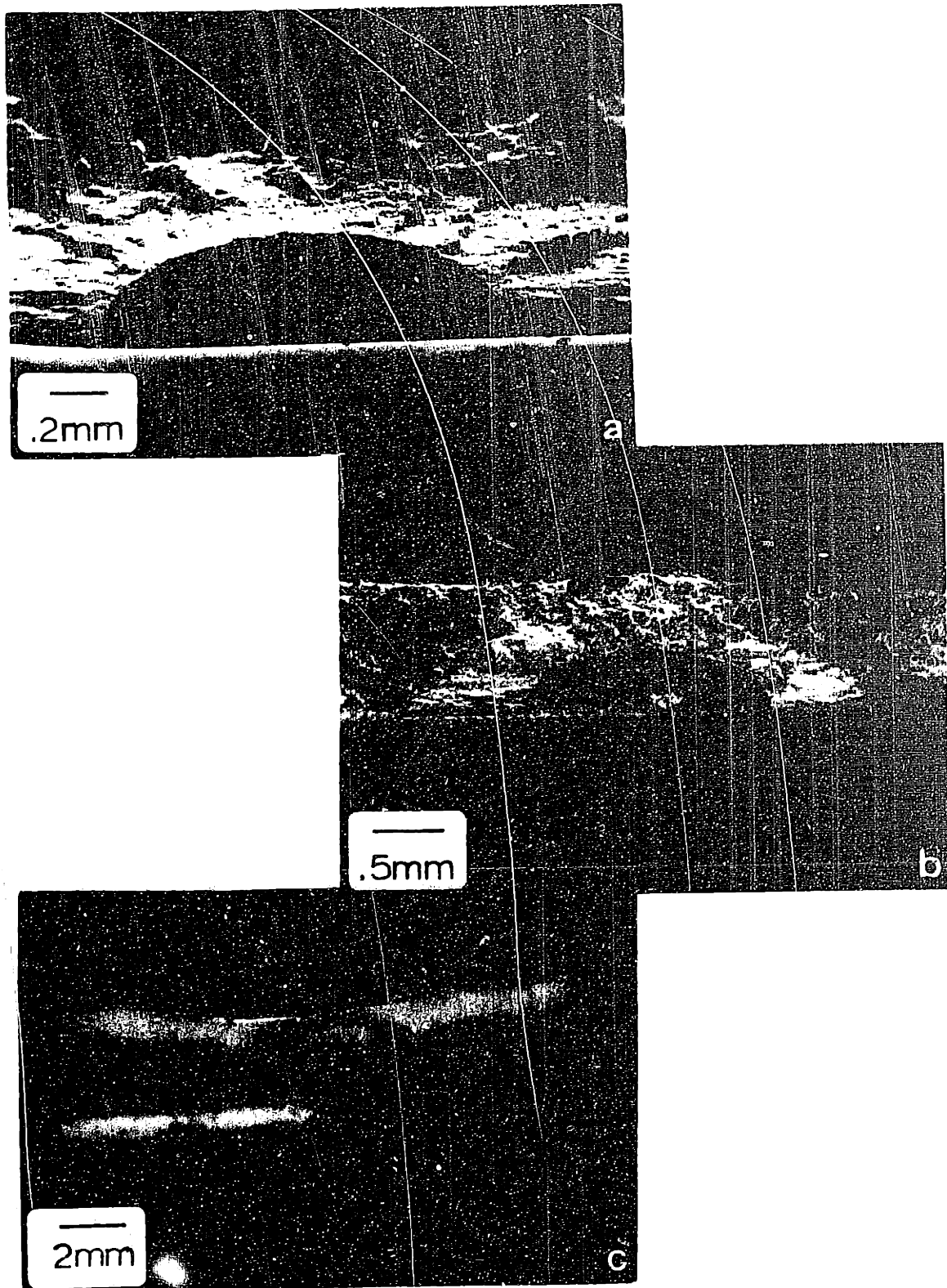
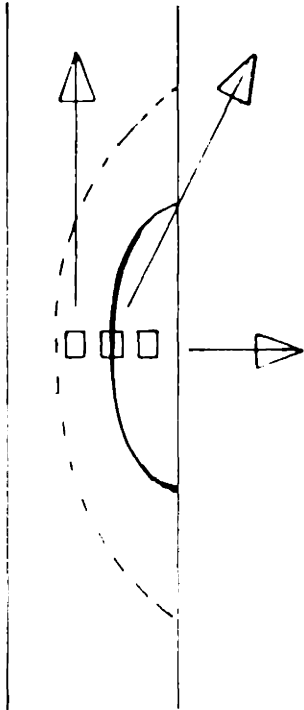
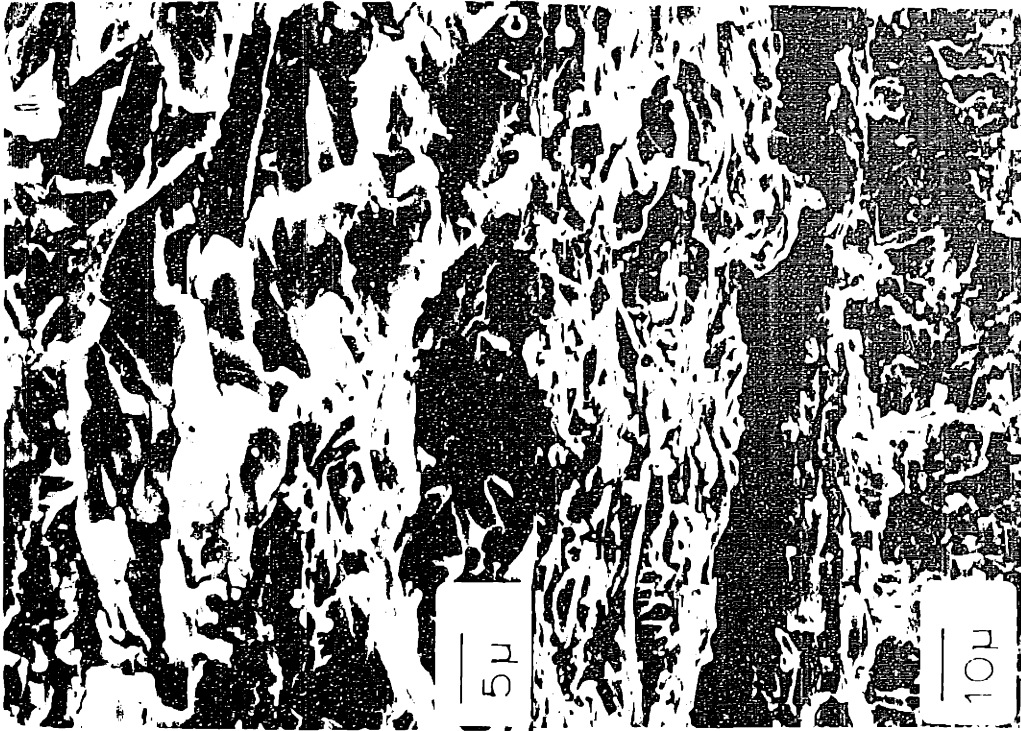


Figure 7.22 General view of the fracture surface of the tubing material.
 (a) Supplier A, SEM micrograph (b) Supplier B, SEM micrograph
 (c) Supplier B, optical micrograph





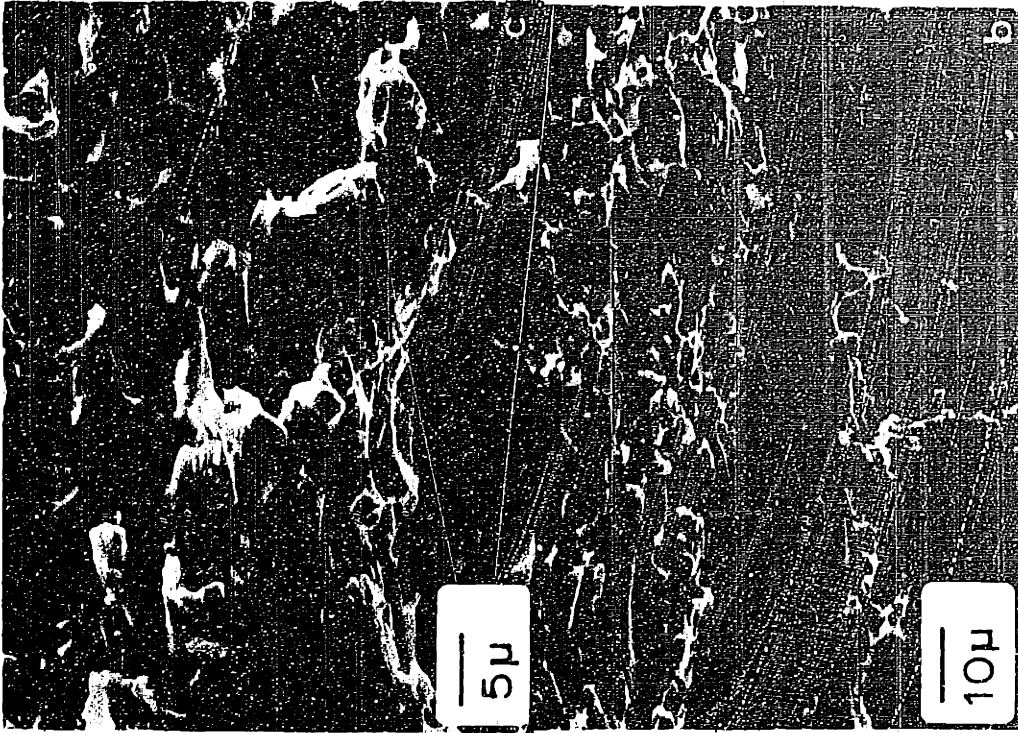
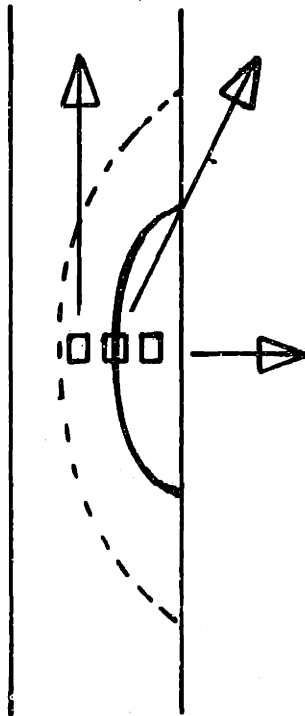


Figure 7.23 Scanning electron micrographs of the Supplier B tubing material (specimen 32) tested at 320°C with 0.2 mg/cm² of iodine under a stress of 37.5 ksi. (a) Detail of the fatigue precrack zone, (b) Transition from fatigue region to SCC region, (c) Transgranular cleavage in the SCC region



(a)

(b)

(c)

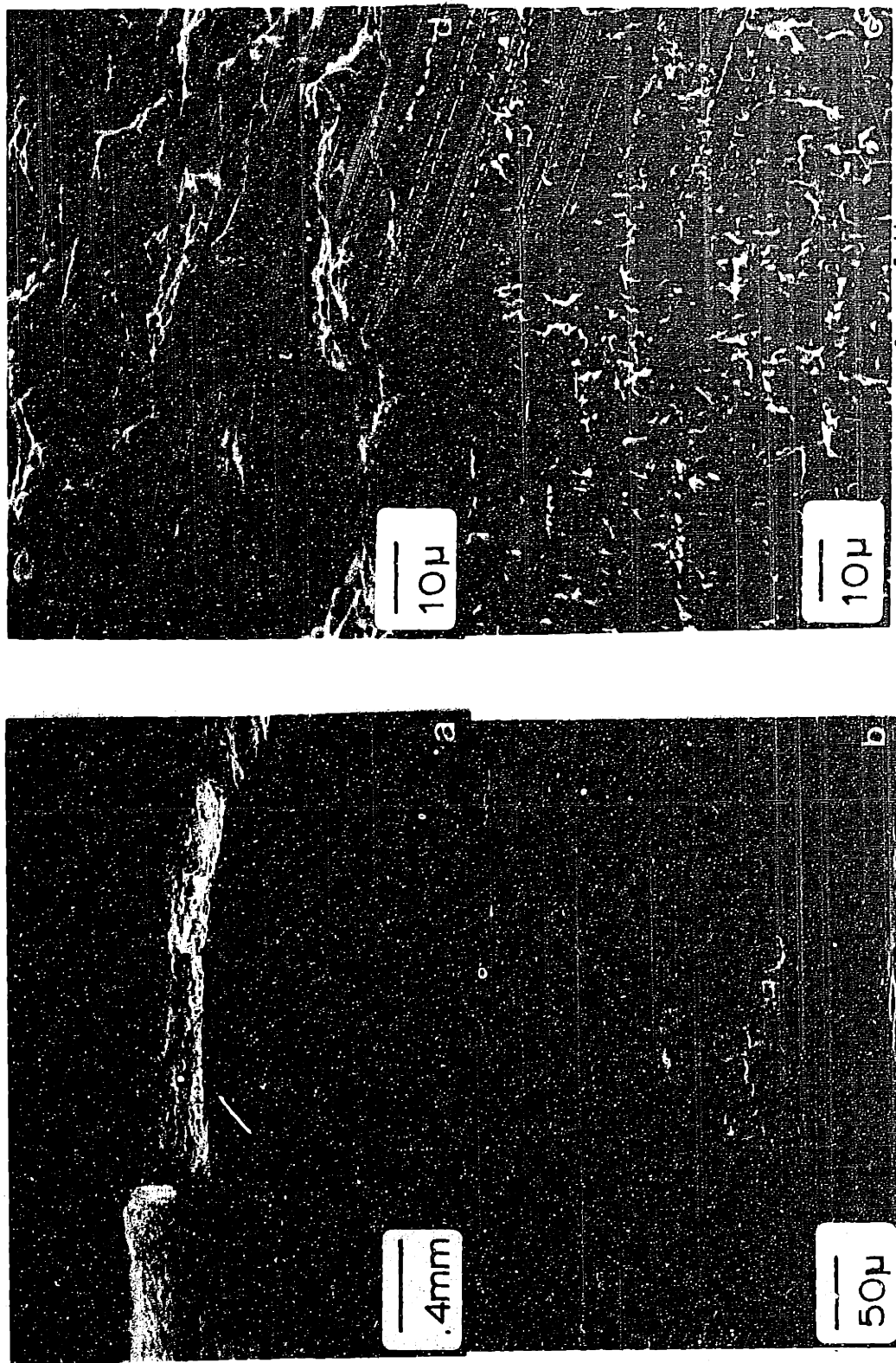
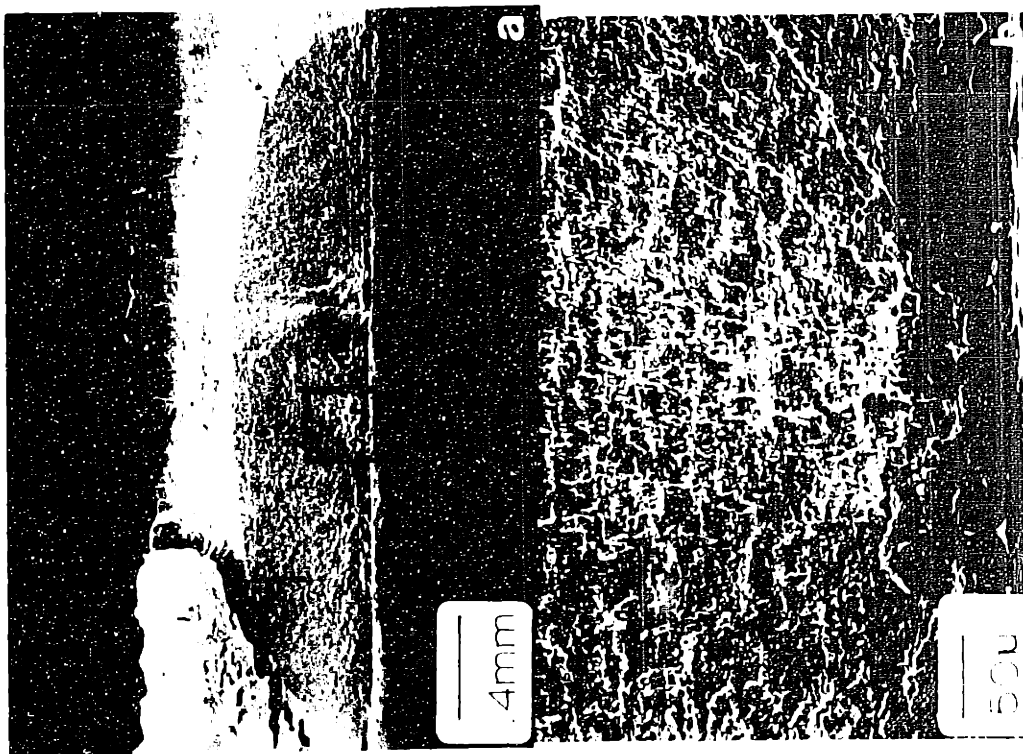
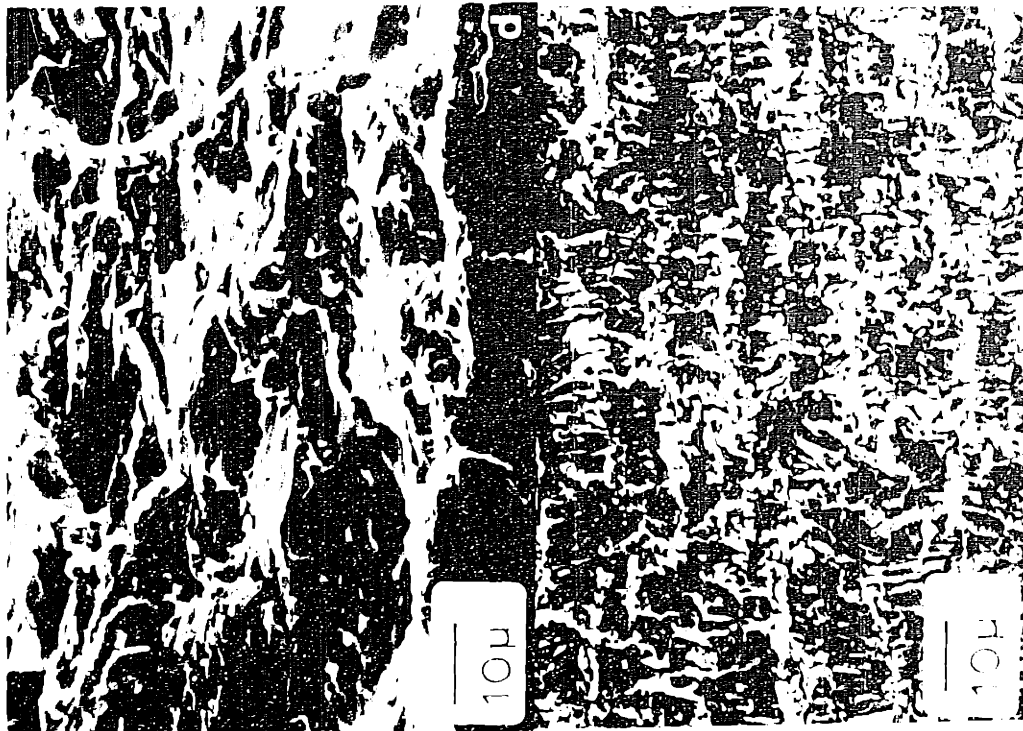
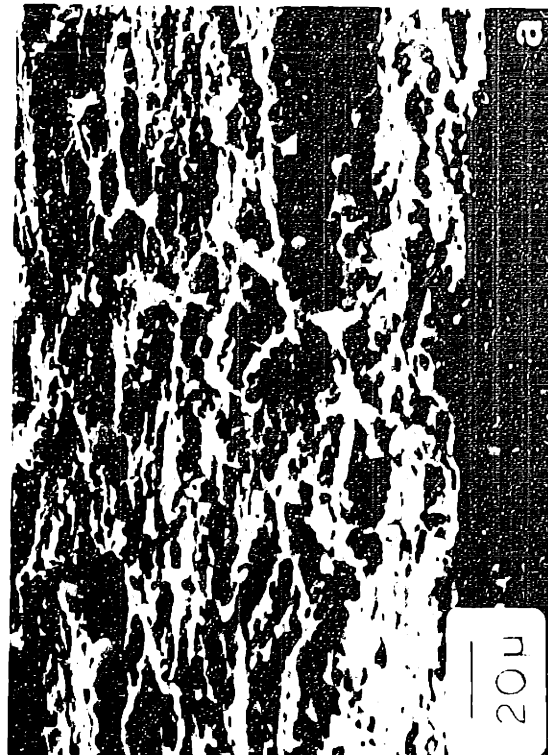
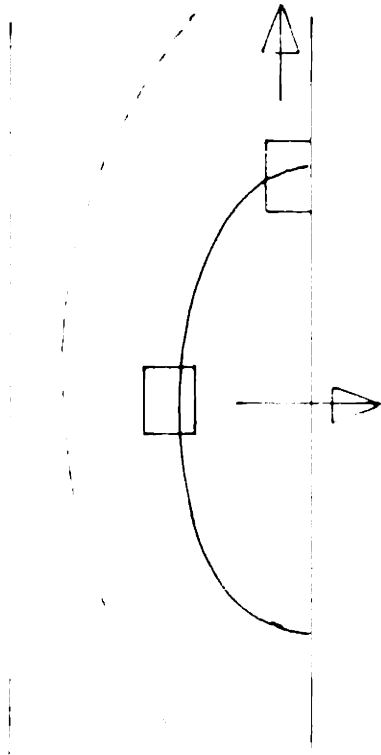


Figure 7.24 Scanning electron micrographs of the fracture surface of the Supplier B tubing material (specimen B4) tested at 320°C with 0.2 mg/cm² of iodine under a stress of 37.5 ksi. (a) General view, (b) Detail of the precrack zone of (a) (c) & (d) higher magnification of the fatigue region (ii) 300 zone



INTENTIONAL DUPLICATE EXPOSURE



INTENTIONAL DUPLICATE EXPOSURE

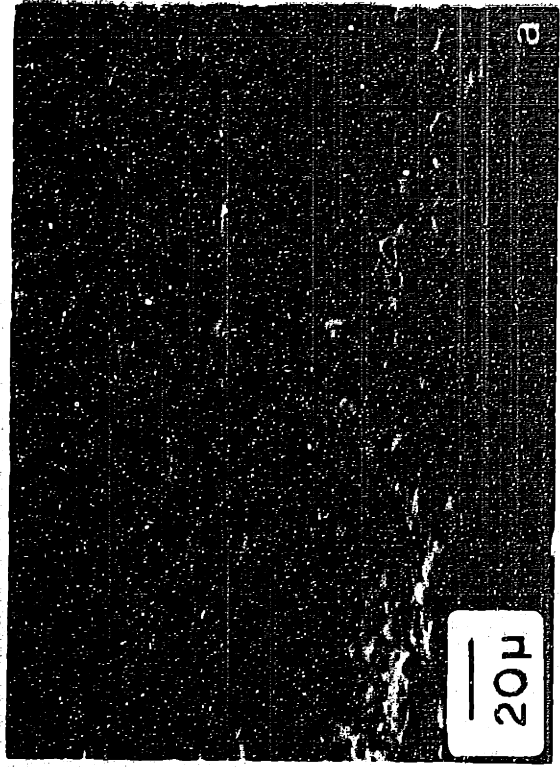
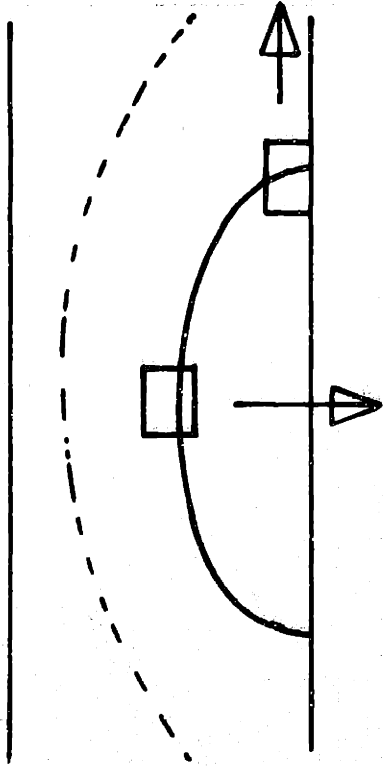
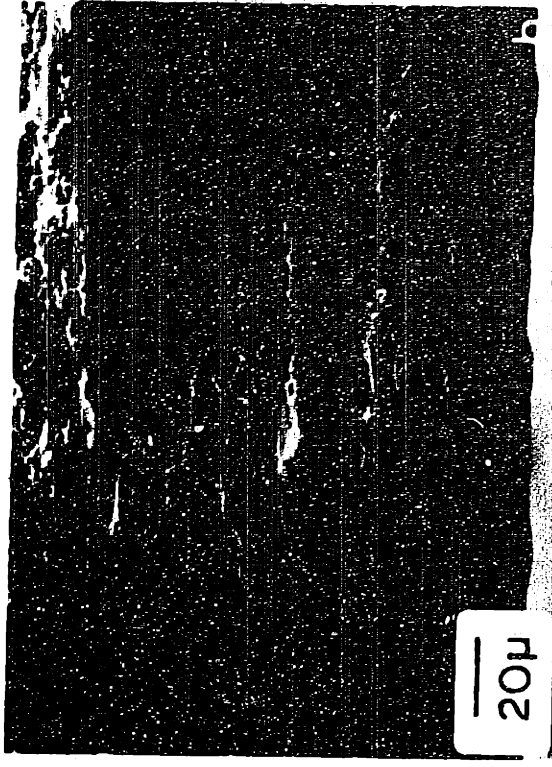


Figure 7.25 Scanning electron micrographs of the fracture surface of the Supplier A tubing material (specimen A2) tested at 320°C with 0.2 mg/cm² of iodine under a stress of 42.0 ksi showing transition zone between fatigue and SCC (a) Deepest point of fatigue precrack (b) surface intersection point

8. DISCUSSION

8.1 Mechanism of Cracking

Basically, there are two questions to the problem of stress corrosion crack growth: what causes the crack to grow and what factors control the crack rate.

The environment or its components must react with the material at or near the crack tip to reduce the energy requirements for crack growth. The argument against an electrochemical mechanism for cracking of zirconium alloys in iodine vapor around 300°C is that in this environment (high temperature and low iodine pressure) no liquid phases are possible. Thus, both iodine and the zirconium iodides exist only as solid or vapor species (in a pure system) and furthermore both reactants and products are covalent compounds (50). Electrochemistry seems unlikely to play any role in the processes occurring under these conditions.

The hypothesis of an adsorption-type mechanism which reduces the Zr-Zr bond strength in certain crystallographic directions at the crack tip is the most plausible explanation for the predominantly transgranular crack propagation in the I-SCC of Zircaloy (51).

The study done by Krishnan et al. (52) provides a better understanding of the chemisorption process of iodine on clean zirconium surfaces and the thermodynamic stability of the chemisorbed state. Krishnan et al. have used Auger electron spectroscopy (AES) to monitor the relative coverage of a zirconium crystal exposed to a flux of iodine gas molecules. The zirconium is heated to temperatures

in the range 1000-1300 K, and the iodine pressures correspond to 10^{-4} - 10^{-6} Pa. Under these conditions of temperature and pressure, they postulate that the interaction between gaseous molecular iodine and zirconium involves the following sequence: the iodine molecules that strike the metal surface and become thermalized will dissociate since thermodynamic data (53) predict that monoatomic iodine will be several orders of magnitude more abundant than molecular iodine. Therefore, the iodine can be assumed to be monoatomic in its interaction with the zirconium. The iodine striking the surface either adheres to form an adsorbed layer on the metal or it evaporates into the gas. The iodine that adheres to the surface forms a chemisorbed layer from which volatile species can then evaporate, as illustrated schematically in Figure 8.1.

Krishnan et al. results show that iodine chemisorbed on zirconium is thermodynamically more stable than combined in the zirconium iodides. In the overall process of iodine-induced SCC of zirconium alloys this has the following significance. Iodine can initially react with exposed zirconium surface and the solid iodide available to be transferred at a later time to fresh zirconium surface that might be formed when the metal is strained. The mechanism by which iodine can be transferred is not elucidated by these thermodynamic considerations but surface diffusion of iodide species or vapor transport as ZrI_4 gas are possibilities.

8.2 Influence of the Crystallographic Texture

Due to the predominantly crystallographic transgranular cracking of iodine-induced SCC of Zircaloy, it is not surprising that texture influences the velocity and morphology of crack propagation, as shown by our results.

Hence, texture that aligns basal poles toward the tensile stress axis should increase the rate of subcritical crack growth at a given stress intensity factor value. The crack growth rate for the plate 9908-3A, NT orientation ($f_N = 0.70$) is the highest among those specimens tested at 310°C. Also, the rates of crack growth for specimens of plate 9912-SR in both NL or NT orientation ($f_N = .56$) are higher than that for the TL orientation ($f_T = 0.33$) as shown in Figure 7.6.

8.3 Effect of Microstructural Directionality

Independently of the texture effects, the microstructural directionality of the grains also affects the rate of crack growth. The grains tend to become elongated in the rolling direction during fabrication leading to anisotropy of the growth rate, i.e., the velocity of cracks in specimens of NL orientation (crack growth parallel to the rolling direction) are higher than those for specimens in the NT orientation (crack growth normal to the rolling direction) for all values of the parameter K tested at 310°C.

In Figure 7.6 one can also observe that decreasing the iodine pressure by a factor of 10 causes a small decrease in the crack growth

rate (plate 9912-SR, NT orientation).

8.4 Influence of Heat Treatment

As shown in Figure 7.7 the crack velocities for stress relieved Zircaloy are higher than those for recrystallized Zircaloy at a given stress intensity factor value. In a qualitative sense, this is consistent with the higher mechanical strength and lower ductility of the stress relieved material. In addition, the extrapolation of the curves to obtain the apparent threshold values, K_{ISCC} , corroborates the results by Knorr and Pelloux (32) who have found that the threshold K_{ISCC} for cold worked, stress relieved Zircaloy is lower than for recrystallized material.

The results above are in contradiction with those presented by Videm and Lunde (35) who get the much lower crack growth rates for stress relieved Zircaloy.

In a number of iodine containing environments (54) the SCC growth in Zircaloy appears to start as an intergranular chemical process and changes to a transgranular propagation process. In DCB-type specimens the stress intensity at the crack tip decreases as the crack extends. Some evidence of intergranular cracking is observed in the recrystallized condition material at low stress intensity factor values (near K_{ISCC}) as presented in Figure 7.7. The crack growth rates for intergranular processes are much slower than for transgranular cracking. Cox and Wood (18) found no intergranular cracking at the low-K crack arrest region in stress relieved DCB

specimens tested in iodine vapor at 300°C. This strengthens the conclusion that intergranular cracking seems to require a combination of suitable stress intensity factor value and heat treatment condition (recrystallized material).

Videm and Lunde (35) reported that they have observed both intergranular and transgranular cracking in stress relieved Zircaloy tubing, but they prefer not to specify where the change in the crack pattern occurs, because the heavily deformed grains make it difficult to separate trans- and intercrystalline SCC. On the other hand, Knorr and Pelloux (32) have observed a transition to completely intergranular failure in recrystallized Zircaloy plate near K_{ISCC} ; their explanation for the transition of fracture mode in recrystallized tubing is related to the low values of K for a short crack, even with a high nominal stress on the tube, which leads to intergranular fracture.

8.5 Effect of Temperature

There is usually a significant occurrence of fluting and other ductile processes during tests at lower temperatures (Figures 7.19 and 7.20); this is indicative of the high stress levels (high K values for a given crack depth) reached in the experiments since the fluted regions are associated with high local tensile strain (55). The flute spacing for a specimen tested at room temperature, for instance, is ca. 5 μm whereas the grain size is relatively small (15-25 μm).

The occurrence of fluting requires considerable expenditure of

strain energy in the process of crack propagation leading to a much slower growth rate as evidenced in Figure 7.8. This result is in conflict with results reported by Cox and Wood (18) who have found little or no difference in crack velocity for Zircaloy tested in iodine between 25° and 300°C. We cannot explain this difference between their data and our results.

It is also apparent in Figure 7.8 that the extrapolated K_{ISCC} value is displaced to higher stress intensity factor values as the temperature increases.

8.5.1 Apparent Activation Energy Q

The slope of the plot in Figure 7.9 is related to the apparent activation energy, Q, of Regime II crack growth. A direct comparison of this activation energy for environment enhanced crack growth with that for some chemical process, determined under conditions of "zero" stress, as a means of identifying the mechanism for stress corrosion cracking is not straightforward.

Kreyns et al. (57) have determined an activation energy for I-SCC, Q, equal to 42.9 and 35.9 kcal/mole for recrystallized and cold-reduced Zircaloy-4 tubing, respectively. They have used the data obtained by Busby et al. (19) on tests conducted at 360°C and 400°C in their analysis; Kreyns et al. have used a power law for crack growth based on Cox and Wood's (12) results on DCB specimens (exponent n equal to 4). The expression for the stress intensity factor calculations was a very simplified one.

On the other hand, Videm and Lunde (35) have obtained an activation energy for SCC crack growth of 17 kcal/mole from experiments with Zircaloy-2 tubing (both in recrystallized and stress relieved conditions) at 80 and 340°C. Here again the analysis of the crack growth process is too simplified.

8.6 Mechanism of Fluting

In a recent paper, Smith (56) has shown that ligament failure by the fluting mechanism is likely to occur by the movement of a fracture front along the direction AB across a ligament (Figure 8.2), i.e., parallel to the basal poles, when the fluting channels develop simultaneously rather than sequentially. The prime reason why this should be so is because slip occurs mainly on 1010 in $\langle 1210 \rangle$ directions; there is consequently little opportunity for slip along planes whose zone axis is the fracture front (dashed lines in Figure 8.2c).

8.7 I-SCC Growth in Zircaloy Tubes

One way to use the data of the tube pressurization tests of precracked tubes (Table 7.1) is to compare the experimentally determined time-to-failure with those times calculated using fracture mechanics techniques, and then try to deduce the times to crack initiation from experiments with smooth specimens.

Therefore, the objective is to calculate how long it will take for a crack of a given size to penetrate the cladding wall, at various

levels of applied stress.

The tube crack growth rate can be related to the stress intensity factor of the crack by an expression like

$$da/dt = A.K_I^n \quad 8.1$$

where A is a rate constant and n is the exponent.

8.7.1 Evaluation of the Stress Intensity Factor of the Semi-Elliptic Crack

Recently, Scott and Thorpe (58) have proposed that for thin shell cylinders, ($r_1/r_2 \approx 0.9$) (Figure 7.2.1), no correction factor needs to be applied to the stress intensity factor derived for semi-elliptic cracks in plate of infinite surface dimensions.

The first analysis of the stress intensity factor distribution around an elliptic crack embedded in a plate of infinite depth and surface dimension was done by Irwin (59). The solution is:

$$K_1 = \frac{\sigma_a \sqrt{\pi a}}{E(k)} \left(\sin^2 \theta + \frac{a^2}{c^2} \cdot \cos^2 \theta \right) \quad 8.2$$

where σ_a is the applied tensile stress and $E(k)$ is the elliptic integral of the second kind, given by

$$E(k) = \int_0^{\pi/2} \left(1 - \frac{c^2 - a^2}{c^2} \cdot \sin^2 \theta \right)^{1/2} d\theta \quad 8.3$$

where a and c are defined in Figure 7.2.1.

It turns out that K_1 varies along the crack front. At the end

of the minor axis ($\theta = \pi/2$) the stress intensity factor is the largest. At the end of the major axis ($\theta = 0$) it is the lowest.

Values of $E(k)$ can be obtained from standard tables, but the following approximation (58) is convenient:

$$E(k) = (1 + 1.48 \cdot (a/c)^{1.64})^{0.5} \quad 8.4$$

For a semi-elliptic crack in a semi-infinite plate, a front correction factor is necessary which is multiplied by the value of the stress intensity factor given by equation 8.2. An equation to calculate the front face correction factor as a function of the crack shape for the deepest point ($\theta = \pi/2$) of a semi-elliptic crack has been proposed by Shah and Kobayashi (60), however the expression presented by Scott and Thorpe (58) is more convenient for our application.

$$M_f(\pi/2) = 1.13 - 0.07 \cdot (a/c)^{0.5} \quad 8.5$$

Hence,

$$K_I(\pi/2) = M_f(\pi/2) \cdot \frac{\sigma_a \sqrt{\pi a}}{E(k)} \quad 8.6$$

8.7.2 Finite Thickness Correction

Newman (61) has proposed a formula to account for the modification of the stress intensity factor as a function of the crack depth to thickness ratio (a/t), for the uniform tension case, as follows

$$K_1 = + (M_f + (E(k) \sqrt{c/a} - M_f) \cdot (a/t)^p) \cdot \frac{\sigma_m \sqrt{\pi a}}{E(k)} \quad 8.7$$

The value of the parameter "p" that determines how the stress intensity factor varies with the fractional crack depth, a/t, is given by the results of Raju and Newman (62),

$$p(\pi/2) = 1.6 + 3 \cdot (a/c)^3 + 8 \cdot (a/c) \cdot (a/t)^5 + 0.008 \cdot (c/a) \quad 8.8$$

8.7.3 Time-to-Failure Calculations

Taking equation 8.1 as valid, the time to propagate an initial crack of size a_0 to a critical size a_c (time-to-failure) is given by

$$t_f = \int_{a_0}^{a_c} \frac{da}{da/dt} \quad 8.9$$

For finite crack increments, Δa , the expression for t_f becomes

$$t_f = \sum \frac{(\Delta a)}{A \cdot K_i^n} \quad 8.10$$

Appendix E presents a BASIC program ("TAIL") that has been developed to calculate the time-to-failure, t_f , using the expression above.

The critical crack, a_c , is assumed to be the crack depth value at which the net section stress exceeds the ultimate stress of the material. The value of a_c depends upon the applied stress, σ_a ,

such that

$$a_c = t \cdot \frac{(\sigma_u - \sigma_a)}{\sigma_u} \quad 8.11$$

where σ_u is the rupture strength of the tubing and t is its thickness. This is the failure criterion adopted in TAIL.

Implicit in the failure expression for t_f is the assumption that the total time-to-failure is taken up in crack propagation, without any prior incubation period (30).

The life of a cracked Zircaloy tubing from supplier B ($\sigma_u \approx 68$ ksi) at 320°C in iodine vapor, can be calculated as follows, as an application of the method.

The rate constant, A , and the exponent n are obtained from the previous results with DCB specimens. For the NL orientation of plate 9912-SR, when the growth rate vs. K data are replotted on a log-log scale (Figure 8.3), the Regime I crack growth may be described by a power law relation, namely

$$da/dt = (1.709 \cdot 10^{-9}) \cdot K^{4.826}$$

for K_I values less than ~ 8 ksi/in. The velocity is given in in/min.

The results of the time-to-failure calculations for three different crack aspect ratios ($a/2c$) of two initial crack sizes a_0 , are shown in Figures 8.4 and 8.5.

The data for smooth tubing is taken from the work by Knorr and Pelloux (66). As can be observed from these figures, the time-to-failure is very sensitive to variations in the aspect ratio of

the crack. Our experimental data for supplier B tubing is shown on the same figures. In addition, it is evident that I-SCC failures are possible at stresses well below the threshold stress measured on smooth specimens.

Therefore, with this type of analysis it is possible to get an idea of the time spent in crack initiation assuming that the growth rate for the DCB specimens is adequate to describe the growth of an elliptic crack in cladding.

Now, if the data for recrystallized zircaloy is plotted in the same way (log-log plot) again two linear stages for crack growth can be seen (Figure 8.6). For the low-K regime, a least-squares fit gives the following equation

$$da/dt = (3.298 \times 10^{-18}) \cdot K^{12.918}$$

for K_I values less than ~ 10 KsiVin. The velocity is given in in/min.

The exponent n is higher than that for cold worked stress relieved zircaloy. The value of n has a large effect on time-to-failure calculations.

If this procedure is repeated for the other DCB specimens tested at 310°C it is concluded that n varies from 3 to 6 for stress relieved materials.

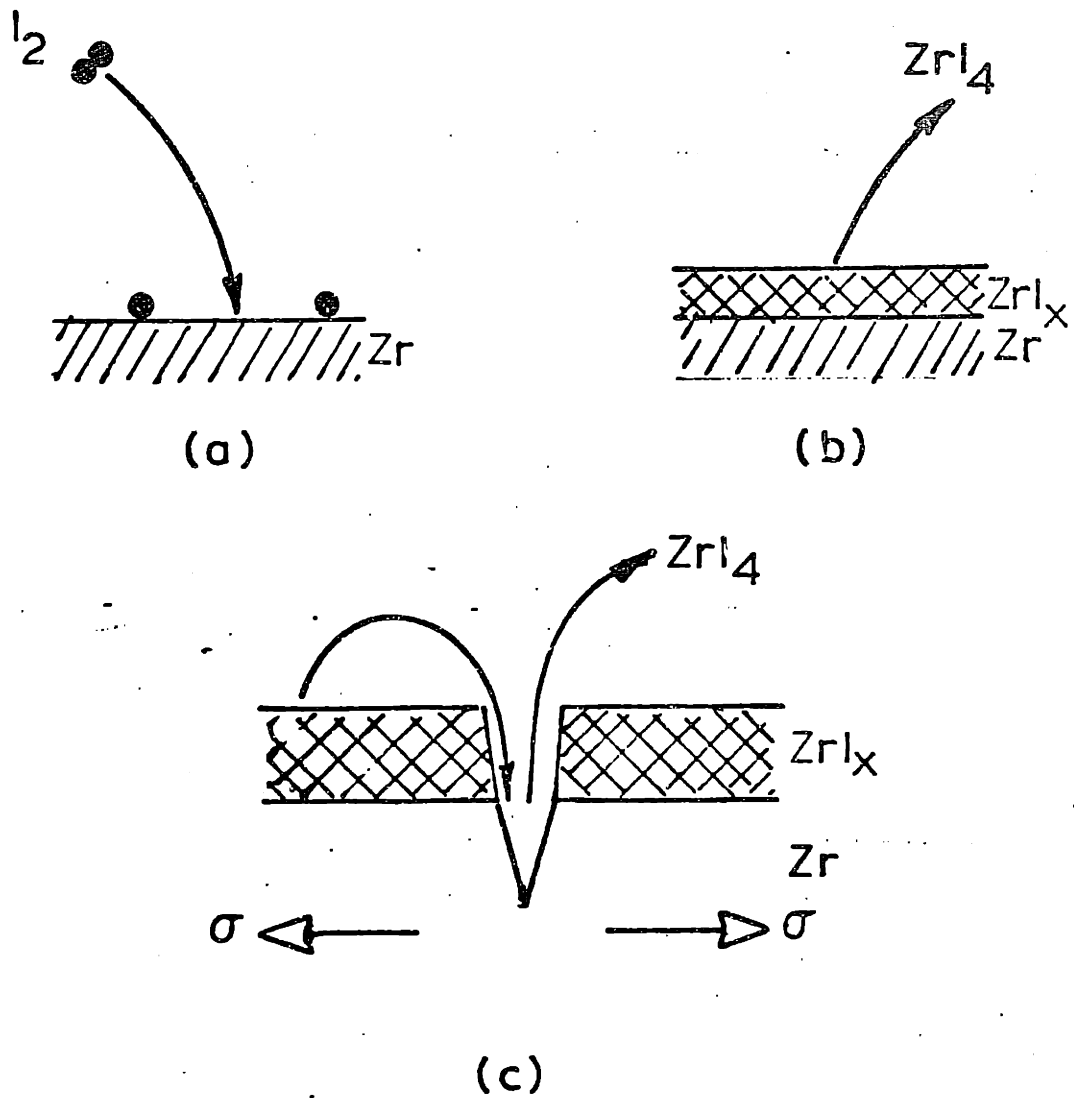


Figure 8.1 Adsorption of iodine on zirconium

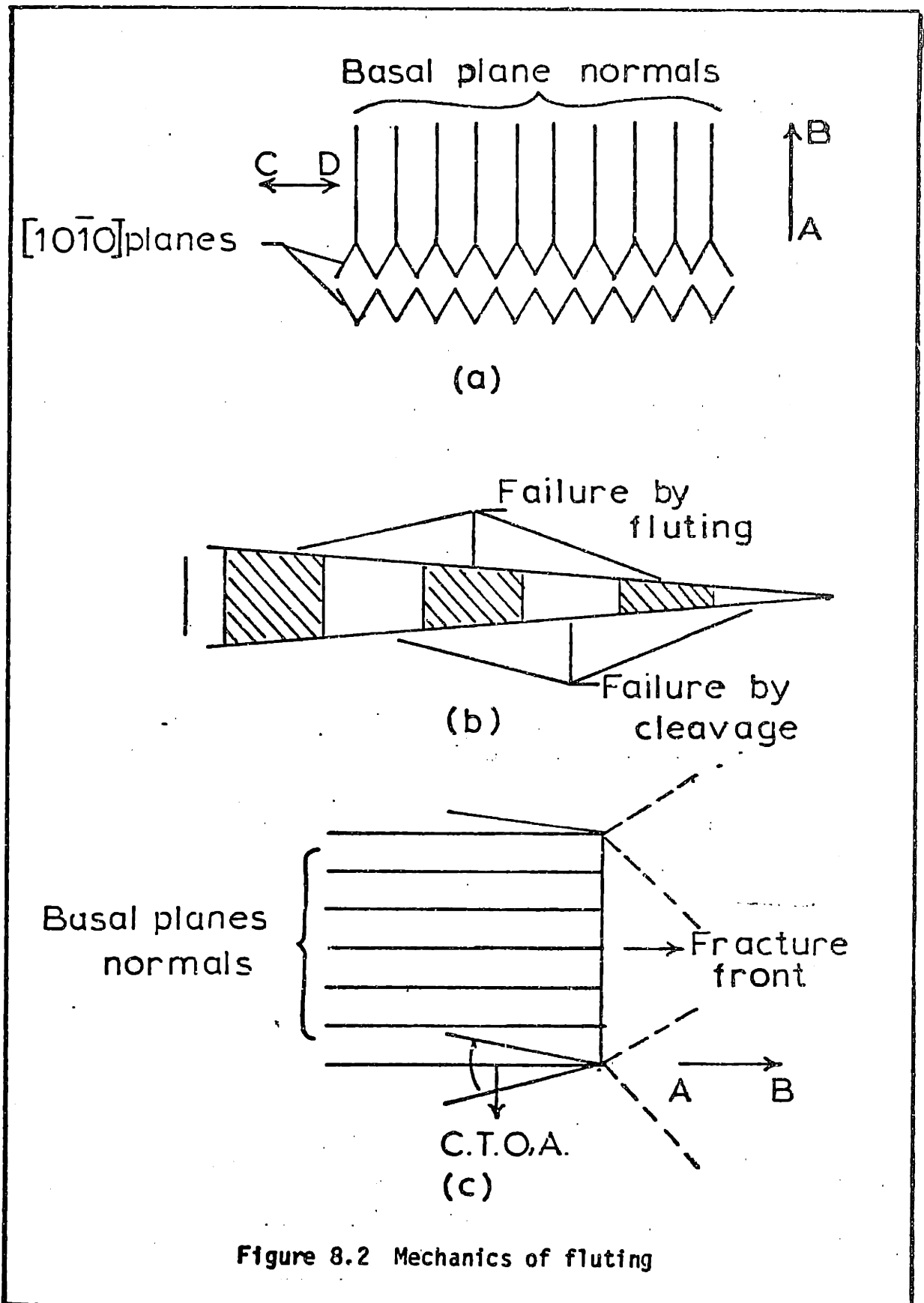


Figure 8.2 Mechanics of fluting

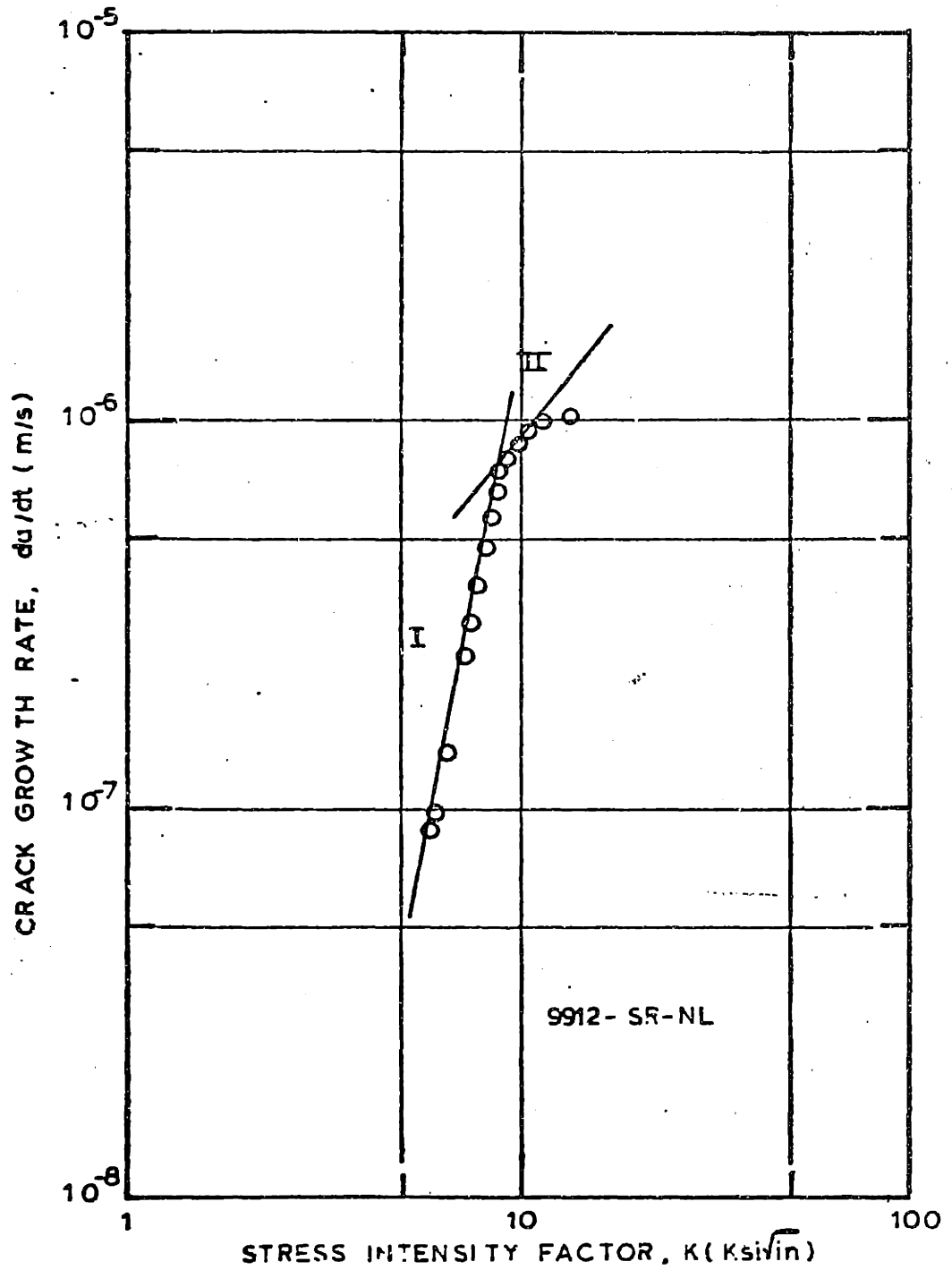


Figure 8.3 Log-log plot of I-SCC growth rate for Zircaloy plate 9912-SR

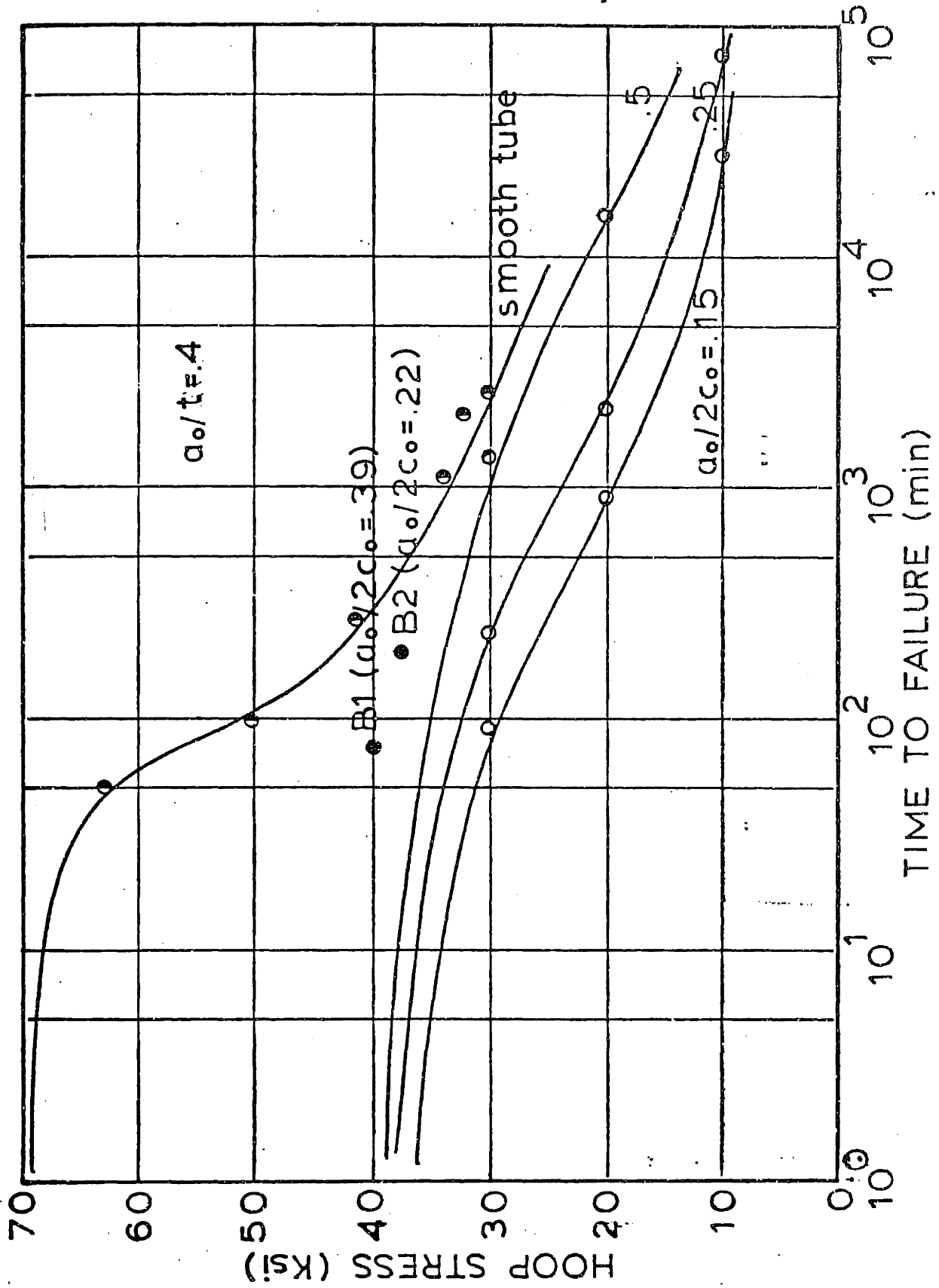


Figure 8.4 Time-to-failure vs hoop stress Zircaloy plate 9912-SR, $a_0/t = .3$

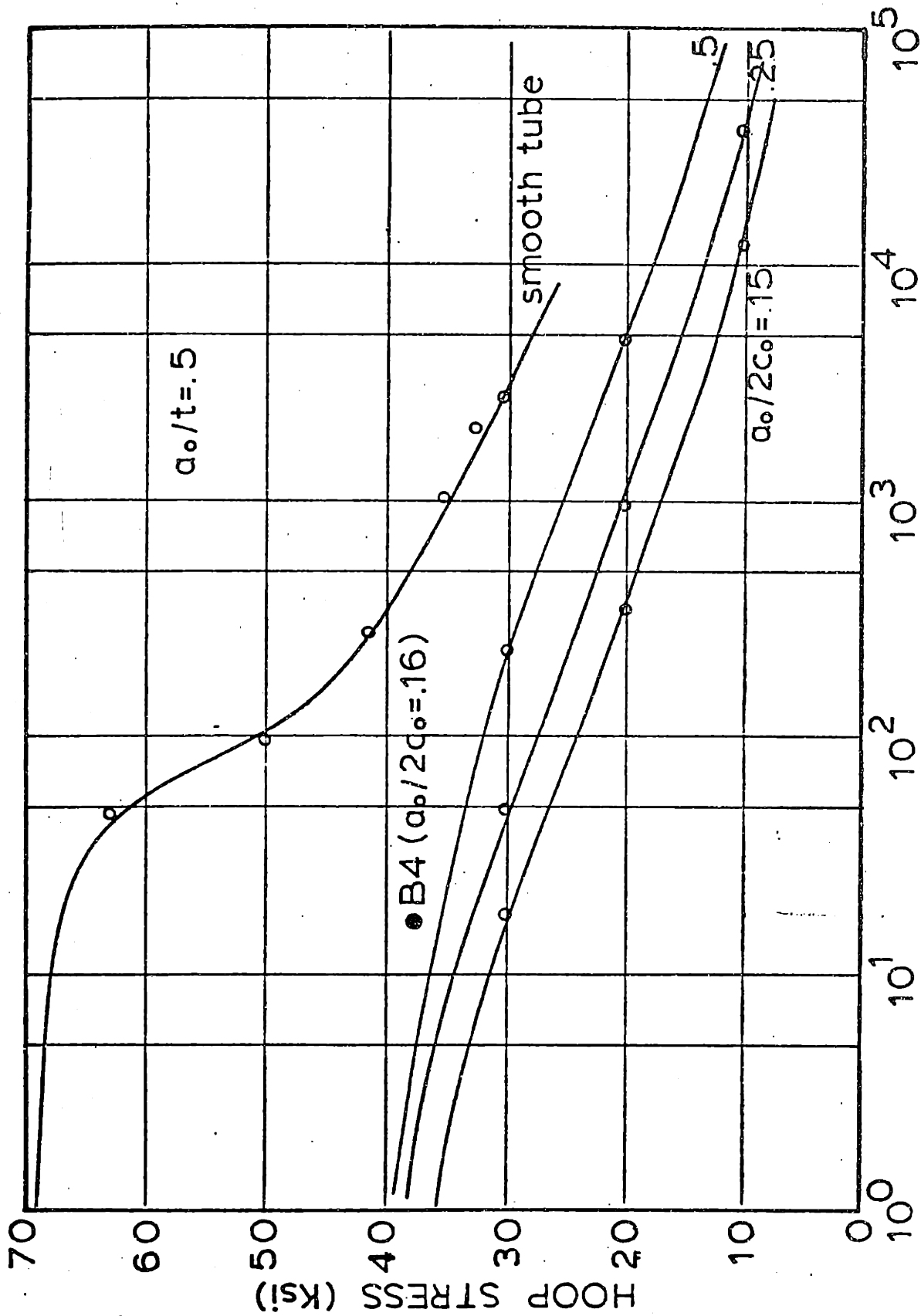


Figure 8.5 Time-to-failure vs hoop stress Zircaloy plate 9912-SR,

$a_0/t = .5$

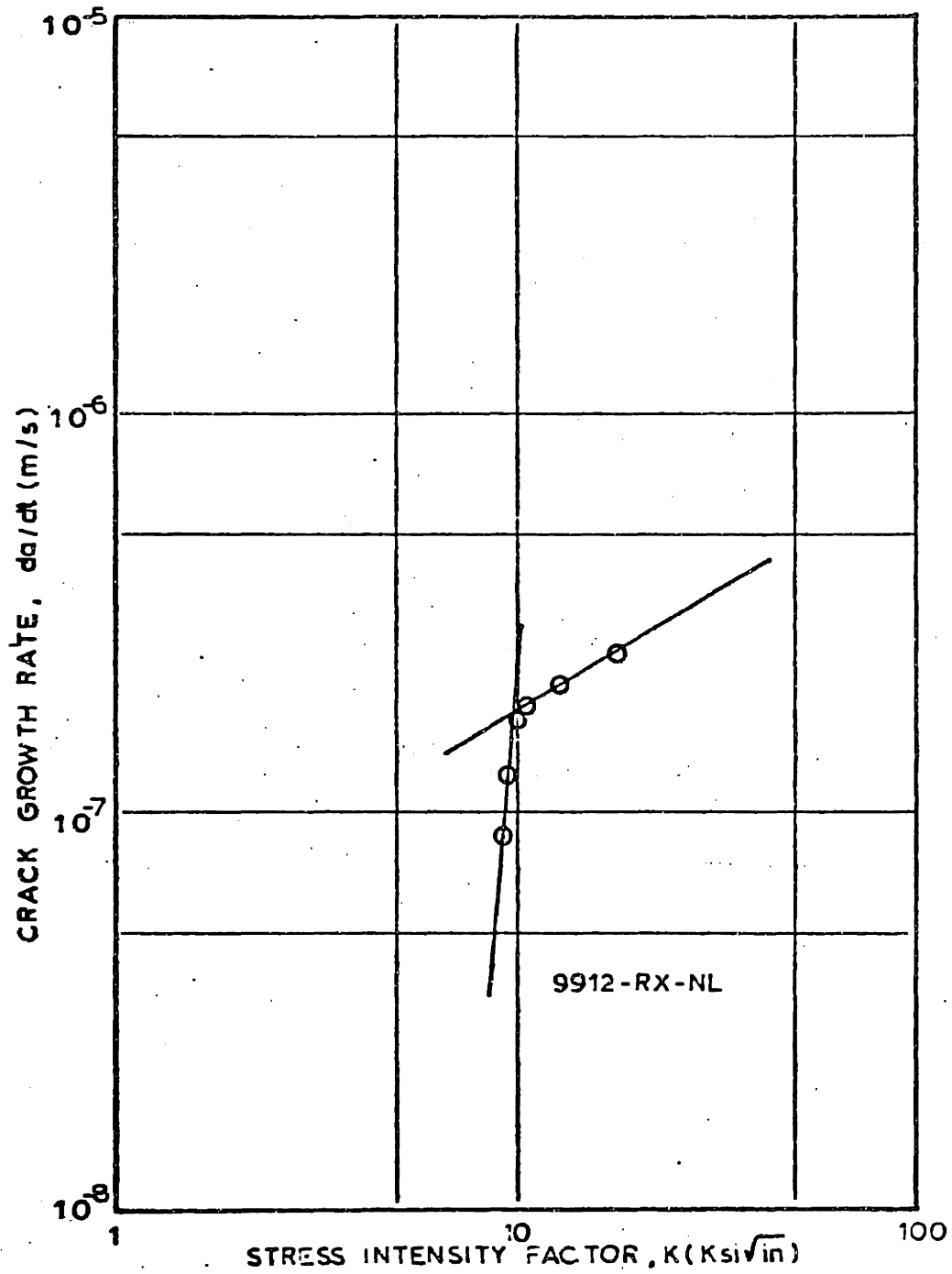


Figure 8.6 Log-log plot of I-SCC growth rate for Zircaloy plate 9912-RX

9. SUMMARY AND CONCLUSIONS

The kinetics of iodine-induced stress corrosion crack growth of unirradiated Zircaloy plate has been investigated using a fracture mechanics approach with double cantilever beam (DCB) specimens. The testing variables have been crystallographic texture (f-number), microstructure (effect of the directionality introduced by rolling), heat treatment (cold worked stress relieved vs recrystallized Zircaloy), and temperature. The iodine partial pressure is 40Pa. The data obtained lead to the following conclusions and observations:

(1) The crystallographic texture, as expressed by the Kearns' f-number has a large influence on the crack growth rate. For tests at 310°C the growth rate increases with increasing f-number.

(2) Microstructural directionality also affects the crack growth rate. Crack propagation is faster in the rolling direction.

(3) In general, two crack growth rate regimes are observed. A low-K regime where da/dt varies strongly with K and a high-K regime where this dependence is not so strong. Both regimes can be fitted to a power law type relation ($da/dt = A \cdot K^n$). Values of n are in the range 3 to 6 for CWSR Zircaloy and is about 13 for recrystallized Zircaloy for the low-K regime.

(4) Recrystallized Zircaloy shows I-SCC growth rates lower than the stress relieved material in the whole range of K. Regions of intergranular cracking are observed at values of K near the threshold. They are indicative of low crack growth rates.

(5) The crack growth rate decreases with decreasing test

temperature. An apparent activation energy for crack growth of 2.9 kcal/mole is determined for the 9912-SR Zircaloy plate.

(6) Transgranular cleavage near the basal plane is the principal mode of crack propagation but as the temperature is decreased the contribution of ductile processes like fluting are enhanced.

To test the validity of the fracture mechanics approach, experiments with fatigue precracked Zircaloy cladding specimens are done. The specimens are internally pressurized in the presence of iodine (0.2mg/cm^2) at 320°C . Time-to-failure under constant stress conditions are measured and compared with calculations using power law relationships from the DCB experiments. The correlation is good for the crack sizes tested (long cracks). The crack geometry (aspect ratio) is an important parameter in the analysis.

10. SUGGESTIONS FOR FUTURE WORK

Some ideas for further research are:

- To study the difference between long and short crack growth behavior using Zircaloy cladding specimens fatigue precracked and establish the upper and lower limits of the analysis. The application of elastic-plastic fracture mechanics to short crack situations needs to be verified.

- To investigate the existence of an "incubation" period to crack growth in Zircaloy cladding as proposed by Peehs et al. (30). The use of precracked specimens is recommended.

- To analyze the behavior of multiple-crack propagation in cladding material as opposed to the single-crack behavior of this study; interconnection of cracks has to be considered.

- To correlate the temperature dependence of the crack growth rate with some thermally-activated physical or chemical phenomenon such as adsorption of iodine on zirconium, for instance.

- To correlate the I-SCC crack growth behavior with the corrosion-fatigue crack growth under iodine vapor and to study the effect of crystallographic texture.

APPENDIX A

The KEARNS' f-PARAMETER

The Kearns' f-parameter (9) was originally conceived as a single-number quantity from which physical properties in polycrystalline material could be calculated from single-crystal values. In order to make calculations of this kind meaningful in polycrystalline material, it is necessary to assume that the bulk property in a reference direction is the weighted summation of this property in the individual crystals.

In an analogous manner, the concept of an f-parameter can be used as a quantitative index of the effective texture, where the single f-number represents the effective fraction of basal poles aligned in any one reference direction.

For hexagonal single-crystals, the magnitude of certain properties $P(\phi)$ relating two vector quantities or a tensor with a scalar quantity is given by (63):

$$P(\phi)_{\text{ref}} = P_c \cos^2 \phi + P_a (1 - \cos^2 \phi),$$

where $P(\phi)_{\text{ref}}$ is the property in the reference direction, P_a and P_c are the single crystal values normal and parallel to (0002), and ϕ is the angle between the reference direction and (0002).

If the grains of a certain orientation in a polycrystalline material are assumed to contribute to a bulk property in proportion to their volume fraction, V_i , then for crystals oriented with their

c-axis at a tilt angle ϕ_i to the reference direction their contribution to the bulk property can be written as:

$$P(\phi_i)_{\text{ref}} = P_c \cdot V_i \cdot \cos^2 \phi_i + P_a \cdot V_i \cdot (1 - \cos^2 \phi_i)$$

and summing over the total volume,

$$P_{\text{ref}} = P_c \sum_i V_i \cdot \cos^2 \phi_i + P_a \sum_i V_i \cdot (1 - \cos^2 \phi_i)$$

which becomes $P_{\text{ref}} = f \cdot P_c + (1 - f) \cdot P_a$ since $\sum_i V_i = 1$ and the summation $\sum_i V_i \cdot \cos^2 \phi_i$ is defined as the orientation parameter, f .

In order to calculate an f -number from the equation above, it is necessary to calculate V_i as a function of ϕ . This may be done by considering a reference sphere intersected by the (0002) poles of a random sample, and evaluating the volume of metal as a series of $\Delta\phi$ bands from $\phi = 0$ to $\phi = 90$ degrees. The volume of metal in each $\Delta\phi$ band is proportional to the number of poles in the band, which is equal to the average pole density, $I(\phi)$, times the size of the band. The size of the band is proportional to its circumference on the reference sphere which, in turn, is proportional to $\sin \phi$. Since the volume of metal in each $\Delta\phi$ band is proportional to $I(\phi) \cdot (\sin \phi) \cdot (\Delta\phi)$, the volume fraction in each band may be expressed as follows:

$$V_{\Delta\phi} = \frac{\int_{\phi_1}^{\phi_2} I(\phi) \cdot \sin \phi \cdot d\phi}{\int_0^{\pi/2} I(\phi) \cdot \sin \phi \cdot d\phi}$$

where the integral in the denominator represents the total number of basal (0002) poles in a unit volume of the sample.

When the average basal pole density in any $\Delta\phi$ band, $I(\phi)$, is expressed as a fraction of the basal pole density in the same $\Delta\phi$ band of a random specimen, this integral equals unity. The expression for f may now be put in an integral form as

$$f = \int_0^{\pi/2} I(\phi) \cdot \sin \phi \cdot \cos^2 \phi \cdot d\phi$$

The f -number defined above may take on values from 0 to 1. An f -number of 0 indicates perfect alignment of the basal poles in a direction normal to the reference direction. An f -number of 1 indicates alignment of all basal poles parallel to the reference direction. An f -number of $1/3$ in each of the three principal directions defines the isotropic case (randomly oriented specimen), and the sum of the f -numbers in these directions is theoretically equal to unity, irrespective of the anisotropy in any one direction.

APPENDIX B

BASIC CONCEPTS IN LINEAR ELASTIC FRACTURE MECHANICS

While the initial work in fracture mechanics was based upon an energy balance criterion, later work has identified alternate fracture parameters principally, the stress intensity factor, the crack opening displacement, and the J-integral parameter. For elastic materials, these are all interrelated. Specifically, for plane strain LEFM in the "opening" mode)

$$G = J = [(1 - \nu^2)/E] \cdot K^2 = Y \cdot \delta \quad (B.1)$$

where G is the strain energy release rate, J is the value of the J-integral, K is the stress intensity factor, and δ is the crack tip opening displacement, while E, ν , and Y are, as usual, the elastic modulus, Poisson's ratio, and yield stress, respectively (33).

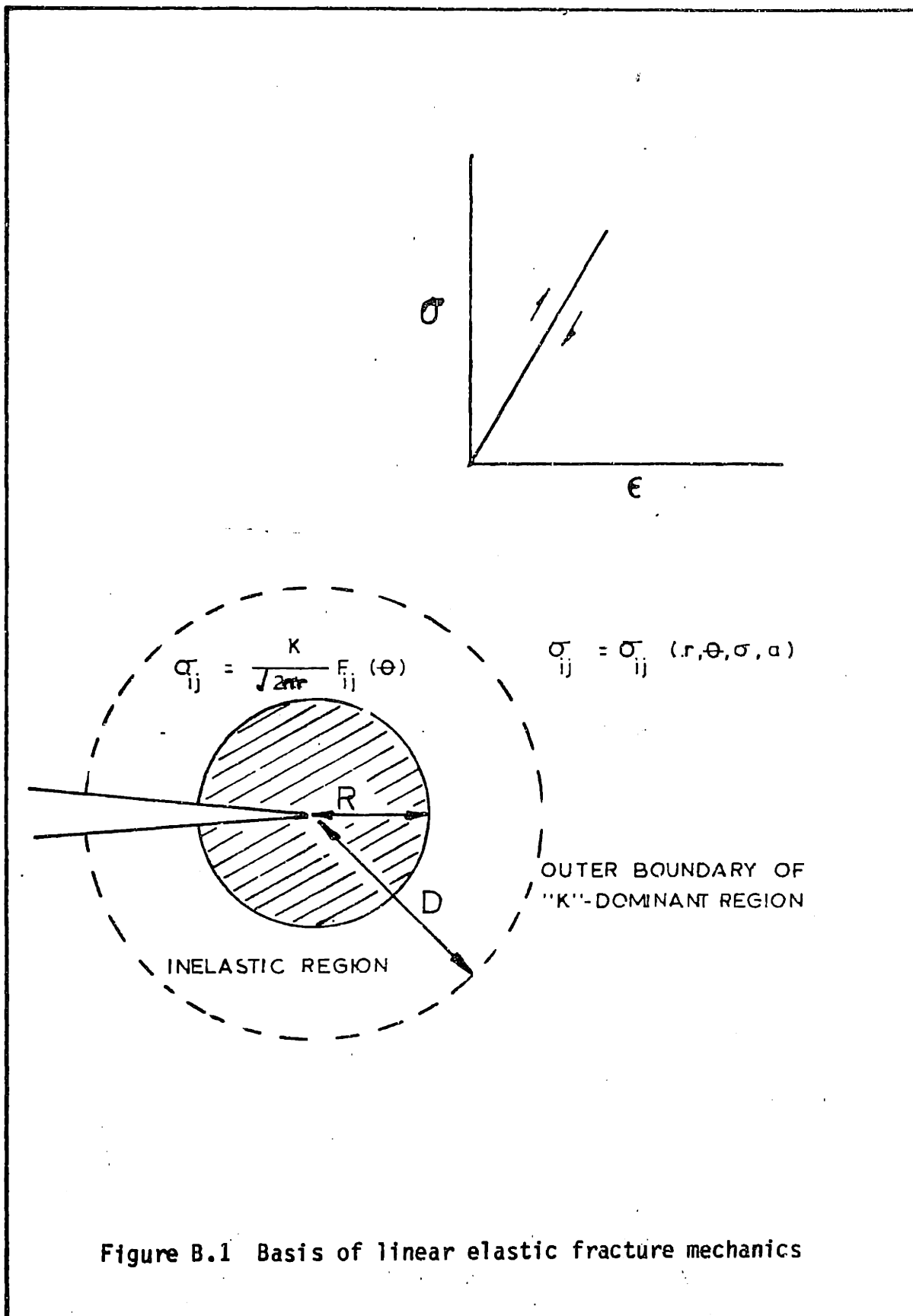
The modern view of LEFM is contained in Figure B.1. It can be shown that, if a body obeys everywhere a linear elastic stress-strain law (see insert in Figure B.1), then the stresses at the crack tip can always be expressed in terms of a polar coordinate (r, θ) system with origin at the crack tip as

$$\sigma_{ij} = [K/2\pi r] F_{ij}(\theta) + \dots \quad (B.2)$$

where the omitted terms are of higher order in r . For small values of r (i.e., very near the crack tip), only the first term is significant. Then, the remote stresses, the crack length, and the

external dimensions of the cracked body will affect the stresses at the crack tip only through the parameter K , the stress intensity factor. More definitely, there will be a region--the "K-dominant" region having the characteristic dimension D in which the first term of the series is a sufficiently good approximation ("small-scale yielding approximation").

To continue this argument, let R denote the size of the inelastic region surrounding the crack tip where the process of void initiation, growth, and coalescence that constitute ductile fracture is occurring. In this region, of course, the assumption of linear elastic behavior is invalid. It is not possible, therefore, to characterize directly the fracture process using a linear elastic formulation. However, this is not necessary, provided the inelastic region is contained in the K-dominant region. That is, if $R < D$, it can be argued that any event occurring within the inelastic region is controlled by the deformation in the surrounding K-dominant region. Consequently, if crack growth occurs, it must do so at a critical value of the stress intensity factor (34).



APPENDIX C

FATIGUE CRACK GROWTH RATE MEASUREMENTS

FCGR tests were conducted to determine the fatigue crack growth behavior of Zircaloy plate in order to establish the stress intensity factor range value for precracking the DBC specimens for I-SCC tests.

The material used was a Zircaloy-2 plate, 0.10 in (2.54 mm) thickness. The cold-worked plate had been stress relieved at 485°C for 5 hours. Its hardness was 97 Rockwell B. The basal pole figure at the mid-thickness of the plate is shown in Figure C.1.

The specimen design was the single-edge-notch (SEN) configuration. The crack-starter notches were nominally 0.4 in long, and were introduced by a combination of a band saw cut (0.25 in wide) with a 0.006 in wide string saw cut.

The specimens were polished on one side to facilitate crack length measurements. First, the specimens were hand ground down to 600 grit SiC paper, then a section 1/4" on either side of the notch and extending across the width of the specimen was polished with 14 μm and 3 μm diamond paste using a felt wheel and a Dremel Moto Tool.

The specimens were fatigue cycled in uniaxial tension at 10 Hertz (cycles/sec) on a MTS hydraulic machine with R value (P_{\min}/P_{\max}) of 0.05. The specimens were tested at room temperature (25°C) in air.

The crack lengths were measured optically with a Gaertner traveling microscope accurate to 0.01 mm. The crack growth rate was calculated by the equation

$$da/dN = (a_f - a_i)/N$$

where a_f is the final crack length

a_i is the initial crack length

N is the number of cycles.

The stress intensity factor was calculated by the formula (64):

$$K = (P/B \cdot w) \cdot a^{1/2} \cdot (1.986 + 1.782(a/w) + 6.998(a/w)^2 - 21.505(a/w)^3 + 45.351(a/w)^4)$$

where P is the load

B is the specimen thickness

w is the specimen width

$a = (a_f + a_i)/2 =$ average crack length.

The bracketed term represents the correction for the finite width of the test specimen. This expression is valid for a/w less than 0.635.

Specimens were tested with load applied in both the transfers (TL orientation), and rolling (LT orientation) directions. Figure C.2 shows the results obtained. Least-squares regression techniques were applied to the data with the following results

$$da/dN = 8.09 \times 10^{-16} \cdot (\Delta K)^{2.38}$$

for $\Delta K < 20 \text{ Ksi}\sqrt{\text{in}}$

LT orientation

$$da/dN = 3.13 \times 10^{-22} \cdot (\Delta K)^{3.90}$$

for $\Delta K > 20 \text{ Ksi}\sqrt{\text{in}}$

$$da/dN = 1.98 \times 10^{-16} \cdot (\Delta K)^{2.53}$$

for $\Delta K < 20 \text{ Ksi}\sqrt{\text{in}}$

TL orientation

$$da/dN = 7.19 \times 10^{-21} \cdot (\Delta K)^{3.57}$$

for $\Delta K > 20 \text{ Ksi}\sqrt{\text{in}}$

The curves show a transition in the crack growth rate. The effect of the plate orientation appears to be small.

Scanning electron micrographs of the fracture surfaces are shown in Figure C.3. The crack growth direction is from bottom to top.

137

L

90°

60°

30°

T

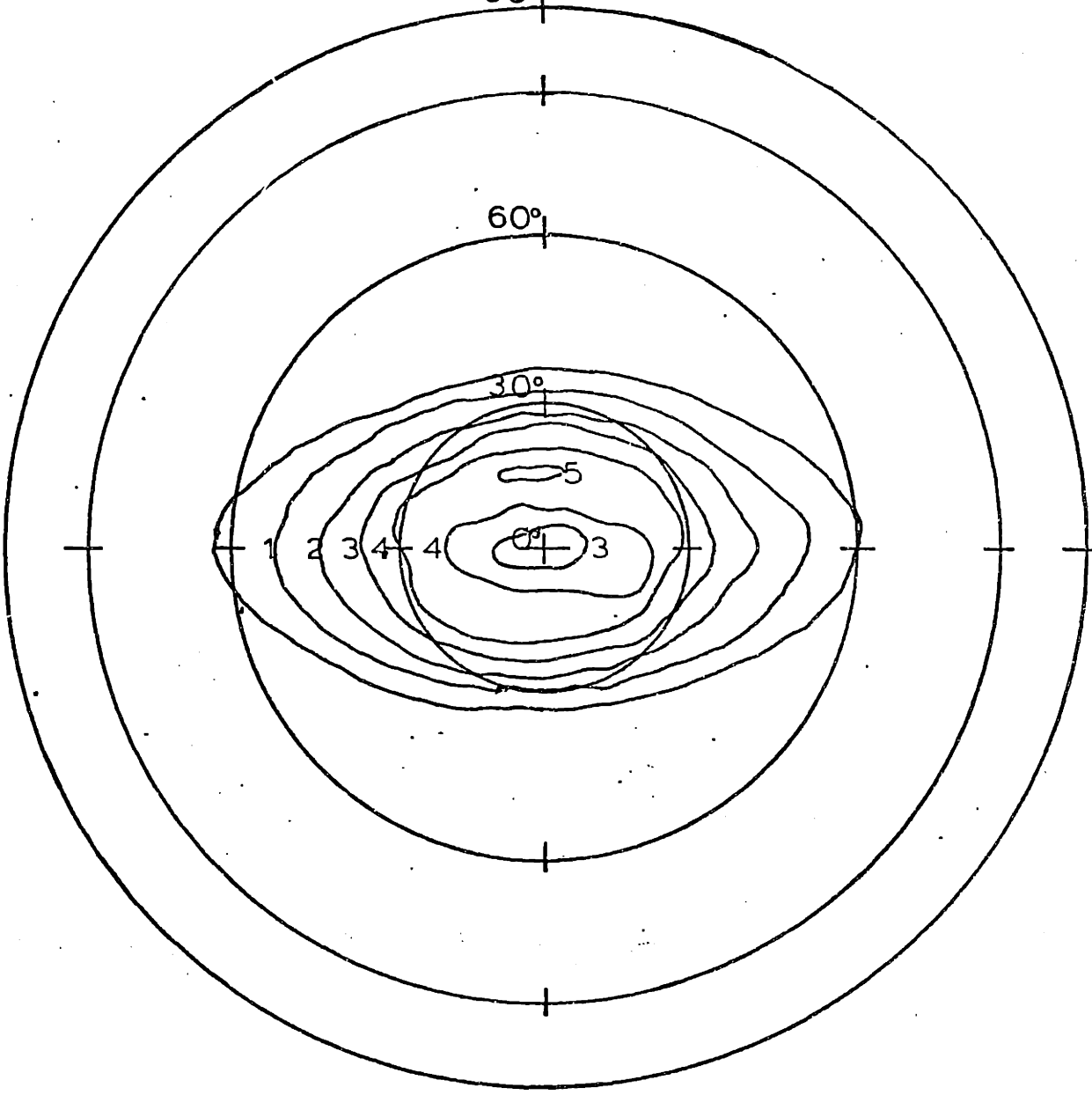
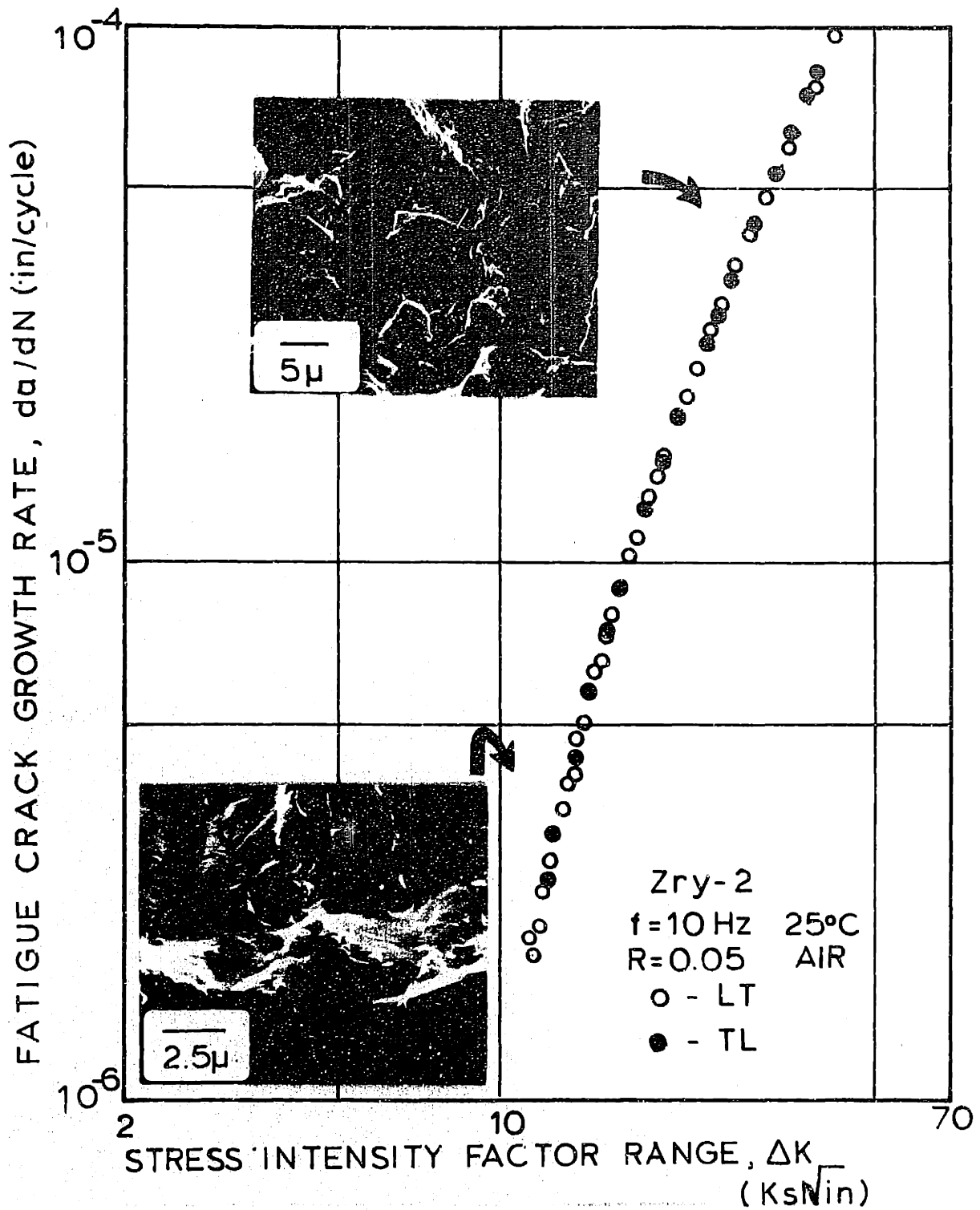
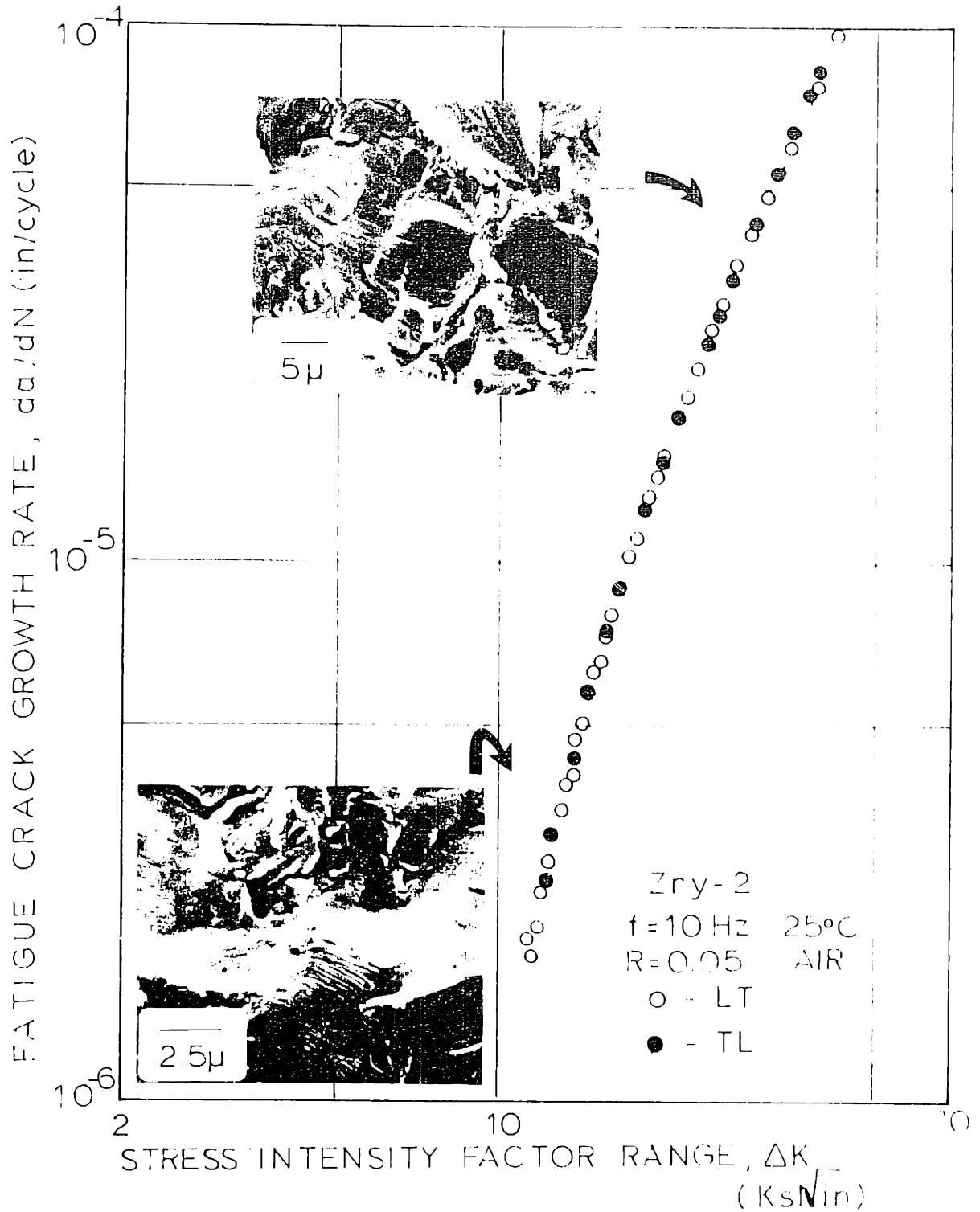
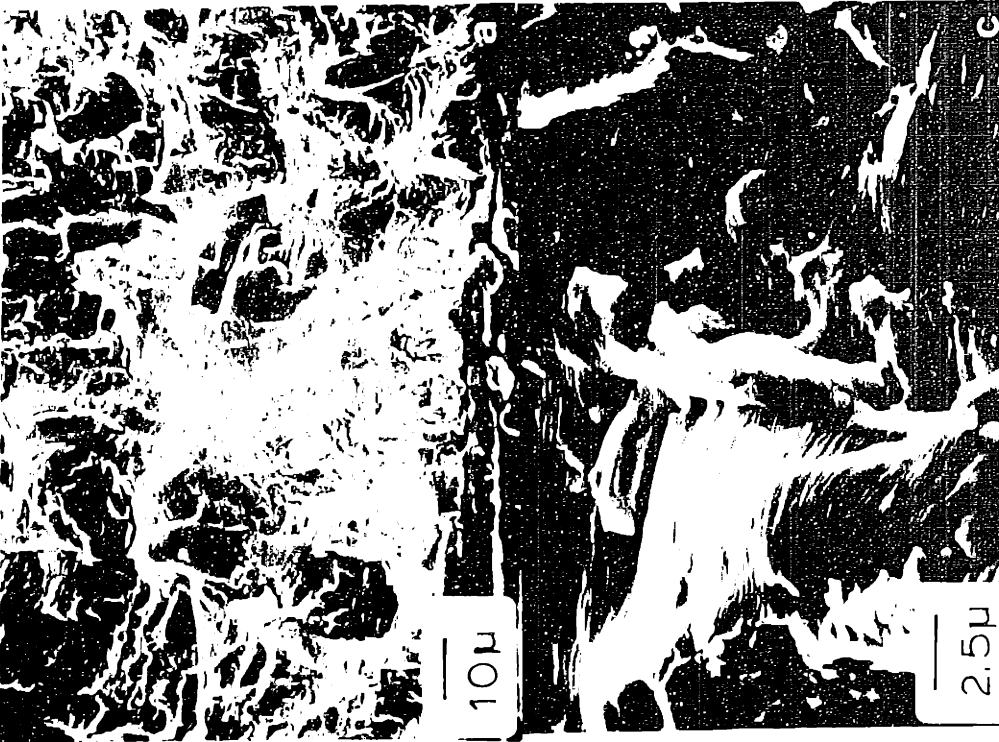
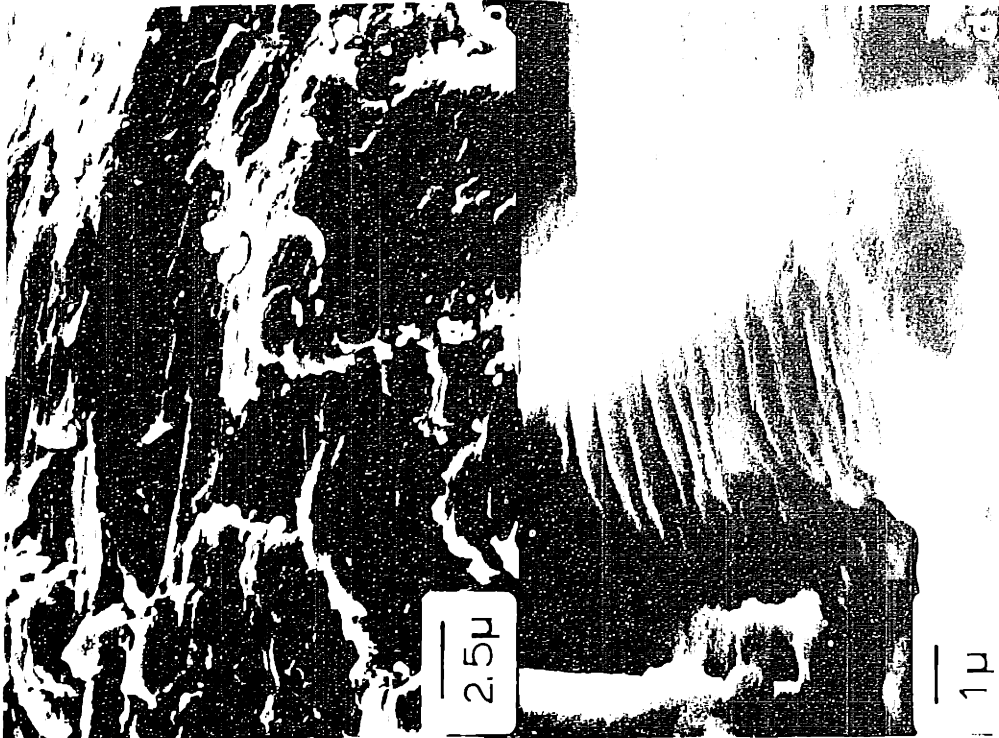


Figure C.1 Basal pole figure

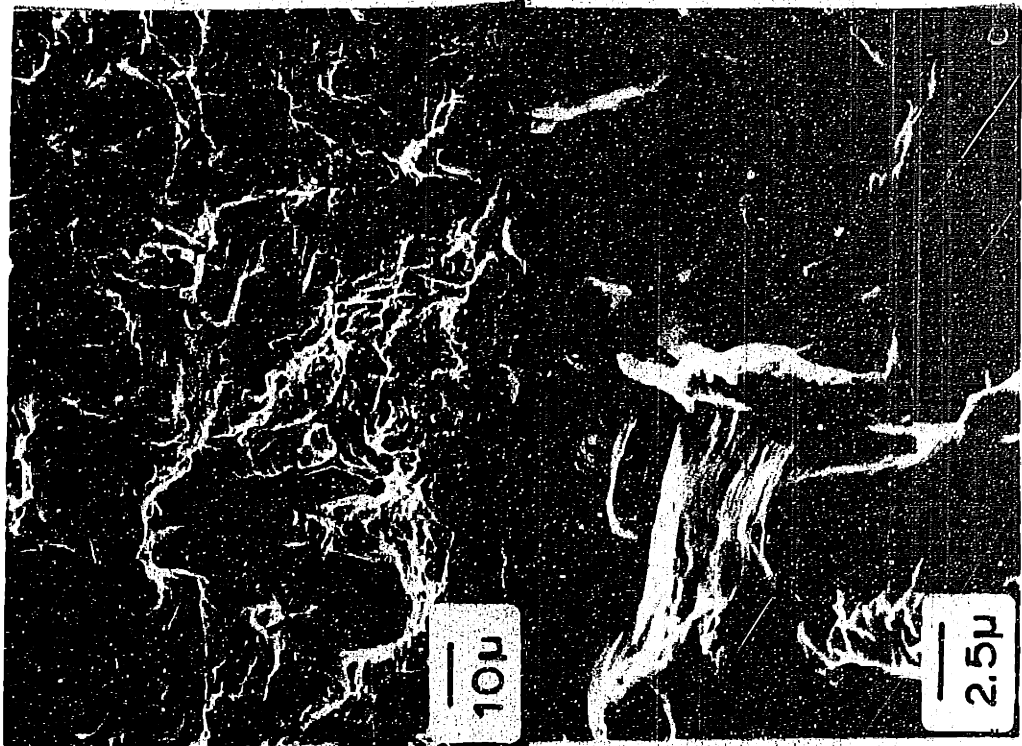
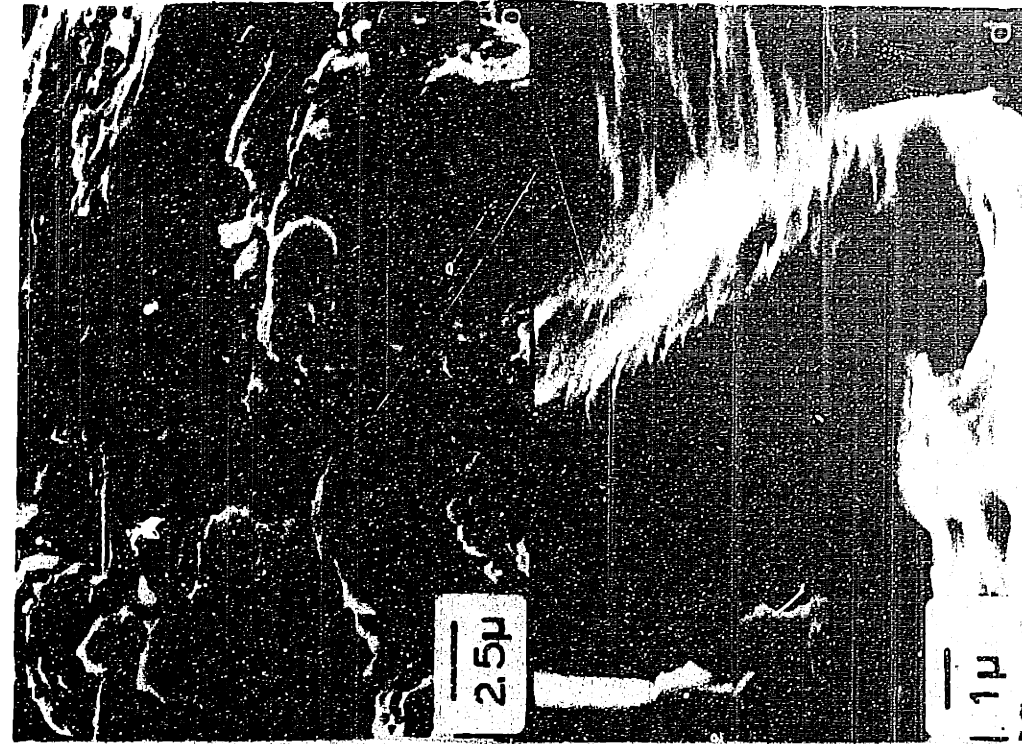


C.2 Fatigue crack propagation behavior of CWSR Zircaloy-2 plate cycled in air at 25°C.





C.3 Scanning electron micrographs of fracture surface of Zircaloy-2 plate fatigued in air at 25°C (a) Region near the crack starter, (b) Detail at $K = 12 \text{ Ksi}\sqrt{\text{in}}$, (c) Detail at $K = 30 \text{ Ksi}\sqrt{\text{in}}$ (d) Fatigue striations. Crack path from bottom to top.



C.3 Scanning electron micrographs of fracture surface of Zircaloy-2 plate fatigued in air at 25°C (a) Region near the crack starter, (b) Detail at $K = 12 \text{ Ksi}\sqrt{\text{in}}$, (c) Detail at $K = 30 \text{ Ksi}\sqrt{\text{in}}$ (d) Fatigue striations. Crack path from bottom to top.

APPENDIX D

STRESS ANALYSIS OF FATIGUE PRECRACKING OF TUBES (43)

Under a compressive load, a ring element with a rectangular section becomes oval, and the decrease in its diameter, δ , is a linear function of the applied load, P (), according to the relation:

$$\delta = \left(\frac{\pi}{4} - \frac{2}{\pi}\right) \cdot 12 \cdot P \cdot R^3/E \cdot e^3 \cdot l \quad (D.1)$$

where R is the Young's modulus of the material

R is the average radius of the ring element

e is the thickness of the ring element

l is the length of the ring element.

In our experiments, each element of length dl of the upper plate is subjected to a load dP proportional to the local deformation, δ , of the ring element that is under this plate element. The deformation of the upper plate then, is similar to the deflection of a finite length beam on an elastic foundation submitted to a single load at its middle section. Its deformation is the solution of the differential equation (65):

$$(E' \cdot b \cdot h^3/12) \cdot d^4y/dx^4 = -Ky \quad (D.2)$$

where E' is the Young's modulus of the plate

h is the thickness of the plate

b is the length of the plate

K is a constant usually called the modulus of the foundation

per unit of length. It is given by the relation (65):

$$K = (P/\delta \cdot l) = (E \cdot e^3/12R^3) \cdot (\frac{\pi}{4} - \frac{2}{\pi})$$

For the boundary conditions imposed (no traction between the tube and the plate) the solution of (2) is:

$$y = Z \cdot \cos \beta x \cdot \operatorname{ch} \beta x \quad (D.3)$$

with $\beta = (3K/E' \cdot h^3 \cdot b)^{1/4}$

and $Z = (P \cdot \beta/2K) \cdot \frac{1 - \operatorname{ch} \pi}{\operatorname{sh} \pi} \quad (D.4)$

The length L , over which the deformation of the tube is distributed is given by:

$$L = \pi/\beta$$

In practice, L is approximately a liner function of the plate height. Hence, we have a simple method of changing the size of the loading region and therefore the crack length.

The induced stresses in the tube are dependent on the deflection δ and the angular position ϕ . In the inside surface, the tangential stress is given by

$$\sigma_t = \frac{Z \cdot E \cdot e \cdot (\cos \phi - \frac{2}{\pi})}{4(\frac{\pi}{4} - \frac{2}{\pi}) \cdot (1 - \nu^2) \cdot R^2}$$

This gives a maximum value for the traction stresses in the inside surface, in the region right below the point of application of the

load:

$$\sigma_{\max} = \frac{(\pi - 2) \cdot Z \cdot E \cdot e}{(\pi^2 - 8) \cdot (1 - \nu^2) \cdot R^2}$$

By varying the loading with time in a fatigue machine, a crack is induced in this region whereas the initiation and propagation can be monitored by the mechanical response of the system, that is, the change in compliance.

APPENDIX E

THE TAIL COMPUTER PROGRAM

The TAIL program (in BASIC) calculates the time-to-failure of precracked Zircaloy tubing specimens.

The crack growth relation used in the calculations is of the power law form $da/dt = A \cdot K^n$.

Two assumptions are made in the calculation:

(1) The crack shape remains constant and the growth rate is governed by K at a single point of the crack (maximum value).

(2) The crack growth rate law parameters A and n are material constants.

The BASIC algorithm for TAIL proceeds in the following steps:

1. Computation of the critical crack depth (AC)
2. Computation of the crack step incremental (DA)
3. Computation of the elliptic integral (EK)
4. Computation of the parameter P
5. Computation of the stress intensity factor (K1)
6. Computation of the time-to-failure (t_f)

A listing of TAIL is contained in Figure E.1.

Figure E.1. Listing of TAIL

```

10 REM TIME TO FAILURE (MIN)
15 REM
20 REM AO INITIAL CRACK DEPTH (IN)
25 REM CO INITIAL CRACK HALF-LENGTH (IN)
30 REM T TUBING WALL THICKNESS (IN)
35 REM SU ULTIMATE STRENGTH (KSI)
40 REM SA APPLIED HOOP STRESS (KSI)
45 REM A RATE CONSTANT (IN/MIN/KSI**N)
50 REM N EXPONENT
55 REM D DENOMINATOR DELTA-A EXPRESSION
60 REM L LOOP PARAMETER
65 REM
70 PRINT "TIME TO FAILURE"
75 PRINT
100 READ A,N,D,L
150 DATA
200 PRINT "AO,CO,T,SU,SA"
250 INPUT AO,CO,T,SU,SA
300 AC = (1 - SA/SU)*T
400 PRINT "AC ="; AC
450 PRINT
490 REM INCREMENTAL CRACK DEPTH DA
500 DA = (T - AO)/D
550 REM
600 TF = 0
700 FOR I = 1 TO L
800 A1 = AO + I*DA
900 IF A1 - AC > 0 THEN 1400
1000 C1 = (A1/AO)*CO
1100 GOSUB 1600 'K1
1200 TF = TF + (DA/K1N)/A
1300 NEXT I
1400 PRINT "TF ="; TF
1450 PRINT
1480 PRINT "K1MAX ="; K1
1500 END
1600 REM SUBROUTINE 'K1
1700 PI = 3.1415
1800 GOSUB 3200 'P
1900 X1 = (A1/T)P
2000 GOSUB 2600 'EK
2100 X2 = EK * SQR(C1/A1)
2200 GOSUB 2900 'MF
2300 X3 = MF + (X2-MF)*X1
2400 X4 = (SA/EK)*SQR(PI*A1)
2500 K1 = X3*X4
2600 REM SUBROUTINE 'EK
2700 EK = SQR(1 + 1.47*((A1/C1)1.64)

```

Figure E.1. Listing of TAIL (continued)

```
2800 RETURN
2900 REM SUBROUTINE 'MF
3000 MF = 1.13 - 0.07*SQR(A1/C1)
3100 RETURN
3200 REM SUBROUTINE 'P
3300 P = 1.6 + 3*(A1/C1)3 + 8*(A1/C1)*(A1/T)5 + 0.008*(C1/A1)
3400 RETURN
```

APPENDIX F

POLYNOMIAL FITTING TO THE CRACK LENGTH VS. TIME DATA

Figure F.1 shows a typical plot of crack length vs. time data collected in this work.

The initial growth of the stress corrosion crack is very fast. The curve is fitted to a 3rd degree polynomial by regression analysis (least square method). For the example in case the expression found is

$$a(t) = .43 + 2.48 \times 10^{-3}t - 4.39 \times 10^{-6}t^2 + 2.81 \times 10^{-9}t^3$$

with $r^2 = .994697$

where r is the coefficient of correlation.

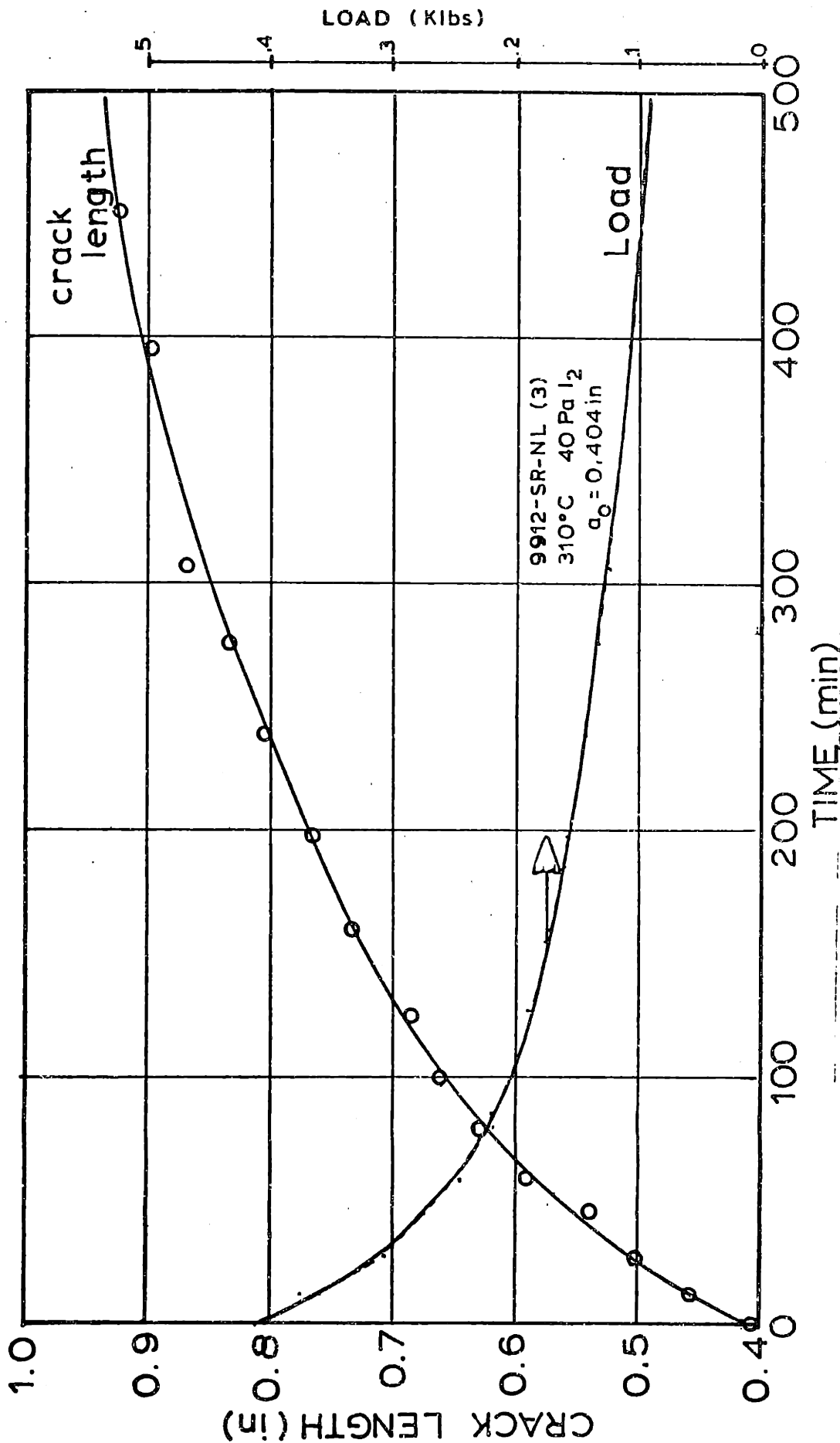


Figure F.1 Growth of iodine-induced crack in Zircaloy

BIBLIOGRAPHY

1. Roberts, J.T. Adrian
Structural Mechanics in Nuclear Power Systems
Plenum Press, New York 1981
2. Roberts, J.T.A., Jones, R.L., Cubiciotti, D., Miller, A.K.,
Wachob, H.F., Smith, E., and Yaggee, F.L.
"A Stress Corrosion Cracking Model for Pellet-Cladding
Interaction Failures in Light-Water Reactor Fuel Rods,"
Zirconium in the Nuclear Industry (Fourth Conference), ASTM STP
681, American Society for Testing and Materials 1979, pp. 285-305
3. Schemel, J.H.
ASTM Manual on Zirconium and Hafnium
ASTM STP 639, American Society for Testing and Materials 1977
4. Akthar, A.
Basal Slip in Zirconium
Acta Metallurgica 21: pp. 1-11 (1973)
5. Christian, J.W.
The Theory of Transformations in Metals and Alloys
Pergamon.
6. Ballinger, R.G.
"The Anisotropic Mechanical Behavior of Zircaloy-2,"
M.I.T. Thesis Nuclear Engineering 1977 M.S.
7. Schewbridge, J.F.
"Crystallographic Texture Control in Zircaloy Tubes"
M.I.T. Thesis Mat. Sci. and Engineering 1982 Sc.D.
8. Knorr, D.B. and Pelloux, R.M.
"Quantitative Characterization of Crystallographic Textures in
Zirconium Alloys"
Journal of Nuclear Materials 71: pp. 1-13 (1977)
9. Kearns, J.J.
"Thermal Expansion and Preferred Orientation in Zircaloy"
WAPD-TM-742 (1965).
10. McGeary, R.K. and Lustman, B.
Preferred Orientation in Zirconium
Trans. AIME, 191: pp. 944-1002(1951)
11. Jensen, J.A. and Backofen, W.A.
Deformation and Fracture of α -Zirconium Alloys
Canadian Metallurgical Quarterly, 11: pp. 39-51 (1972)

- 11a. Pettersson, K.
Studsvik Energiteknik AB (Unpublished Results)
12. Cox, B. and Wood, J.C.
"Iodine Induced Cracking of Zircaloy Fuel Cladding," in Corrosion Problems in Energy Conversion and Generation
Electrochemical Society, Princeton, N.J. (1974) pp. 275-321
13. Aitchison, I. and Cox, B.
"Interpretation of Fractographs of SCC in Hexagonal Metals"
Corrosion, 28: pp. 83-88 (1972)
14. Spurrier, J. and Scully, J.C.
"Fractographic Aspects of the Stress Corrosion Cracking of Titanium in a Metanol/HCl Mixture"
Corrosion, 28: pp. 453-463 (1972)
15. LeMay, I.
Principles of Mechanical Metallurgy
Elsevier, New York (1981) p. 253
16. Wood, J.C., Surette, B.A., London, I.M., and Baird, J.
"Environmentally Induced Fracture of Zircaloy by Iodine and Cesium: The Effects of Strain Rate, Localized Stresses and Temperature"
Journal of Nuclear Materials 57: pp. 155-179 (1975)
17. Cubicciotti, D. and Jones, R.L.
"EPRI-NASA Cooperative Project on Stress Corrosion Cracking of Zircalloys"
EPRI NP-717 (1978)
18. Cox, B. and Wood, J.C.
"The Mechanism of SCC of Zirconium Alloys in Halogens"
Proc. Int. Conf. on Mechanisms of Environment Sensitive Cracking of Materials, Guildford, U.K., 1977
Eds. P.R. Swann et al., The Metals Society, London 1977, pp. 520-530.
19. Busby, C.C., Tucker, R.P., and McCauley, J.E.
"Halogen Stress Corrosion Cracking of Zircaloy-4 Tubing,"
Journal of Nuclear Materials, 55: pp. 64-82 (1975)
20. Cubicciotti, D., Jones, R.L., Syrett, B.C.
"Stress Corrosion Cracking of Zircalloys,"
EPRI NP-1329 (1980)

21. Kleinschmidt, P.D., Cubicciotti, D. and Hildenbrand, D.L.
"Thermodynamics of the Gaseous Zirconium Iodides,"
J. Electrochem. Soc., 125: pp. 1543-1548 (1978)
22. Cubicciotti, D. and Scott, A.C.
"Kinetics of Formation of Solid Iodides no Zirconium"
Journal of the Less-Common Metals, 77: 241-250 (1981)
23. Daake, R.L. and Corbett, J.D.
Synthesis and Nonstoichiometry of the Zirconium Trihalides
Inorg. Chem., 17: pp. 1192-1195 (1978)
24. Syrett, B.C.
The Effect of Axial Stress to Hoop Stress Ration on the
Susceptibility of Unirradiated Zircaloy-4 to Iodine Stress
Corrosion Cracking
Journal of Nuclear Materials, 96: 160-168 (1981)
25. Wood, J.C.
"Factors Afecting Stress Corrosion Cracking of Zircaloy in Iodine
Vapour"
Journal of Nuclear Materials, 45: 105-122 (1972/73)
26. Syrett, B.C., Cubicciotti, D., and Jones, R.L.
"Some observations on the Influence of Tube Manufacturing
Technique on Iodine Stress Corrosion Cracking of Unirradiated
Zircaloy"
Proc. of the ANS Topical Meeting on LWR Fuel Performance
Portland (April 1979), pp. 113-
27. Yaggee, F.L., Mattas, R.F., and Neimark, L.A.
"Characterization of Irradiated Zircaloys: Susceptibility to
Stress-Corrosion Cracking"
EPRI Report No. 1155, Sept. 1979
28. Lee, D. and Adamson, R.B.
"Modeling of Localized Deformation in Neutron Irradiated
Zircaloy-2"
Zirconium in the Nuclear Industry, ASTM-STP 633
American Society for Testing and Materials, 1977, pp. 385-401.
29. Tenckhoff, E.
"Operable Deformation Systems and Mechanical Behavior of Textured
Zircaloy Tubing"
Zirconium in Nuclear Applications, ASTM STP 551
American Society for Testing and Materials, 1974, pp. 179-200

30. Peehs, M., Stehle, H., and Steinberg, E.
"Out-of-Pile Testing of Iodine Stress Corrosion Cracking in Zircaloy Tubing in Relation to the Pellet-Cladding Interaction Phenomenon"
Zirconium in Nuclear Industry (Fourth Conf) ASTM STP 681
American Society for Testing and Materials, 1979, pp. 244-260
31. Garlick, A.
"Fracture of Zircaloy Cladding Under Simulated Power Ramp Conditions"
Journal of Nuclear Materials 49: pp. 209-224 (1973/74)
32. Knorr, D.B. and Pelloux, R.M.
"Effects of Texture and Microstructure on the Propagation of Iodine Stress Corrosion Cracks in Zircaloy"
Metallurgical Transactions A, 13: pp. 73-83 (1982)
33. Rice, J.
"A Path Independent Integral and the Approximate Analysis of Strain Concentration by Notches and Cracks"
J. Appl. Mech. 34: pp. 237- (1967)
34. Kanninen, M.F., Popelar, C.H., and Broek, D.
"A Critical Survey on the Application of Plastic Fracture Mechanics to Nuclear Pressure Vessels and Piping"
Nuclear Engineering and Design 67: pp. 27-55 (1981)
35. Videm, K. and Lunde, L.
"Stress Corrosion Crack Initiation and Growth and Formation of Pellet-Clad Interaction Defects"
Zirconium in the Nuclear Industry (Fourth Conf.) ASTM STP 681
American Society for Testing and Materials, 1979, pp. 229-243.
36. Schulz, L.G.
Direct Method of Determining Preferred Orientation of Flat Reflection Sample Using Geiger Counter X-Ray Spectrometer
Journal of Applied Physics, 20: 1030- (1949)
37. Kaufmann, P.D., Danielson, P., and Baroch, E.F.
"Improved Metallography of Zirconium Alloys"
Zirconium in Nuclear Applications ASTM STP 551
American Society for Testing and Materials, 1974, pp. 52-62.
38. Green, J.A.S.
Influence of Texture on the Corrosion and Film Formation of a Titanium Single-Crystal
Corrosion, 30: 175-176(1974)

39. Speidel, M.O. and Hyatt, M.V.
"Stress-Corrosion Cracking of High-Strength Aluminum Alloys"
Advances in Corrosion Science and Technology, vol. 2
Plenum Press (1972) p. 115.
40. Mostovoty, S., Corsley, P.B., and Ripling, E.J.
"Use of Crack Line Loaded Specimens for Measuring Fracture
Toughness"
Journal of Materials, 12: p. 681 (1967)
41. Gillespie, L.J. and Fraser, L.H.D.
"The Normal Vapor Pressure of Crystalline Iodine"
J. Am. Chem. Soc., 58, pp. 2260-2263 (1936)
42. Reid, A.F. and Mill, R.
"Vacuum Drying of Iodine with Molecular Sieves"
J. Inor. Nuc. Chem. 26: pp. 892- (1964)
43. C. Lemaignan. Private communication to R.M. Pelloux
44. Pettersson, K.
"Stress Corrosion Crack Growth in Unirradiated Zircaloy"
Studsvik K4-78/12 (1978)
45. O'Donnell, W.J. and Langer, B.F.
Fatigue Design Basis for Zircaloy Components
Nuclear Science and Engineering: 20, 1-12 (1964)
46. Knorr, D.B.
"Stress Corrosion Cracking of Zircaloy in the Presence of Iodine"
M.I.T. Thesis Mat. Sci. and Eng. 1981 Sc.D.
47. Poole, L. and Borchers, M.
Some Common Basic Programs, 3rd Ed.
Osborne/McGraw-Hill, Berkeley, 1977, p. 151
48. Bevington, P.R.
Data Reduction and Error Analysis for the Physical Sciences
McGraw-Hill, New York, 1969, p. 56
49. Dahiberg, E.P.
Techniques for Cleaning Service Failures in Preparation for
Scanning Electron Microscope and Microprobe Analysis
S.E.M. Handbook (1974), p. 912
50. Wood, J.C.
Factors Affecting Stress Corrosion Cracking of Zircaloy in
Iodine Vapour
Journal of Nuclear Material 45: 105-122 (1972/73)

51. Cox, B.
Environmentally Induced Cracking of Zirconium Alloys
Reviews of Coatings and Corrosion, 1: 367-421 (1975)
52. Krishnan, G.N., Wood, B.J., and Cubicciotti, D.
Auger Electron Spectroscopy Study of the Chemisorption of
Iodine on Zirconium
J. Electrochem. Soc: 127: 2738-2742 (1980)
53. Stull, B.R. and Prophet, H.
JANAF Thermochemical Tables
U.S. National Bureau of Standards, NSRDS-NBS 37, June 1981
54. Cox, B.
Environmentally Induced Cracking of Zirconium Alloys
Corrosion-NACE 28: 207-217 (1972)
55. Smith, E.
The Stress for the Formation of a Cladding Crack During a Power
Ramp
S.M.I.R.T. paper C4/4
56. Smith, E.
The Mechanics of the Fluting Process in Zircaloy
Res Mechanica Letters 1: 21-24 (1981)
57. Kreyns, P.H., Spahr, G.L., and McCauley, J.E.
An Analysis of Iodine Stress Corrosion Cracking of Zircaloy-4
Tubing
Journal of Nuclear Materials 61: 203-212 (1976)
58. Scott, P.M. and Thorpe, T.W.
A Critical Review of Crack Tip Stress Intensity Factors for
Semi-Elliptic Cracks
Fatigue of Engineering Materials and Structures 4: 291-309 (1981)
59. Irwin, G.R.
Crack Extension Force for a Part Through Crack in a Plate
J. Appl. Mech. Trans. ASME 84: 651-654 (1962)
60. Shah, R.C., and Kobayashi, A.S.
Stress Intensity Factors for an Elliptical Crack Approaching
the Surface of a Semi-Infinite Solid
Int. J. Fract. 9: 133-146 (1973)
61. Newman, J.C.
Fracture Analysis of Surface and Trough-Cracked Sheets and Plates
Engng. Fract. Mech. 4: 667-689 (1973)

62. Raju, I.S., and Newman, J.C.
Stress Intensity Factors for a Wide Range of Semi-Elliptical
Surface Cracks in Finite Thickness Plates
Engng. Fract. Mech. 4: 817-829 (1979)
63. Nye, J.F.
Physical Properties of Crystals
Oxford University Press, London (1957)
64. Baratta, F.I., Bluhm, J.I., Driscoll, G.W., and Matthews, W.T.
Int. J. of Fracture Mechanics 7: 203 (1971)
65. Timoshenko, S.
Strength of Materials, Parts I and II
D. Van Nostrand Co., Inc., Princeton, N.J., 1956
66. Knorr, D.B. and Pelloux, R.M.
Research on Mechanisms of Stress Corrosion Cracking in Zircaloy
DOE/ET/34215-24 Uc-78 (1981)

Biographical Note

Arnaldo H Paes de Andrade, the author, was born and raised in Belem, Brasil, where he graduated from Colegio Estadual Paes de Carvalho in 1967. He received a B.S. degree in Physics from the Universidade de Sao Paulo, Brasil in 1971. From 1972 to 1977, the author was employed in Sao Paulo as a member of the research group on solid state physics and materials science of the Instituto de Pesquisas Energeticas e Nucleares (IPEN). In 1977 he received a M.S. degree from the Universidade de Sao Paulo. Also in 1977 he married the former Lane Moreira Brandao. Having made a decision to convert from physics to metallurgy, the author entered the Department of Materials Science and Engineering at MIT where he effectively began his studies in February 1978. While at MIT, he was supported by a Comissao Nacional de Energia Nuclear (RJ-Brasil) fellowship. In 1981, the author and his wife were blessed with a son, Laerte. Upon graduation, the author continues employment at IPEN in his home country.